NAVAL POSTGRADUATE SCHOOL

MONTEREY, CALIFORNIA

THESIS

RESISTANCE OF ULTRA HIGH TEMPERATURE CERAMICS TO CALCIA-MAGNESIA-ALUMINA-SILICATE (CMAS) ATTACK

by

Erick Samayoa

June 2021

Thesis Advisor:	Andy Nieto
Co-Advisor:	Raymond M. Gamache

REPORT DOCUMENTATION PAGE	*Form Approved OMB No. 0704-0188*

1. AGENCY USE ONLY ***(Leave blank)***	**2. REPORT DATE** June 2021	**3. REPORT TYPE AND DATES COVERED** Master's thesis

4. TITLE AND SUBTITLE RESISTANCE OF ULTRA HIGH TEMPERATURE CERAMICS TO CALCIA-MAGNESIA-ALUMINA-SILICATE (CMAS) ATTACK	**5. FUNDING NUMBERS** RMP5J
6. AUTHOR(S) Erick Samayoa	
7. PERFORMING ORGANIZATION NAME(S) AND ADDRESS(ES) Naval Postgraduate School Monterey, CA 93943-5000	**8. PERFORMING ORGANIZATION REPORT NUMBER**
9. SPONSORING / MONITORING AGENCY NAME(S) AND ADDRESS(ES) Strategic Environmental Research & Development Program (SERDP)	**10. SPONSORING / MONITORING AGENCY REPORT NUMBER**

11. SUPPLEMENTARY NOTES The views expressed in this thesis are those of the author and do not reflect the official policy or position of the Department of Defense or the U.S. Government.

12a. DISTRIBUTION / AVAILABILITY STATEMENT Approved for public release. Distribution is unlimited.	**12b. DISTRIBUTION CODE** A

13. ABSTRACT (maximum 200 words)

New hypersonic vehicles will operate inside the atmosphere through flight and are now subjected to increase atmospheric particulates exposure primarily composed of Calcia-Magnesia-Alumina-Silicate (CMAS) and is known as CMAS attack. CMAS attack affects thermal and environmental barrier coatings and is an ongoing problem for gas turbine engines (GTE). New materials are needed to withstand high temperatures while resisting CMAS attack. This thesis aims to characterize CMAS interaction with the two candidates for hypersonic applications: hafnium and zirconium diboride.

Both ceramics were mixed with CMAS and then placed in isothermal holds at 1000–1600°C between 1–100 hours of exposure. The samples were then analyzed via transmission/scanning electron microscope (T/SEM), energy dispersive spectroscopy (EDS), and x-ray diffraction (XRD) to identify new phases.

At all temperatures and durations, both diborides oxidized and produced MO2(M=Hf/Zr). For durations less than an hour regardless of temperature, both diborides reacted weakly or did not react with the CMAS. For all other durations and temperatures, the silicate in the CMAS reacted with MO2 and produced MSiO4 but then revert back into their oxide and SiO2 at 1600°C. Further studies will look at bulk pucks of MB2 for better characterization of CMAS infiltration on both diborides under hypersonic conditions using a rig burner.

14. SUBJECT TERMS UHTC, hypersonic, CMAS, ceramics, HfB2, ZrB2, T/SEM, EDS, XRD	**15. NUMBER OF PAGES** 137
	16. PRICE CODE

17. SECURITY CLASSIFICATION OF REPORT Unclassified	**18. SECURITY CLASSIFICATION OF THIS PAGE** Unclassified	**19. SECURITY CLASSIFICATION OF ABSTRACT** Unclassified	**20. LIMITATION OF ABSTRACT** UU

NSN 7540-01-280-5500

Standard Form 298 (Rev. 2-89)
Prescribed by ANSI Std. 239-18

THIS PAGE INTENTIONALLY LEFT BLANK

RESISTANCE OF ULTRA HIGH TEMPERATURE CERAMICS TO CALCIA-MAGNESIA-ALUMINA-SILICATE (CMAS) ATTACK

Erick Samayoa
Lieutenant, United States Navy
BS, The Citadel, 2014

Submitted in partial fulfillment of the
requirements for the degree of

MASTER OF SCIENCE IN APPLIED PHYSICS

from the

NAVAL POSTGRADUATE SCHOOL
June 2021

Approved by: Andy Nieto
Advisor

Raymond M. Gamache
Co-Advisor

Kevin B. Smith
Chair, Department of Physics

THIS PAGE INTENTIONALLY LEFT BLANK

ABSTRACT

New hypersonic vehicles will operate inside the atmosphere through flight and are now subjected to increase atmospheric particulates exposure primarily composed of Calcia-Magnesia-Alumina-Silicate (CMAS) and is known as CMAS attack. CMAS attack affects thermal and environmental barrier coatings and is an ongoing problem for gas turbine engines (GTE). New materials are needed to withstand high temperatures while resisting CMAS attack. This thesis aims to characterize CMAS interaction with the two candidates for hypersonic applications: hafnium and zirconium diboride.

Both ceramics were mixed with CMAS and then placed in isothermal holds at 1000–1600°C between 1–100 hours of exposure. The samples were then analyzed via transmission/scanning electron microscope (T/SEM), energy dispersive spectroscopy (EDS), and x-ray diffraction (XRD) to identify new phases.

At all temperatures and durations, both diborides oxidized and produced MO2(M=Hf/Zr). For durations less than an hour regardless of temperature, both diborides reacted weakly or did not react with the CMAS. For all other durations and temperatures, the silicate in the CMAS reacted with MO2 and produced MSiO4 but then revert back into their oxide and SiO2 at 1600°C. Further studies will look at bulk pucks of MB2 for better characterization of CMAS infiltration on both diborides under hypersonic conditions using a rig burner.

THIS PAGE INTENTIONALLY LEFT BLANK

TABLE OF CONTENTS

LIST OF FIGURES

LIST OF TABLES

THIS PAGE INTENTIONALLY LEFT BLANK

LIST OF ACRONYMS AND ABBREVIATIONS

AFRL	Air Force Research Lab
CMAS	calcia-magnesia-alumina-silicate
DOD	Department of Defense
EBC	environmental barrier coating
EDS/X	energy-dispersive X-ray spectroscopy
E/TBC	environmental/thermal barrier coating
SEM	scanning electron microscopy
SPM	suspended particulate matter
TBC	thermal barrier coating
TEM	transmission electron microscopy
TSP	total suspended particle matter
UHTC	ultra-high temperature ceramics
YSZ	yttria-stabilized zirconia

THIS PAGE INTENTIONALLY LEFT BLANK

ACKNOWLEDGMENTS

Special thanks to the physics faculty for allowing me to venture off into other departments in search of a topic that interested me. I would like to thank Professor Andy Nieto for his guidance and willingness to advise a physics graduate student taking on a material science topic. I would also like to thank Professor Troy Ansell for spending countless hours teaching me how to use all the instruments needed for my thesis.

Another special thanks to all my family, cohort, and friends who supported me throughout my course of study at the Naval Postgraduate School. Without them, I would not be where I am today.

THIS PAGE INTENTIONALLY LEFT BLANK

I. INTRODUCTION

A. BACKGROUND AND MOTIVATION

Hypersonic speed for military applications has been a great interest for the Department of Defense since the 1960s but a renewed interest prompted greater research into developing hypersonic weapons to compete against hypersonic weapons developed by Russia and China. Material exposure to hypersonic speeds is not new to some military weapon systems, as most intercontinental ballistic missiles encounter comparable temperatures in their trajectories. A key difference with new hypersonic vehicles is the requirement to operate inside the atmosphere throughout their entire flight and subjected to increase temperatures as a result. Surfaces of these bodies reach temperatures in excess of 1200˚C causing degradation of the aeroshell enabling catastrophic failure during flight. As a result, new composites are needed that can withstand harsher and faster hypersonic speed for sustain periods of time.

Several candidate materials have been identified to operate in these extreme regions such as ceramic borides, carbides, and nitrates which demonstrate high melting points [1].

Carbides, classified into three composition groups (ionic, covalent, and interstitial), are known to have extremely strong bonds. Theses strong bonds give them favorable properties. Ionic carbides have little use for applications because of their extreme brittleness. Interstitial (defect atom located within an atomic structure) carbides located within Hf and Zr have the highest melting point temperature of known materials [1]. The covalent carbides (such as SiC and B_4C) are have extreme hardness, and excellent thermal and chemical stability [1]. Due to their refractoriness and brittleness, fabrication of these carbides ceramics have been limited to lab scale [1]. Nitrides also share many of the properties of carbides and are difficult to fabricate as well [1].

Although bond strength of borides is not as strong and have lower melting points compared to carbides, borides have excellent thermal and electrical conductivities (higher than carbides and nitrates), and low coefficients of thermal expansion as discussed by Gasch et al. [1]. in his review of UHTCs. The combined properties enable good thermal shock resistance as well as good oxidation resistance[1]. Most comprehensive research on ultra-high temperature ceramic (UHTC) oxidation resistance and mechanical behavior has focused on compositions containing HfB_2 or ZrB_2 because of their better oxidation resistance over other ceramics [1–5].

The materials investigated in this thesis were selected due to their favorable properties such as their oxidation resistance over nitrates and carbides[1]. As these missiles continue to operate in lower altitudes, not only will they encounter higher temperatures but more environmental particulates such as volcanic ash, salts, runway debris, dust, and sand affecting these ceramics in ways not yet fully understood in this emerging field.

Environmental particulate attack is a field of great interest for thermal and environmental barrier coating (T/EBC) technology including engine applications for military aircrafts. Several decades of forensic analysis on field returned components enable a greater understanding of material degradation/changes due to environmental conditions [6]. Extensive research has been conducted to the how these particulates degrade aerodynamic performance, structural and chemical integrity of T/EBC [6]. The environmental particulates often enter aircraft engines and melt, due to high temperature, into glassy and crystalline phases causing degradations or engine failures over time. The primary constituents of this environmental particulates are calcia-magnesia-alumina-silicate- (CMAS) based compounds and when high temperatures enable chemical interaction, this is known as a CMAS attack.

As a result, extensive studies have been conducted on CMAS adhesion, infiltration, spallation mechanics, and thermochemical attack mechanisms in an effort to mitigate CMAS attacks on T/EBC. Synthetic CMAS formers were created to mimic the compositions found in areas of interest for the DOD such as AFRL-02. AFRL-02 is a synthetic sand which will be used in this paper to study CMAS attacks, due to its ability to form both glassy and crystalline phases seen in the field [6]. The standardized method of evaluating CMAS attacks in GTEs is to use AFRL-02 as it closely resembles sand found in the Middle East, an area of interest for DOD and generic enough to simulate sand found globally [7].

The following chapter provides a summary of the current understanding of CMAS attack on T/EBCs and the properties of HfB_2 and ZrB_2, two promising candidates for hypersonic applications to understand what reactions the UHTCs will have when expose to CMAS attack in a hypersonic temperature environment with applications in other high temperature environments such as gas turbine engines where particulate attack is likely.

B. THESIS OBJECTIVES

This thesis will provide insight to the following questions:

- What effects does CMAS have on the properties of HfB_2 and ZrB_2?
- Between HfB_2 and ZrB_2, which boride is affected the most by CMAS attack?
- What chemical or physical effects does CMAS attack cause at different temperature ranges on the UHTCs?

THIS PAGE INTENTIONALLY LEFT BLANK

II. LITERATURE REVIEW

A. CMAS LITERATURE REVIEW

1. Sand Composition

Military operations are performed in a wide spectrum of environments where many contaminants adversely affect military equipment. Such examples include atmospheric turbulence which alters beam sizes on laser systems, ambient noises within the ocean causing degradation of sonar signals, and sandstorms degrading radar performance. Sand, in particular, affects many military systems, specifically gas turbine engines. Current military activities include operations in the Middle East where the environmental conditions include lack of moisture, and high temperatures. These factors produce extremely dry ground surfaces and dry wind currents that enables the transport of sand from different regions that carry a variety of different minerals content, particle size and trace elements that can be exposed to military equipment. Knowing sand compositions will help in characterization of CMAS behaviors at elevated temperatures.

Kelly et al. [8] characterized 12 soil samples from Iraq and Afghanistan and found that calcium carbonate was the most dominant mineral in the samples and in both regions, silt and clay sized particles were more abundant than sand-sized particles. Table 1 shows particles sizes between sand, clay, and silt.

Table 1. Soil size comparison provided by USDA. Source: [9]

Particle	Size Range [mm]
Very coarse sand	<2.0 to >1.0
Coarse sand	1.0 to > 0.5
Medium sand	0.5 to > 0.25
Fine sand	0.25 to > 0.10
Very fine sand	0.10 to > 0.05
Coarse silt	0.05 to > 0.02
Fine silt	0.02 to >0.002
Coarse clay	0.002 to > 0.0002
Fine clay	≤0.0002

In another particulate characterization, Englebrecht et al. [10] analyzed air-suspended particulate matter (SPM) in 15 locations throughout the Middle East. Using various filters to capture particles of different sizes, the results from the study showed the particles comprise of the majority of material ingested into military aircraft engines.

The results of the collected particles found, and their composition are shown in Figure 1. The locations of collected samples are compared to sands found throughout the world in Figure 2. Englebrecht pointed out that Middle East sand is more abundant in CaO and lower in SiO_2 than the sand from the other 21 deserts around the world.

An analysis, conducted by Smialek, of selected sand samples provided by the U.S. military shows typical sand compositions found in Saudi Arabia shown in Table 1 [11] . Chemical analysis was performed by the emission spectroscopy of sand dissolved in HF-$HN0_3$ or a sodium-salt fusion technique. Carbon and sulfur were analyzed by combustion gas analysis A map of the regions of operations can be seen in Figure 3. Table 2 shows the two most abundant minerals in dune sands are quartz (SiO_2) and carbonate (CO_2) and for riverbed sand, the two most abundant minerals are calcite ($CaCO_3$) and dolomite ($CaMg(CO_3)_2$) [11].

Table 2. Composition of selected Saudi Arabia Sand. Source: [11].

	Dune Sand	**20 µm Fines**	**10 µm Saudi No. 1**†	**River Bed Sand**
SiO_2	90.8	52.4	55.0	12.3
CaO	1.5	17.4	20.9	25.9
Al_2O_3	2.5	14.3	13.6	5.2
Fe_2O_3	0.8	8.8	8.2	0.9
MgO	0.5	4.4	‡	15.6
NiO	1.0	0.5	NA	0.2
TiO_2	0.2	0.9	2.2	0.2
Na_2O	0.2	‡	NA	0.2
K_2O	0.5	‡	trace	0.1
CO_2	5.6	NA	NA	39.4
SO_2	1.3	NA	NA	8.5

NA—not analyzed

* Emission spectroscopy, normalized to 100% oxide.

† From BFLRF No. 294.[4]

‡ Not found.

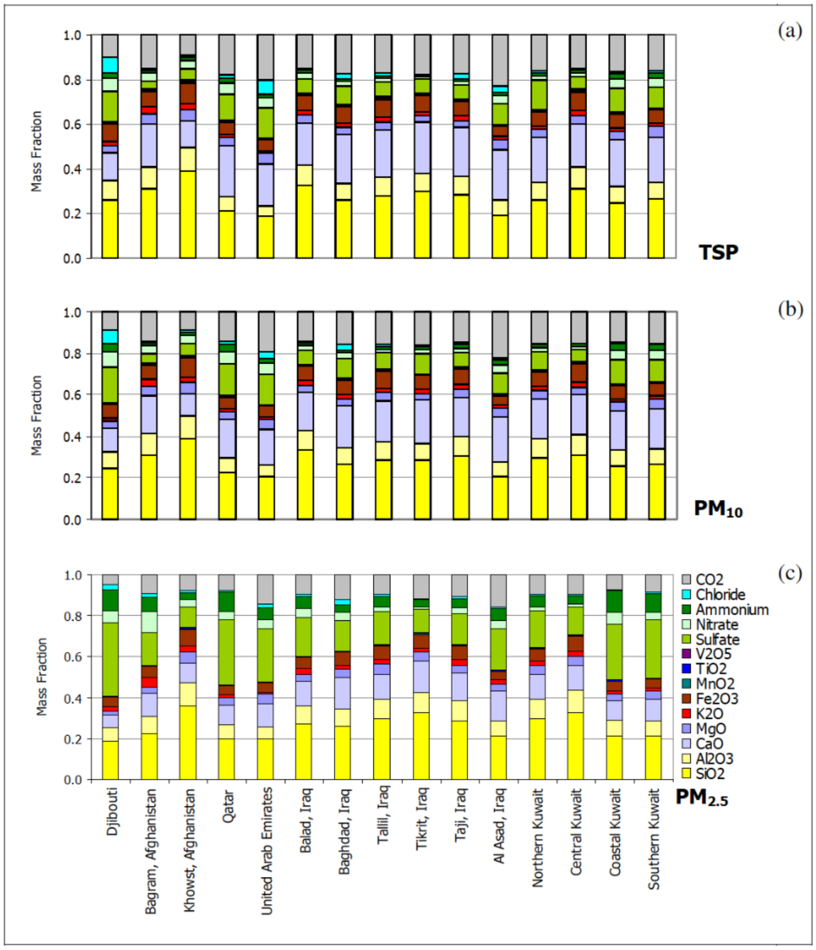

Figure 1. Composition of particulates for (a) TSP, (b) PM10, (c) PM2.5 as mass fractions. Source: [10].

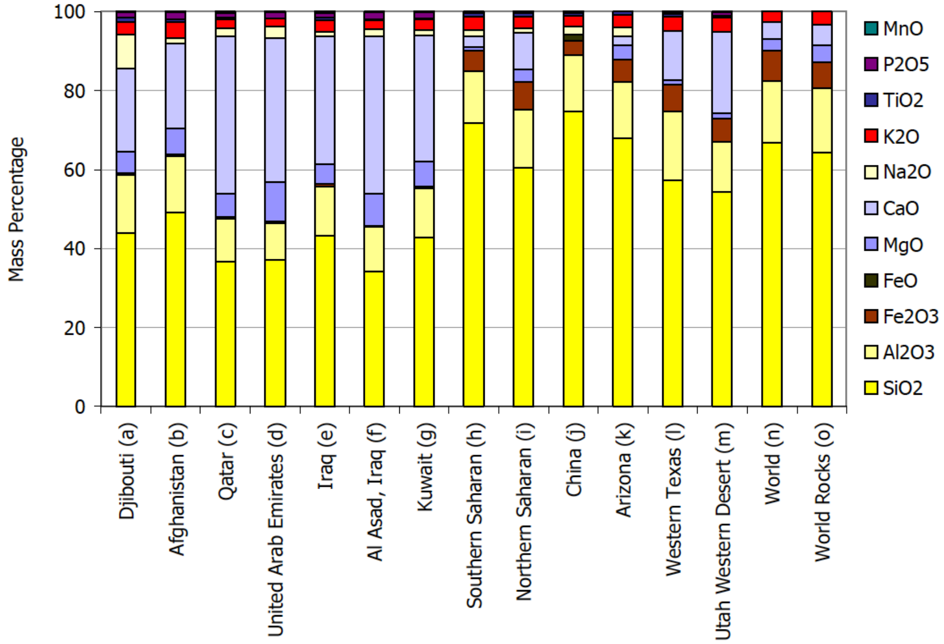

Figure 2. Comparison of dust samples from the Middle East, Sahara, China, U.S., world average dust, and world rocks. Source: [10]

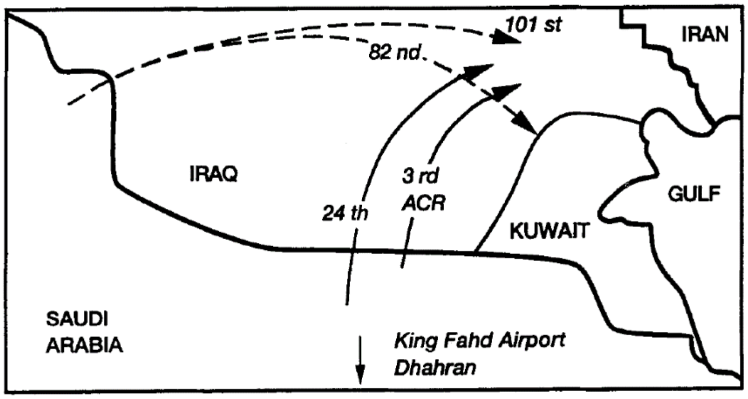

Figure 3. The source history of the sand sample. Source: [11].

Another study conducted by de Wet et al. [12] sampled five different sites throughout the Middle East and their results are shown in Table 3. The analysis shows the most abundant mineral is quartz. The following minerals were also observed: quartz, calcite, and dolomite as well as the feldspar silicates including albite, microcline, and gypsum.

Table 3. XRD analysis of sand samples from Middle East. Amount indicted by vs=very strong, s=strong, m=medium, w=weak, and vw=very weak. Source: [12]

Mineral	Sinaiyah	Bahrain	Dubai	Abu Dhabi	Doha
Quartz α-SiO_2	vs	vs	s	vs	w
Calcite $CaCO_3$	w	w/m	vs	s	w
Aragonite $CaCO_3$	-	m	-	-	-
Dolomite $CaMg(CO_3)_2$	w	w/m	w	w	m
Gypsum $CaSO_4.2H_2O$	-	-	-	-	vs
Albite $NaAlSi_3O_8$	m	w	w	m/s	-
Microcline $KAlSi_3O_8$	m	w	w	w	-
Diopside $CaMg(SiO_3)_2$	-	w/m	-	-	-

These studies show that the composition of sand can differ in composition makeup and as a result several synthetic CMAS were created to best stimulate natural CMAS attacks on gas turbine engines. A study conducted by Opie [7] sought to compare a variety of synthetic CMAS powders against naturally occurring sands found in Arizona and Afghanistan. This analysis revealed that AFRL-02 was able to closely mimic real world sand ingestion from the Middle East. This data supports the use ARFL-02 within the development of the next generation of CMAS-resistant TBC.

2. Gas Turbine Coatings

Before reviewing the effects of CMAS attacks, this section will briefly discuss coating composition of a gas turbine engine. Engines need a ceramic coating that can withstand extreme temperature environments. Table 4 shows the ideal characteristics of a ceramic coating applied to a GTE. Zirconia (ZrO_2) possesses a majority of ideal properties suitable for TBC but is subjected to polymorphic phase transformations and varying volumes changes (from 3–5%) while heating and cooling [13]. To solve this issue, zirconia is doped with yttria, stabilizing it from these phase changes. It was found that YSZ is stabilized with seven weight percent (wt.%) yttria (Y) in order to retain the desired coefficient of thermal expansion over a wide range of temperatures [14] and is commonly referred to as 7YSZ. If yttria concentration is increased, at higher temperatures YSZ will be dominated by the cubic phase which does not possess the same strength and durability than the tetragonal phase[13]. At lower yttria concentration, monoclinic structure prevails over YSZ structure which possess poor strain tolerance of the TBC[13]. The tetragonal phase is the preferred phase because it is more durable with greater strength while still maintaining an acceptable strain tolerance for TBC applications[15].

Table 4. Favorable properties for TBC. Source: [13].

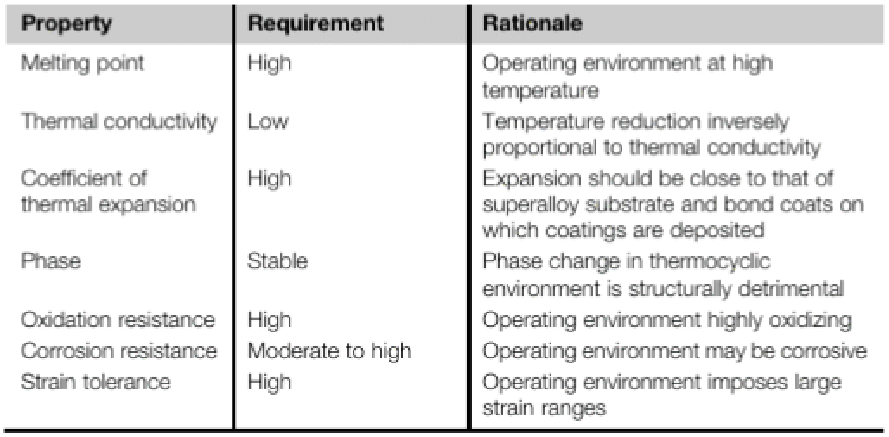

Property	Requirement	Rationale
Melting point	High	Operating environment at high temperature
Thermal conductivity	Low	Temperature reduction inversely proportional to thermal conductivity
Coefficient of thermal expansion	High	Expansion should be close to that of superalloy substrate and bond coats on which coatings are deposited
Phase	Stable	Phase change in thermocyclic environment is structurally detrimental
Oxidation resistance	High	Operating environment highly oxidizing
Corrosion resistance	Moderate to high	Operating environment may be corrosive
Strain tolerance	High	Operating environment imposes large strain ranges

3. CMAS Attack

Once sand, primarily composed of calcia-magnesia-alumina-silicate constituents, enters a gas turbine engine, the temperature melts the sand into a glassy-crystalline mixture where then it infiltrates and attacks TBC systems by degrading thermal protective properties reducing engine life. Figure 4 shows a damaged turbine blade and vane caused by CMAS attack.

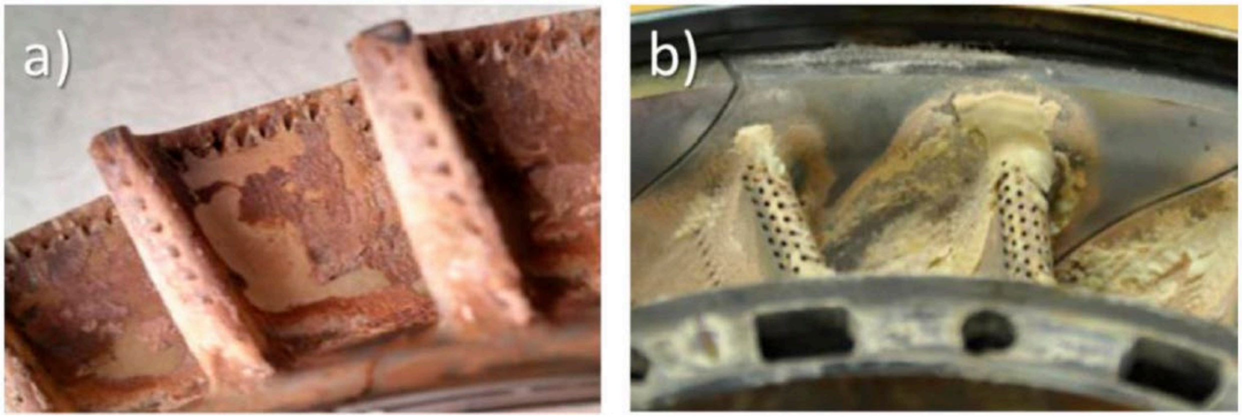

Figure 4. CMAS-induced damage on (a) blade and (b) vane. Source: [16]

4. Infiltration and Failure

Chemical attack of CMAS adversely affects TBC coating by removing Y from YSZ. As discussed before, lower the yttria concentration will affect the phase-stabilization of Zr, resulting in a monoclinic structure which is deleterious to the integrity of the TBC [13,17–19].

In a review conducted by Shifler [20], infiltration of CMAS is dependent on the temperature of the blade, the hotter the blade, the greater the infiltration and quickly decrease as temperature decreases. At lower temperatures, CMAS will start to solidify as well. Once the environment cools off, delamination developed in the TBC just underneath the CMAS deposit as the affected area experiences a thermal expansion mismatch.

5. CMAS Properties

Both Wiesner et al. and Opie[7] determined the composition of synthetic sand CMAS/AFRL-02 and are shown in Table 5. The main constituents for synthetic CMAS are quartz, gypsum, aplite, dolomite, and salt. Opie [7] further found the particle distribution size to be: 90% 40.5 μm, 50% 8.5 μm, and 10% 2.5 μm. Figure 5 shows the X-ray diffraction (XRD) spectra of the synthetic CMAS and Figure 6 shows the XRD spectra of the CMAS glass after heated.

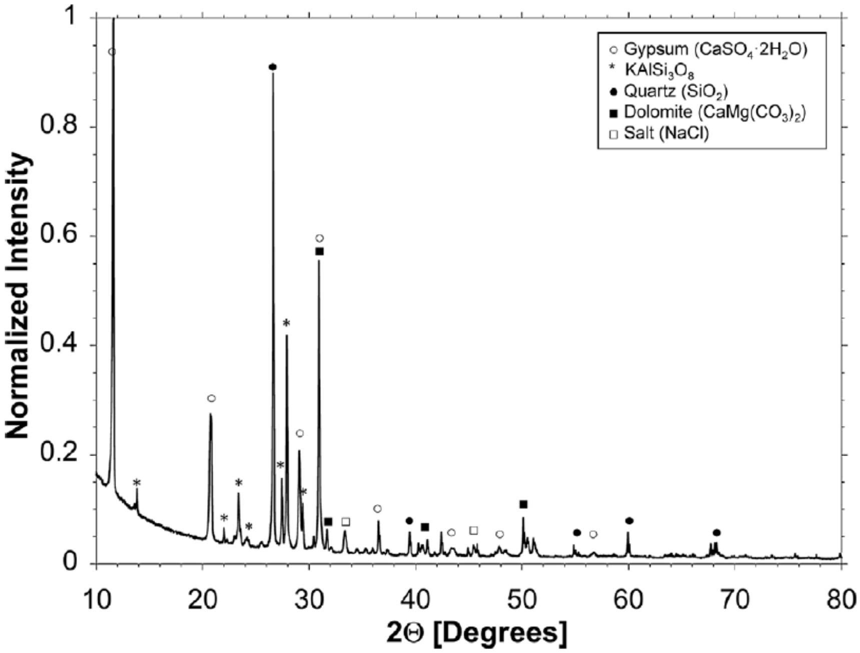

Figure 5. XRD of the CMAS powder. Source: [21]

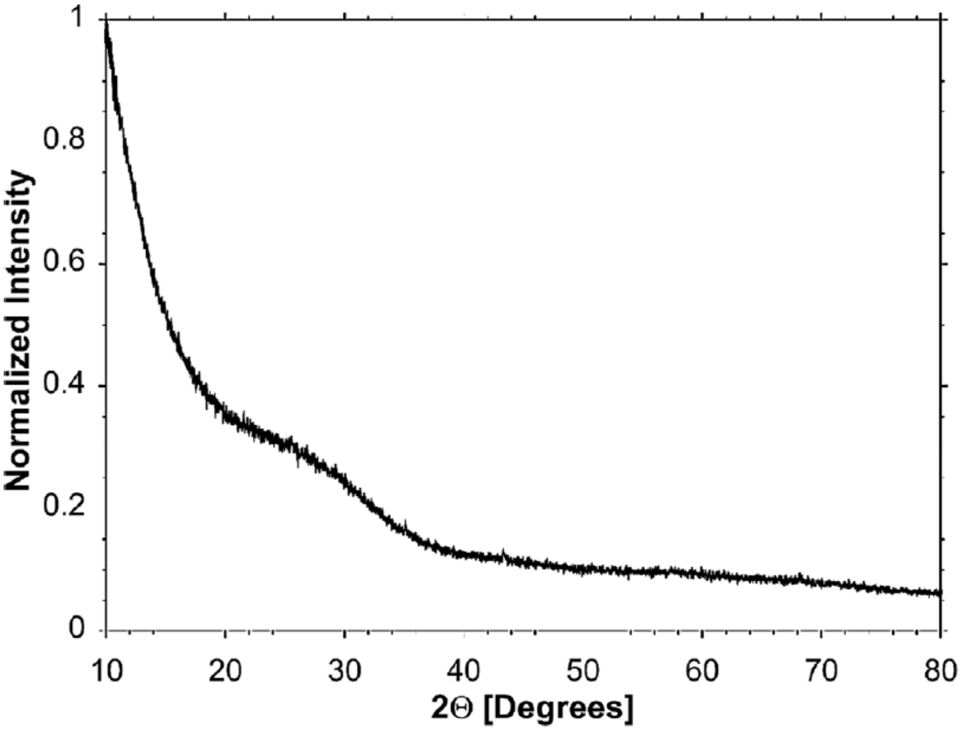

Figure 6. XRD spectra of CMAS glass. Source: [21]

Table 5. Composition of synthetic CMAS sand.

CMAS/AFRL-02	% by Wt., Wiesner [21]	% by Wt., Opie [7]	% by Wt., Powder Tech. Inc. [22]
Quartz	34	36.56	34
Gypsum	30	28.75	30
Aplite	17	16.36	17
Dolomite	14	13.33	14
Salt	5	5	5

Wiesner et al. [21]. then heated the CMAS former until it melted into glass. The glassy CMAS had a bulk density of 2.63 g, Young's modulus of 84.3 GPa, shear modulus of 33.6 GPa and Poisson's ratio 0.26[21]. The CMAS glass exhibited a melting temperature of 1176°C, which is below the operating temperature of engine components. Wiesner et al. also pointed out the low melting point shows at higher temperatures, CMAS glass can easily flow throughout the engine allowing infiltration and damage TBCs[21].

B. HAFNIUM DIBORIDE AND ZIRCONIUM DIBORIDE LITERATURE REVIEW

1. UHTCs

Gasch et al. conducted a review of UHTCs and concluded HfB_2 and ZrB_2 are ideal candidates for TBC hypersonic environments because of their favorable properties over other ceramics such a high melting point and oxidation resistance.[1].

ZrB_2 and HfB_2 has a melting temperature of 3245°C and 3380°C respectively with a hexagonal crystal structure[1,23]. Their B-B rings and M-B bonds give them very high hardness and temperature stability as well [1,23]. Gasch [1] also pointed out that both have low coefficients of thermal expansion and high thermal conductivities which in turn give both borides good thermal shock resistance. Table 6 shows these properties for selected

UHTCs. Compared with other ceramics, both borides have greater oxidation resistance which makes them ideal candidates for hypersonic applications.

Table 6. Thermal expansion and conductivity of UHTCs. Source: [1].

	Thermal Expansion	Temp. Range	Thermal Conductivity	Temp.	
Material	10^{-6}/K	°C	W/m*K	°C	Ref.
HfB_2	6.3	20–1027	105	20	5, 30
	6.8	1027–2027	75	400	5, 30
	7.6	20–2205	70	800	5, 30
HfB_2-20v% SiC	–	–	79	100	31
	–	–	74	500	31
	–	–	62	1000	31
HfC	6.6	20–1500	20	20	5
	–	–	23	400	5
	–	–	30	800	5
HfN	∼6.5	20–1000	18	20	5
	–	–	20	400	5
	–	–	22	800	5
ZrB_2	5.9	20–1027	–	–	30
	6.5	1027–2027	–	–	30
	8.3	20–2205	–	–	30
ZrB_2-20v% SiC	5–7.8	400–1600	98.7	100	31
	–	–	84.5	500	31
	–	–	78	1000	31
ZrC	6.7	20–1500	–	–	25
TiB_2	4.6	20–1027	–	–	30
	5.2	1027–2027	–	–	30
	8.6	20–2205	–	–	30
TiC	7.7	20–1500	–	–	25
TaB_2	8.2	20–1027	16.0	20	30
	8.4	1027–2027	16.1	1027	30
	8.4	20–1650	36.2	2027	30
TaC	6.3	20–1500	–	–	25
SiC	1.1	20	114	20	32
	5.0	1000	35.7	1000	32
	5.5	1500	26.3	1500	32

2. Oxidation

Oxidation is a chemical process in which oxygen reacts with any composition forming an oxide. In oxygen rich environment, reaction rates increase with temperature. Oxides have different thermal expansion coefficients, making them prone to mismatch with the borides. With these mismatches, the coatings are subjected to thermal shock and failure in an operational environment.

HfO_2 and ZrO_2 are the oxidation products of both HfB_2 and ZrB_2 respectively and both also produce B_2O_3. Upadhya et al. [24] discussed the advantages of HfO_2 and ZrO_2 over other UHTCs. As mention before with zirconia(3-5% change in volume)[13], Upadhya et al. also stated the solid-phase transformations of HfO_2 and ZrO_2 experience volume change under different high temperatures , shown in Table 7, that could result in failure of TBC on the system[24]. As a result, both HfB_2 and ZrB_2 must be doped with additives (such as SiC)[1,2,23,25–27] to stabilize phase transformations without affecting their desirable melting and softening temperatures. The following sections will go more into detail for both HfB_2 and ZrB_2.

Table 7. Phase changes due to temperature for ZrO_2 and HfO_2. Adapted from [24].

	Monoclinic to tetragonal	Tetragonal to cubic
HfO2	1650°C	2700°C
ZrO2	1150°C	2370°C

As mentioned, the products of oxidation are hafnium dioxide (HfO_2) and boric oxide (B_2O_3) and is given by Equation 1. Tandon et al. [28] also found oxidation resistance of HfB_2 increased when the temperature is below the boiling point of B_2O_3 (1500°C at 1 atm pressure) and is attributed to liquid B_2O_3 sealing voids in the sample preventing oxygen to enter.

$$HfB_2(cr)+\frac{5}{2}O(g)\rightarrow HfO_2(cr)+B_2O_3(l) \qquad (1)$$

Bargeron [29] found reaction creates a layered composition, one of the HfB_2 and the other of the oxide. In Figure 7, the oxide is distinguishable from the HfB_2 by its columnar structure. This pattern remained consistent up until the boiling point of B_2O_3, shown Figure 8, where large bubbles and noticeable separation formed between the oxide and parent boride [29].

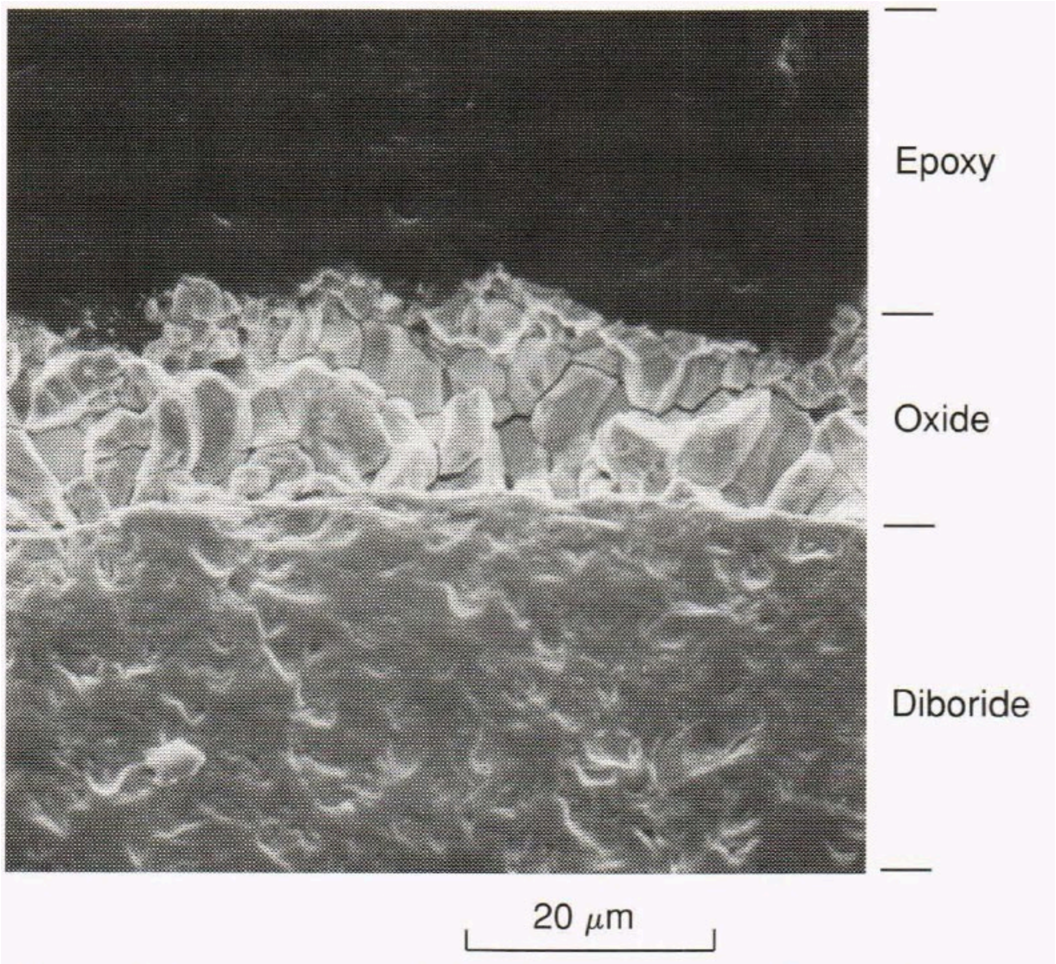

Figure 7. Cross section of the HfB_2 and oxide after heated for 1800 seconds at 1520°C. Source: [29].

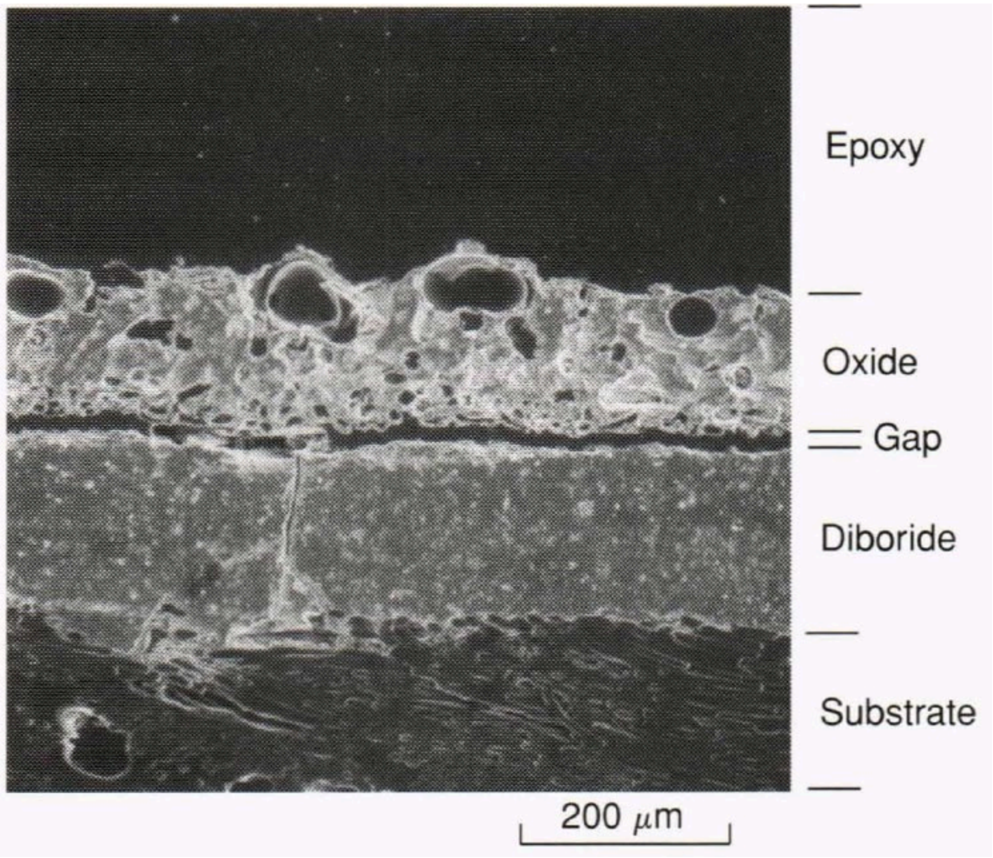

Figure 8. Bargeron et al. conducted a study to analyze the oxidation mechanisms of hafnium carbide and hafnium diboride. Cross section of the HfB_2 and oxide after heated for 300 seconds at 1900°C. Source: [29].

ZrB_2 has similar reactions for oxidation like HfB_2, Parthasarathy[3] discussed the two main phases for ZrB_2 are ZrO_2 and B_2O_3 with distribution of these scales varying with temperature and shown in Figure 9. At temperatures under 1000°C, glassy B_2O_3 is observed on top of the (ZrO_2 + B_2O_3) scale, but is absent at higher temperatures as it evaporates[28]. At all temperatures, a porous zirconia is observed. Parthasarathy also noted at low and intermediate temperatures, the pores in the zirconia are filled with B_2O_3 [3]. The reaction that describes the oxidation is given in Equation 2. Table 8 provides a summary of the oxidation products of HfB_2 and ZrB_2.

$$ZrB_2(cr) + \frac{5}{2}O_2(g) \rightarrow ZrO_2(cr) + B_2O_3(g) \tag{2}$$

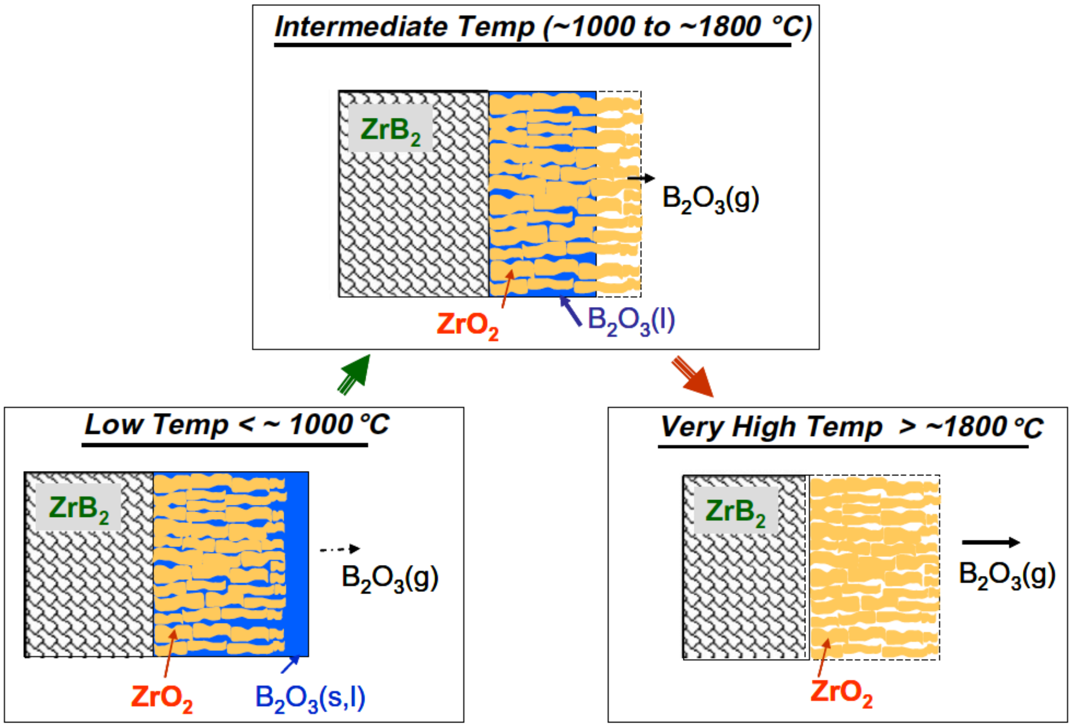

Figure 9. Oxidation products formed during oxidation of ZrB_2 in three temperature regimes. Source: [3].

Table 8. Summary of Oxidation Products of HfB_2 and ZrB_2. Source: [28].

Compound	Temperature	Products
HfB_2	above 1488K	HfO_2 (c); B_2O_3 (g)
ZrB_2	below 1329K Above 1439K	ZrO_2 (c); B_2O_3 (c) ZrO_2 (c); B_2O_3 (g)

III. MATERIALS AND METHOD

A. MELTING OF CMAS

AFRL-02 synthetic sand created by Powder Technology Inc. [22] with a composition listed in Table 5 was melted to prepare CMAS glass. The sand was selected to replicate sand glass that closely resemble sand found in the Middle East, an area of interest for DOD [7]. The procedure involved heating the synthetic sand to 1500°C at a rate of 2°C/min until 800°C and then at a rate of 1°C/min until reaching 1500°C with a one-hour isothermal hold at 1500°C in a platinum crucible in an open tube furnace. 1500°C was picked into to produce both crystalline and glassy CMAS to better simulate environmental conditions.

B. SAMPLE PREPARATION AND PROCESSING

To accurately characterize the high-temperature interactions between HfB_2, ZrB_2 , and the CMAS glass, we used a mixture of 23 mol% CMAS glass powder and 77 mol% of UHTC previously as conducted by Wiesner et al. [30].

For our experiment, 1.5 grams of the UHTCs was used for the experiment. Using the information in Table 9 and 10, the moles in the UHTCs and CMAS were calculated to determine the correct amount of mol% of CMAS needed for the experiment.

Table 9. Molecular weight and mass for HfB_2 and ZrB_2.

UHTC	Molecular Weight	Mass [g]
HfB_2	200.11	1.5
ZrB_2	112.85	1.5

Table 10. Composition and molecular weight of the constituents of AFRL-02 (CMAS).

Mineral	% by WT	Molecular Weight
Dolomite	13.33	184.40
Gypsum	28.75	172.17
Aplite	16.36	262.22
Silica	36.56	60.08
Salt	5	58.44

$$mol = M / MW \tag{3}$$

Where, mol is moles, M is mass, and MW is molecular weight.

$$(HfB_2)_{mol} = 0.0075 \tag{4}$$

$$(ZrB_2)_{mol} = 0.0133 \tag{5}$$

Molecular weight of CMAS will be:

$$CMAS_{MW} = 13.33*(CaMg(CO_3)_2) + 28.75*(CaSO_4 * H_2O) + 16.36*(NaAlSi_2O_8) + 36.56*(SiO_2) + 5*(NaCl) \tag{6}$$

$$CMAS_{MW} = 141.86 \tag{7}$$

where $CMAS_{MW}$ is a function of the molecular weight of the constituents multiplied by the percentage by weight.

To yield the 23% mol of CMAS glass powder and 77% UHTC mixture needed for the experiment, we use:

$$(CMAS)_{23\%} = \frac{(CMAS)_{mol}}{((HfB_2)_{mol} + (CMAS)_{mol})} * 100 \tag{8}$$

$$(CMAS)_{23\%} = 0.318 \text{ grams for 1.5 grams of } HfB_2 \tag{9}$$

$$(CMAS)_{23\%} = \frac{(CMAS)_{mol}}{((ZrB_2)_{mol} + (CMAS)_{mol})} * 100 \tag{10}$$

$$(CMAS)_{23\%} = 0.563 \text{ grams for 1.5 grams of } ZrB_2 \tag{11}$$

The CMAS glass and crystalline was then ball milled using SPEX Sample Prep 8000D Mixer/Mill inside a ceramic jar with 2:1 mixture of 3 mm zirconia balls for 90 minutes to obtain a very fine grit . Once enough CMAS glass was produced, 18 different samples were created; 9 samples each containing 1.5 grams of HfB_2 and 0.318 grams of glass and another 9 samples containing 1.5 grams of ZrB_2 and 0.563 grams of glass which were all placed inside a ceramic jar with no ball mills for 40 minutes to produce analogous and homogenous samples.

C. ISOTHERMAL FURNACE TESTING

The procedure consisted of nine runs with different parameters to accurately characterize the interactions. The first set was held at a fixed temperature of 1000°C with three separate runs that utilized time intervals of either one hour, ten hours, and 100 hours. The second set increased the temperature to 1300°C with the same time intervals for three separate runs, and the third set increased the temperature to 1600°C with the same time intervals for each run.

The first trial used a Lindberg box furnace with a ramp up rate of 16.67° per minute and held at 1000°C for one hour and then allowed to naturally cool down to room temperature.

The second trial used a Lindberg STF 5444C tube furnace with an initial ramp up rate of 20° per minute until reaching 800°C and then 10° per minute until reaching 1300°C for a one-, ten-, and one-hundred-hour isothermal hold. The sample was then allowed to naturally cool down to room temperature in all three runs.

For the third trial, the sample was heated up to 1600°C using CM Furnace 1804 FL with a ramp up rate of 6° per minute and held for an hour, ten hours, and 100 hours and followed the same cool down procedures with previous runs.

D. CHARACTERIZATION

Zeiss FIB and Inspect F50 Scanning electron microscopy (SEM) was used to obtain images and EDS mapping of CMAS, CMAS glass, HfB_2, ZrB_2 powders, and reaction products to characterize parameters using 5–20 keV at working distance of 4–7mm and various magnification levels. Additional SEM images of the powder's cross section were taken. FEI Tecnai Osiris (Scanning) Transmission Electron Microscope was also used to image samples.

X-ray diffraction (XRD) spectra of CMAS, CMAS glass powder, HfB_2 and ZrB_2 were obtained using a Rigaku MiniFlex 6000 XRD with Cu Ka radiation. A step scan procedure with 0.01° per step with 5° per min speed using 40 kV and 15 milliamps was employed to obtain XRD patterns to characterize the powders.

IV. RESULTS

A. CMAS AND UHTC PARTICULATE CHARACTERIZATION

AFRL-02(referred as CMAS former in this thesis), produced by Powder Technology Inc., was analyzed using SEM and XRD. The particle sizes varied size, shape, distribution, and uniformity. The chemical composition of each constituent is shown in Table 11. Using Microtrac S3500 analyzer, PTI determined the percentage of the particle sizes, shown in Table 12. SEM revealed that the majority of the particles are rectangular and roughly under 10 µm in size. A small percentage of the particles were found to be smaller than 1 µm in size and were observed on the surface of the larger particles as shown in Figure 10, Figure 11, and Figure 12.

Table 11. CMAS former chemical composition.

CMAS Former Constituent(AFRL-02)	Chemical Composition	% by Wt.
Dolomite	$CaMg(CO_3)_2$	14
Gypsum	$CaSO_4*2H_2O$	30
Aplite	$NaAlSi_3O_8$	17
Silica	SiO_2	34
Salt	NaCl	5

Table 12. CMAS former particle size distribution. Source: [22]

Percentile	Size [µm]
10	2.5+/-1.0
50	8.5+/-1.0
90	40.5+/-3.0

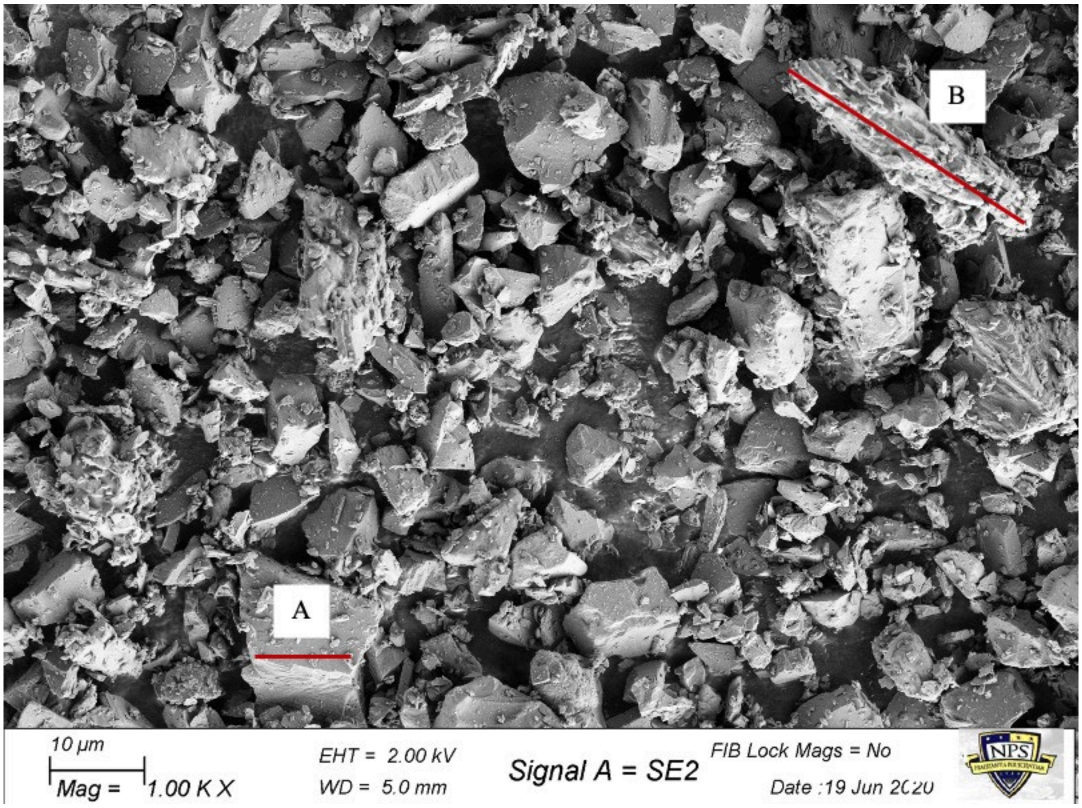

Figure 10. AFRL-02 CMAS former. Sample primarily filled with particles less than 10 µm in size with finer dust particles coasted on the surface of larger particles.(A) Rectangular particle about 10 µm with smaller particle on surface (B) Particle about 27 µm

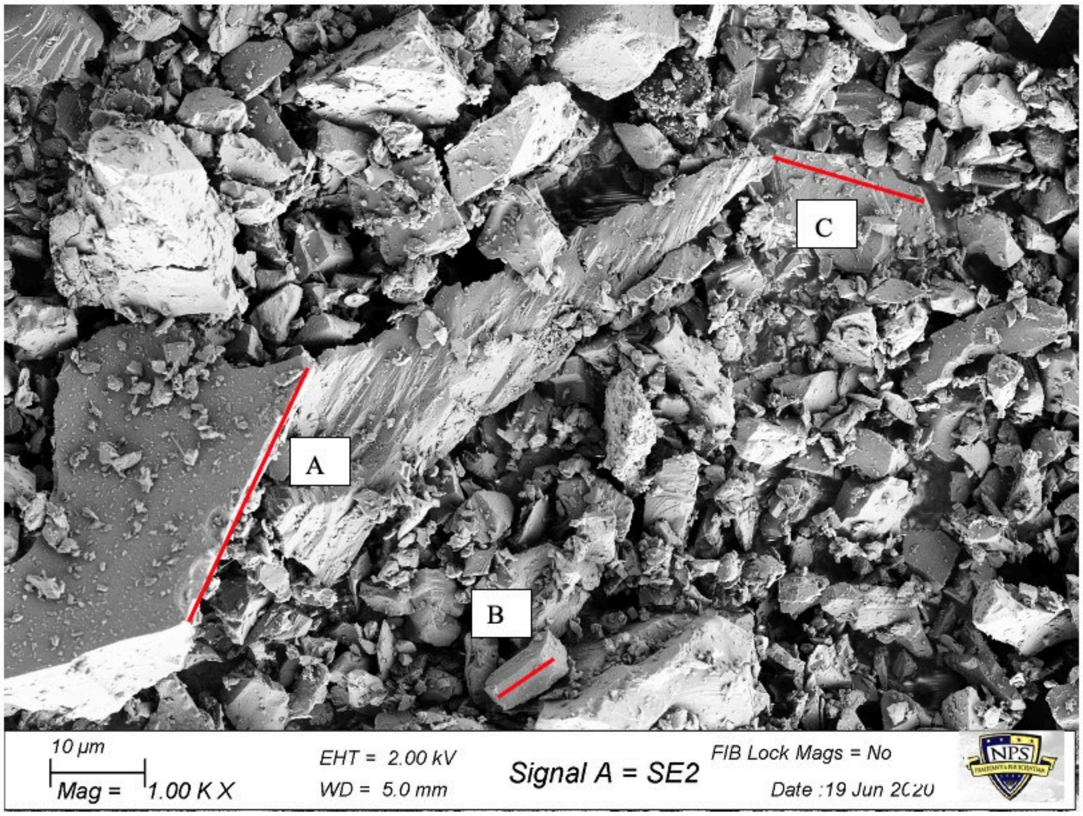

Figure 11. AFRL-02 CMAS former. Sample reveals larger particles over 10 µm in size coated with finer dust on the surface. (A) Rectangular 28 µm particle coated with finer dust on the surface.(B) Rectangular particle roughly 6 µm (C)14 µm particle coated with finer dust on the surface.

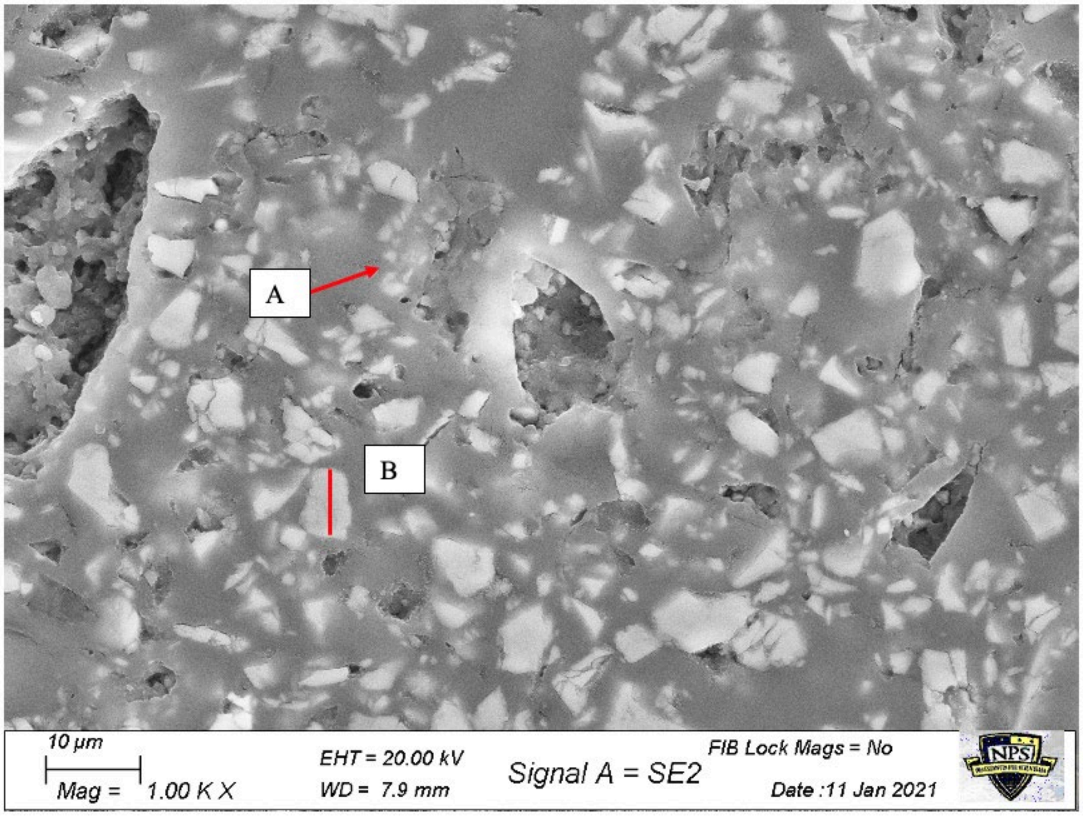

Figure 12. Cross section of AFRL-02 CMAS former. Majority of particles are rectangular in shape roughly 10 µm in size.(A) Particles less than 1 µm in size. (B) 8 µm rectangular particle.

XRD spectra of AFRL-02 CMAS former shown Figure 13 shows the major peaks of quartz, aplite, gypsum, salt, and dolomite and matches Weisner et al.[21] XRD spectra of CMAS former to include the unidentified phases between 30–40 and 60–70 degrees.

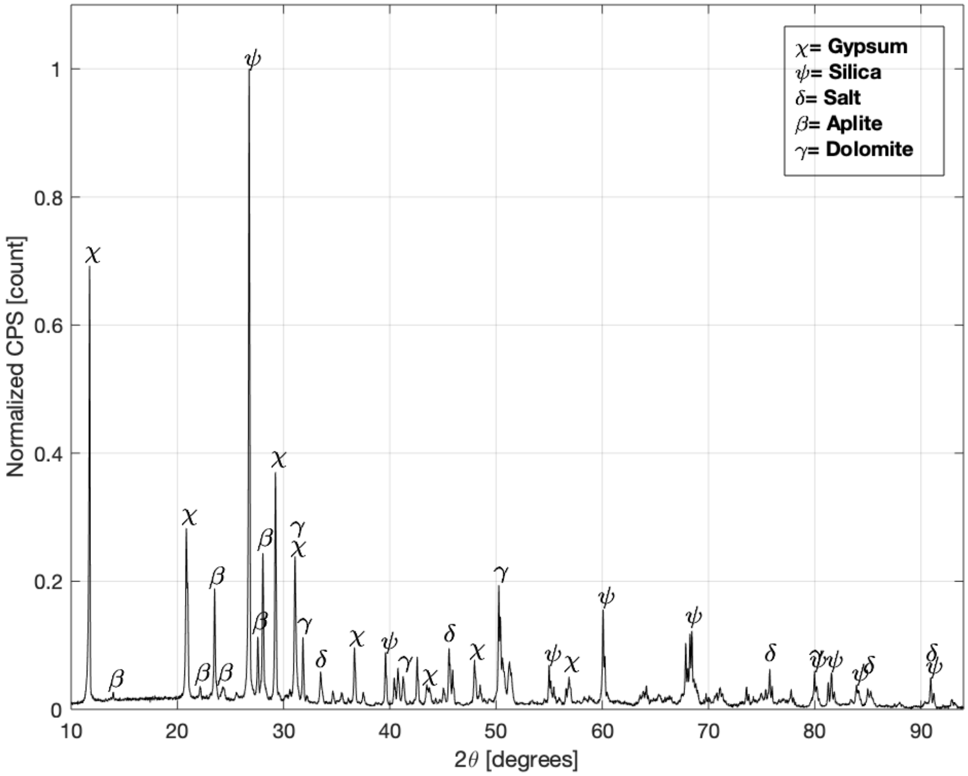

Figure 13. XRD spectra of AFRL-02 CMAS former

B. CMAS GLASS CHARACTERIZATION

After heating was complete, the CMAS former had two distinct phases. The heating produced clear glass and white crystalline phase. CMAS was then ball-mill into a fine powder containing both amorphous and crystalline CMAS. SEM images shows the majority of the particles are less than 1 µm in size and larger pieces were covered in the these small particles, shown in Figure 14 and Figure 15, with equal distribution of the constituents as shown in Figure 16 through EDS. XRD of the glass, crystalline, and CMAS are shown in Figure 17. The smaller particle are likely glass since glass is brittle and would more easily break using zirconia balls during the milling process. The larger particles observed are likely the crystalline particles.

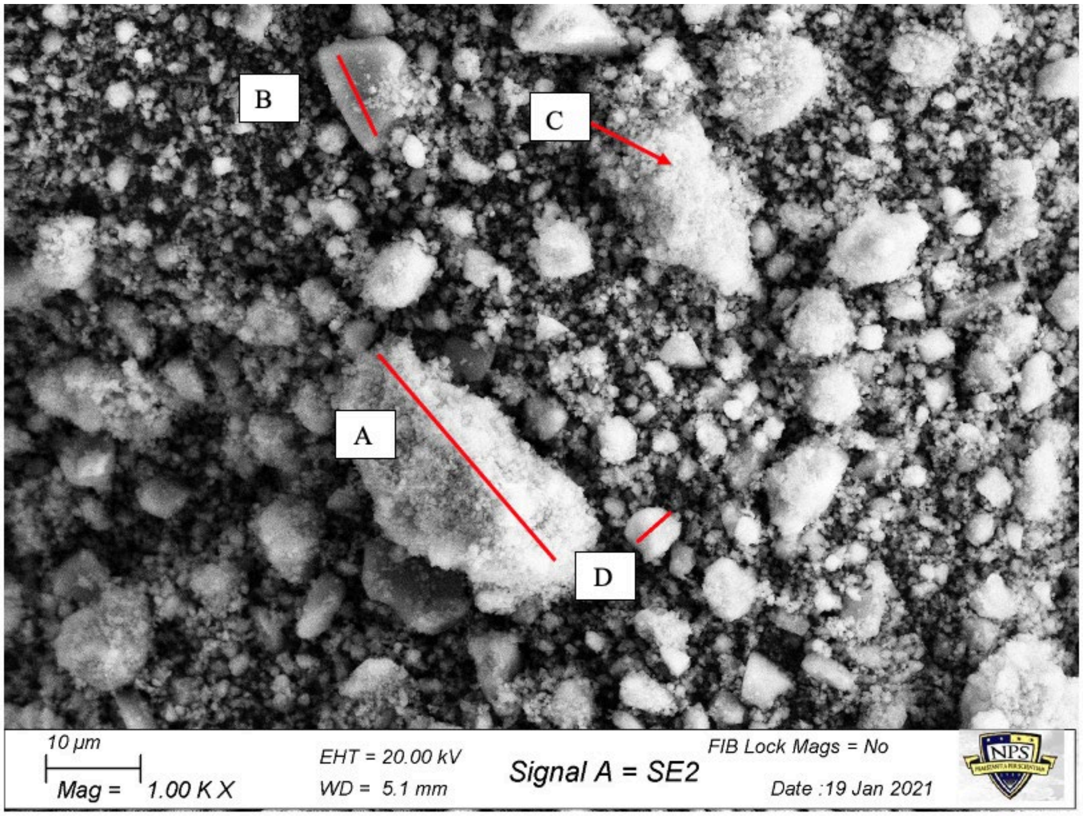

Figure 14. CMAS (A) 30 µm particle coated with homogenous CMAS glass. (B)10 µm size particle. (C) Majority of the sample is composed a CMAS glass less than 1 µm in diameter and can be seen coated on the larger size particles.(D) 6 µm CMAS particle.

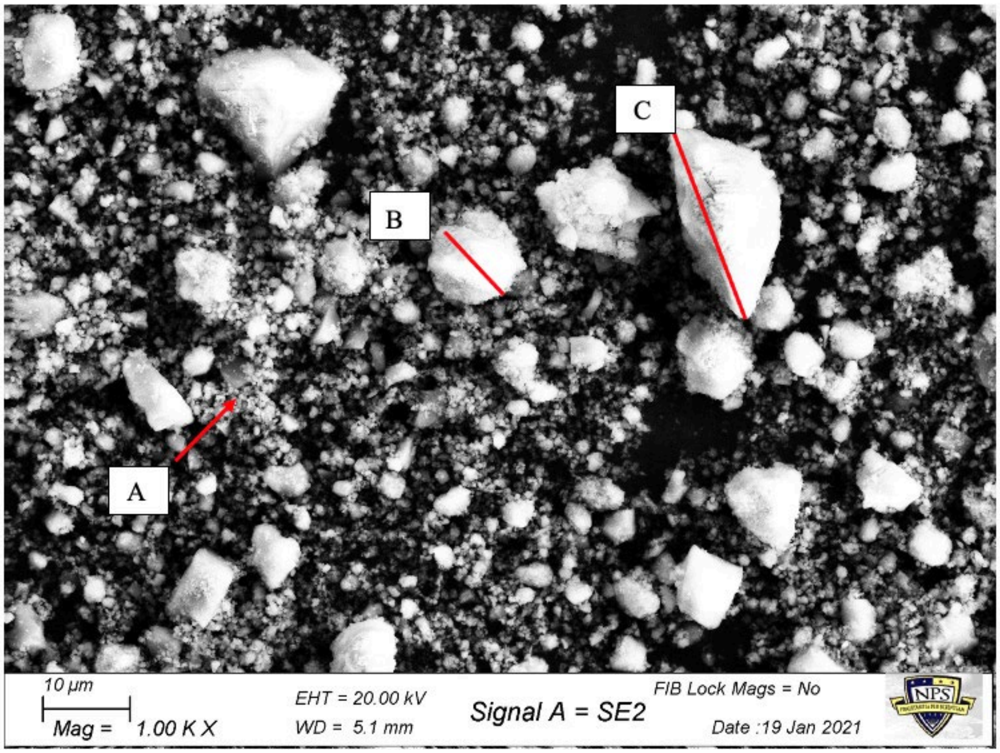

Figure 15. (A) CMAS glass less than 1 µm in diameter (B)10 µm size particle. (C).20 µm size particle.

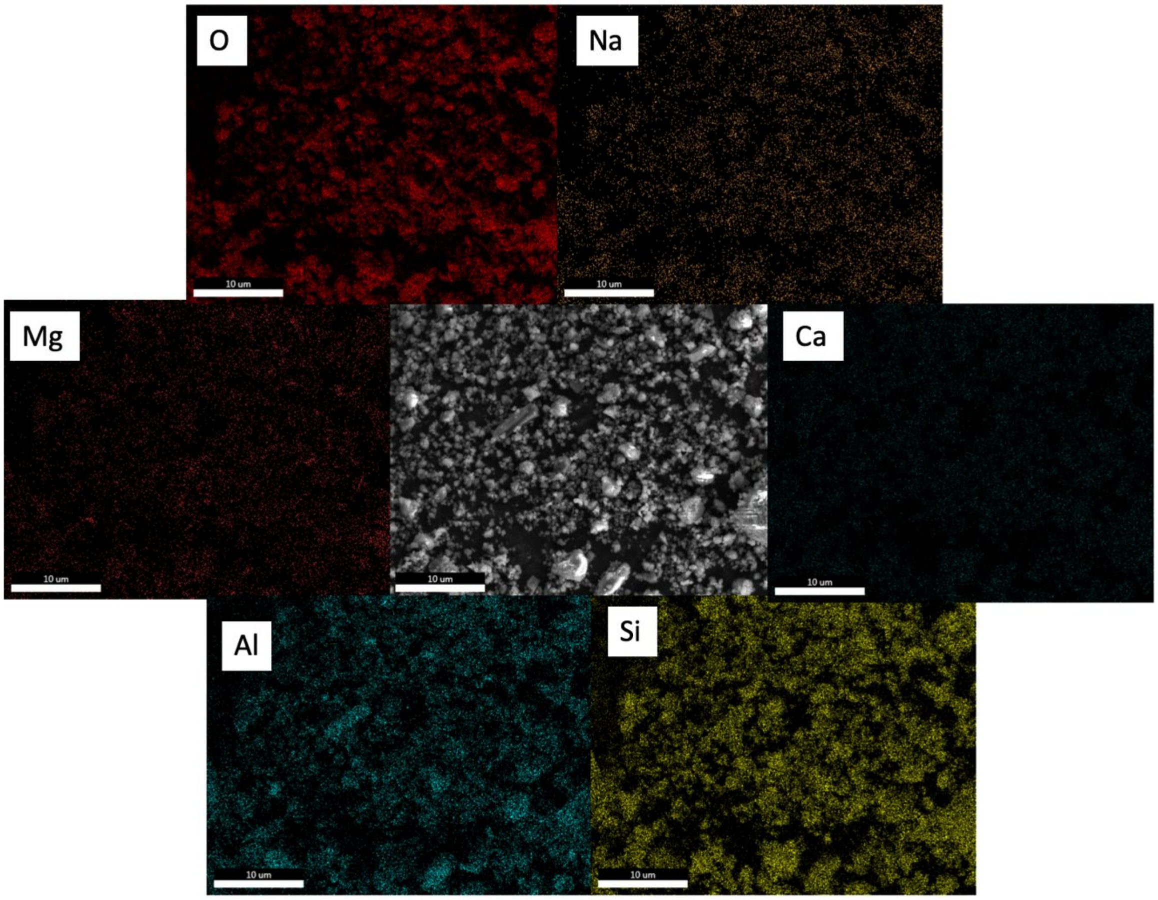

Figure 16. EDS spectra of CMAS glass and crystalline. Equal distribution of the constituents shows the sample is homogenous and amorphous.

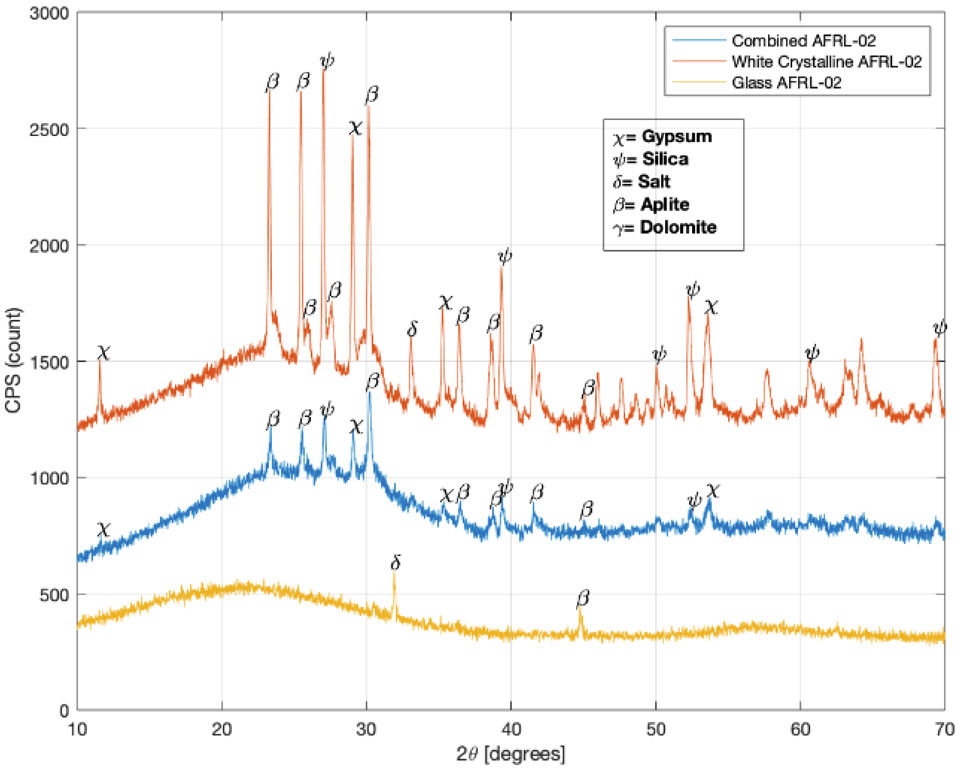

Figure 17. XRD spectra of CMAS, white crystalline, and glass

CMAS glass, as shown Figure 17, is homogenous with two peaks correlating to salt and aplite. The white crystalline shows several phases correlating to silica, gypsum, aplite peaks. Both samples were ball milled together into fine powder to so the trials can best simulate CMAS attack seen in the environment, which consists of both crystalline (mineral) CMAS formers and amorphous CMAS. Figure 18 shows the difference in relative intensities between CMAS and CMAS former crystalline peaks indicating a clear emergence of a broad amorphous region in CMAS.

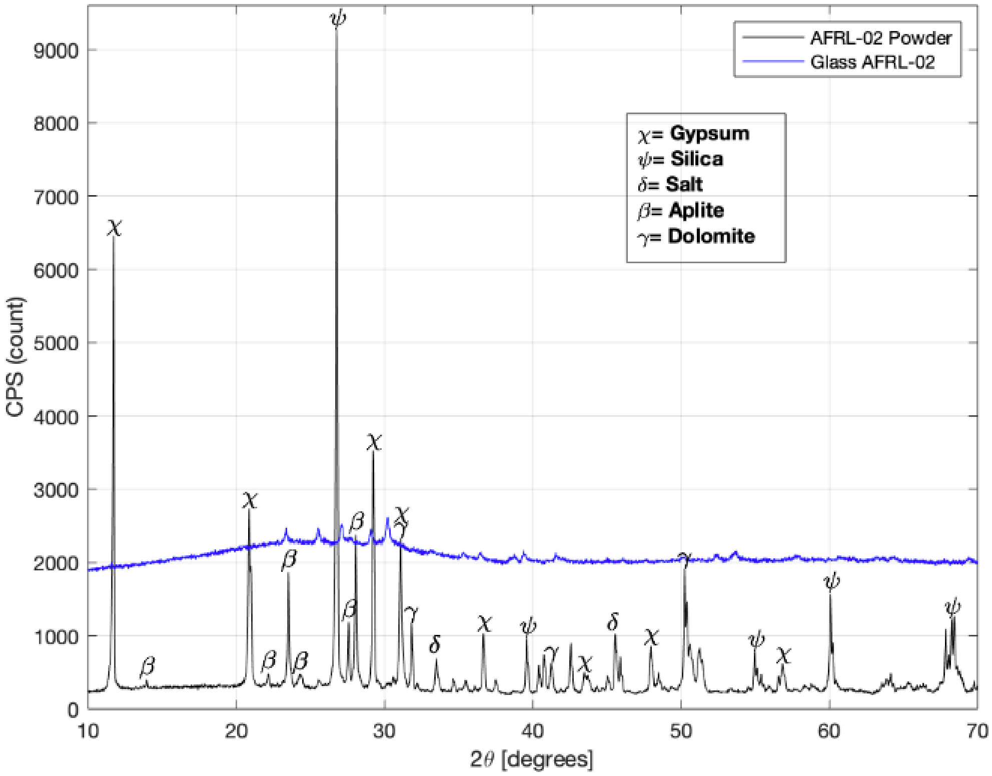

Figure 18. XRD spectra of CMAS former vs. CMAS

C. HAFNIUM DIBORIDE AND ZIRCONIUM DIBORIDE CHARACTERIZATION

XRD analysis, shown in Figure 21 and Figure 24, of the powders revealed the powders were pure HfB_2 and ZrB_2 with no other constituent present in the sample. HfB_2 is mostly composed of small grains under 1 µm with some particles over 5 µm as shown in Figure 19 and Figure 20. ZrB_2 particles are significantly larger than HfB_2 with majority of the particles over 20 µm in size and finer particle coated on the surface as shown in Figure 22 and Figure 23.

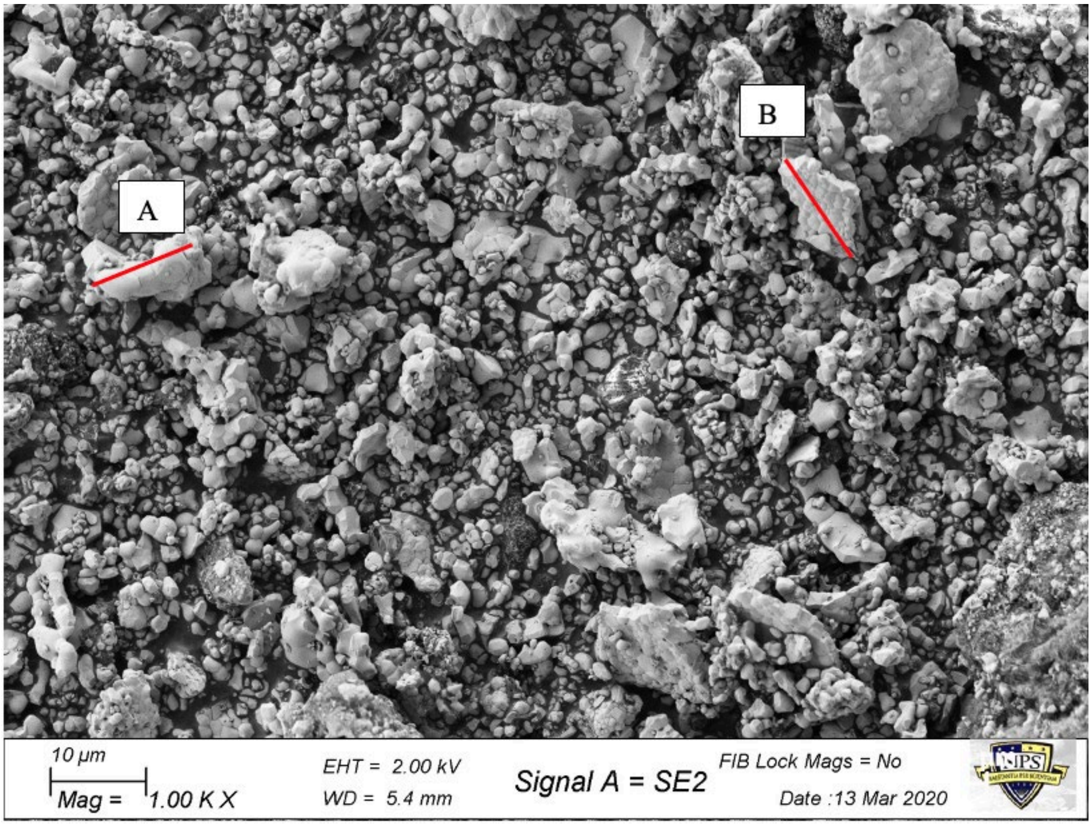

Figure 19. SEM image of HfB_2. Majority of the particles are smaller than 1 µm. (A) Particle is 10 µm is size. (B) Particle measures 12 µm in size.

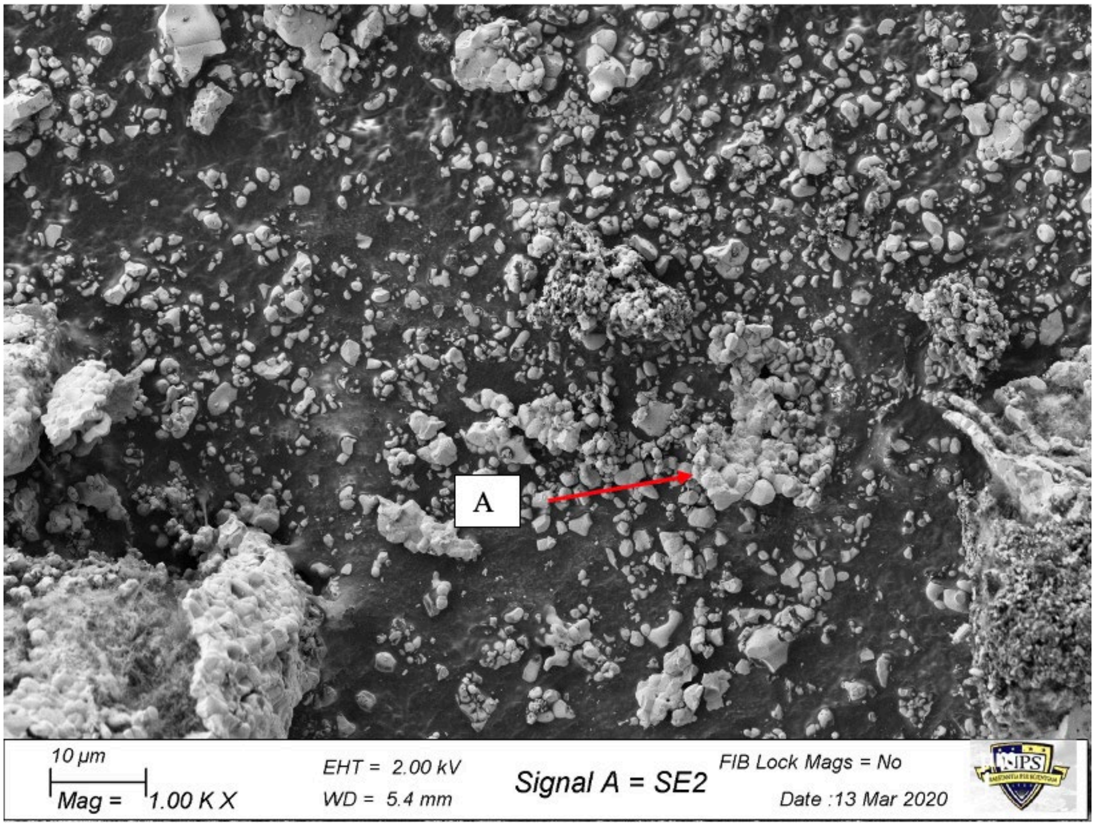

Figure 20. SEM image of HfB_2. (A) Majority of particle sizes are less than 1 µm in size and hexagonal in shape.

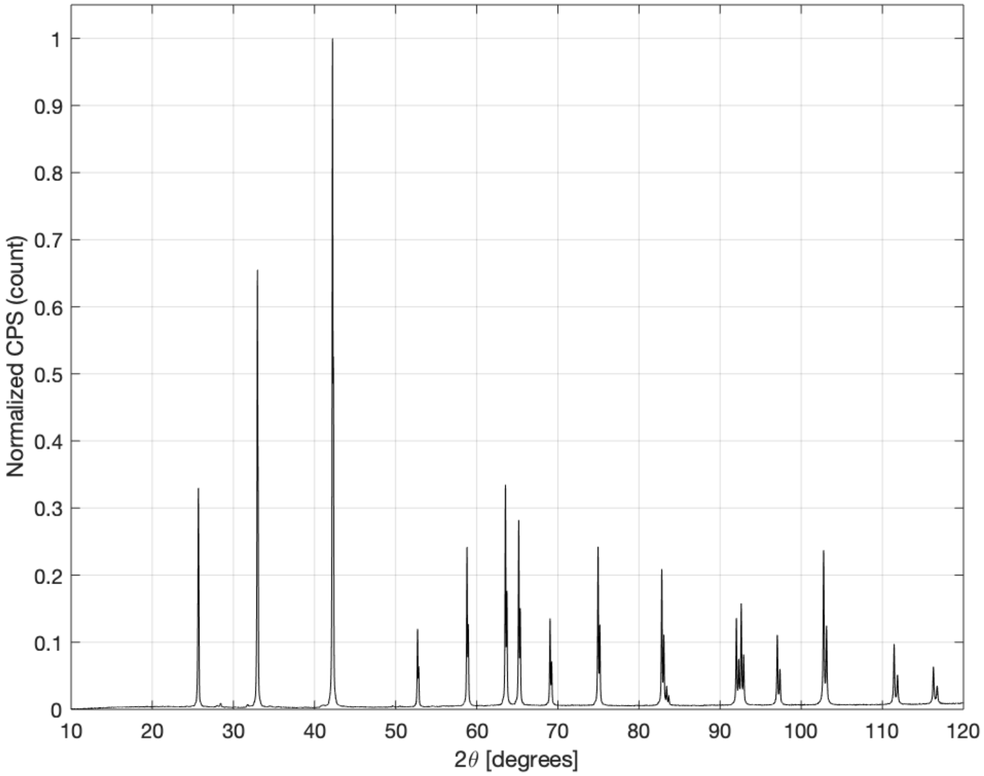

Figure 21. XRD spectra of HfB_2

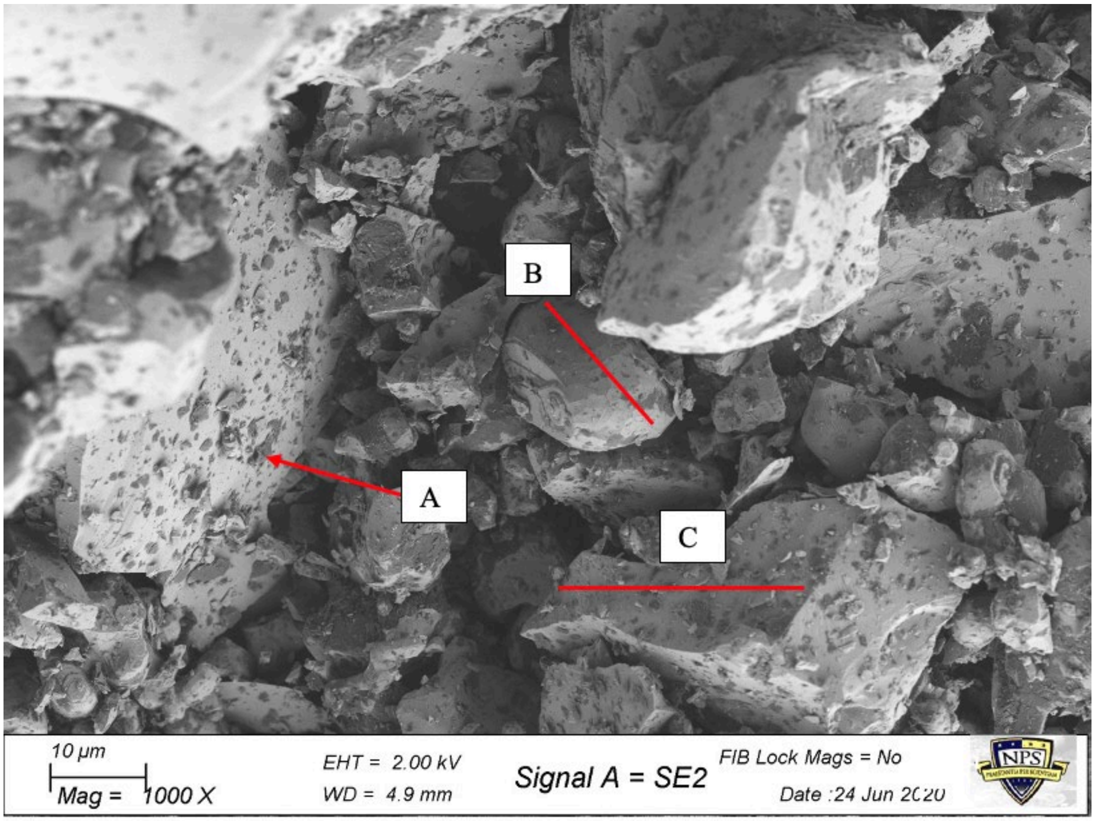

Figure 22. SEM image of ZrB_2 (A) Small particles can be seen coated on the surface of the larger particle through the sample. (B) 14 µm size sample (C) 22 µm size sample.

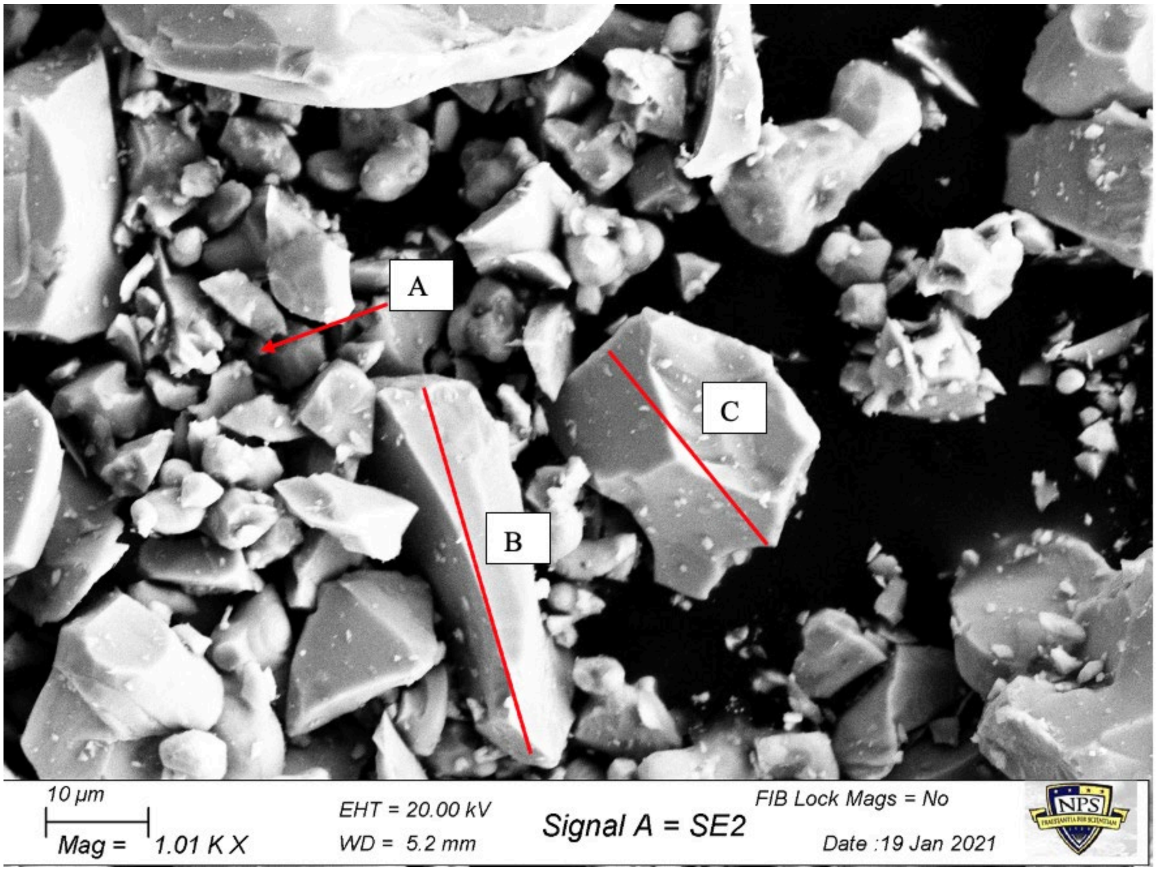

Figure 23. SEM image of ZrB_2 (A) Small irregular size particles less than 10 µm. (B) 40 µm size particle. (C) 23 µm size particle.

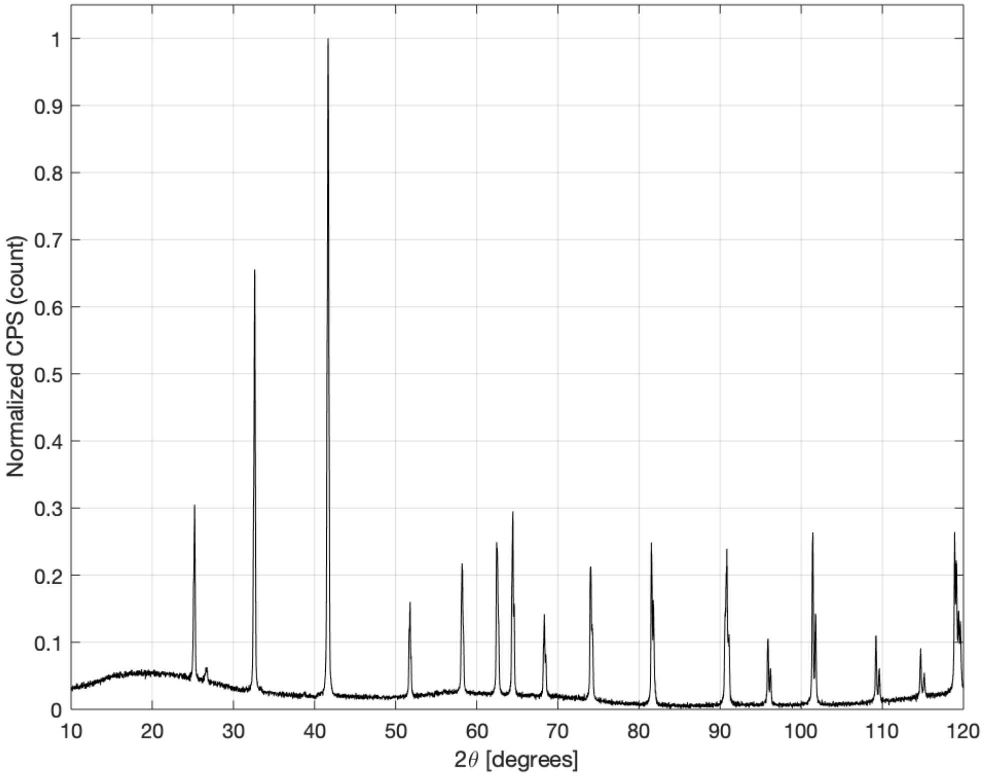

Figure 24. XRD spectra of ZrB_2

D. HFB₂ CMAS INTERACTION

1. 1000°C Isothermal Hold

Figure 26 shows the sample after removed from the furnace. The powder appears to sinter completely with smaller particles visible on the surface. XRD of the sample, shown in Figure 25, reveals the apparent reaction with the oxygen and HfB_2 yielding a monoclinic phase of HfO_2 correlating with experimental findings from Bargeron et al.[29] There are still peaks correlating to HfB_2 with a weaker intensity compared to Figure 20 indicating not all HfB_2 has been completely oxidized during the 1 hour 1000°C exposure. This test suggests CMAS does not interact with HfB_2 at 1000°C as no new phases were identified during XRD analysis. SEM images, shown in Figure 27, shows HfB_2 that has oxidized into HfO_2.

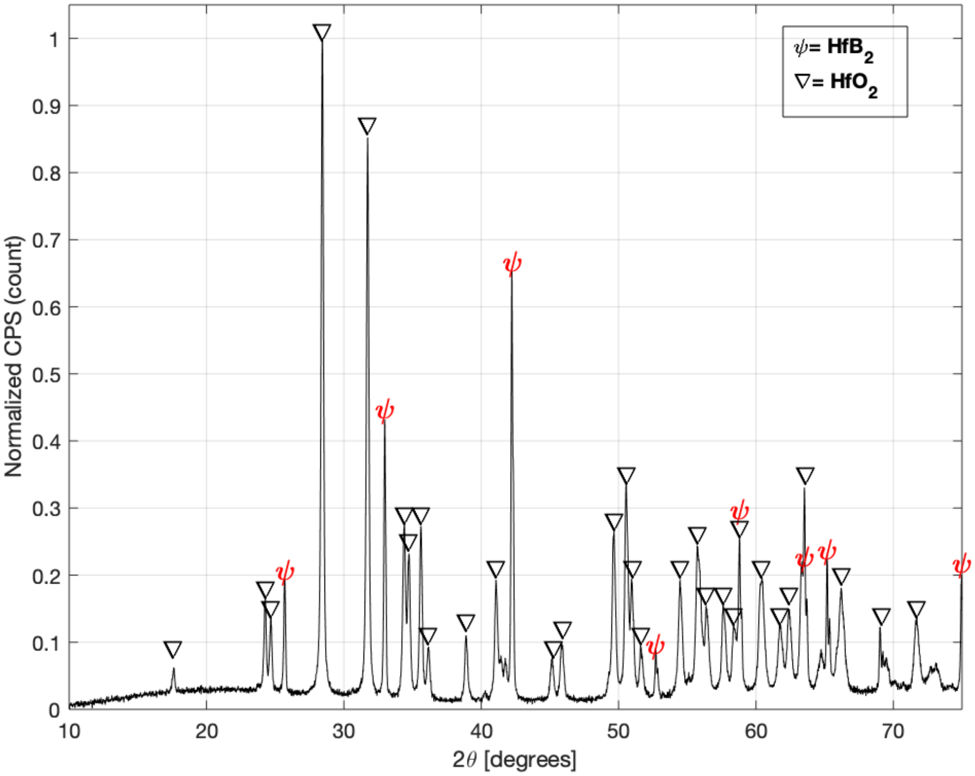

Figure 25. XRD spectra of HfB$_2$+CMAS at 1000°C 1 hour isothermal hold. The slight curvature over 15–30 degrees corelates to amorphous CMAS. No new phase indicates there is no reaction between CMAS and HfB$_2$. Oxidation product from the heat yield monoclinic HfO$_2$.

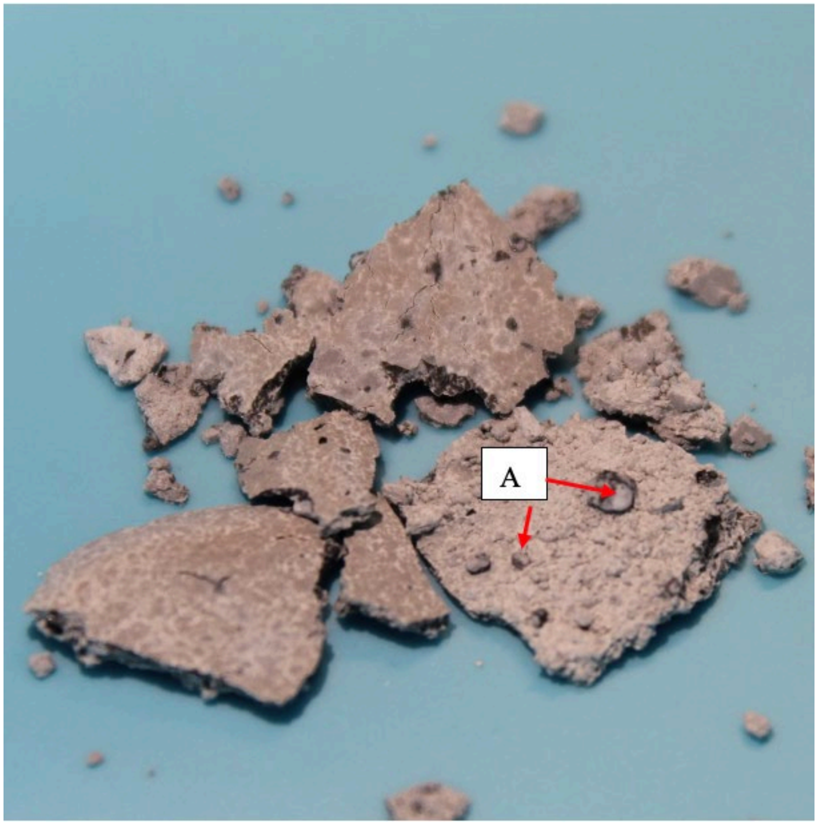

Figure 26. HfB_2 held at 1000°C for 1 hour. (A) Small size particles visible on the surface of the sample.

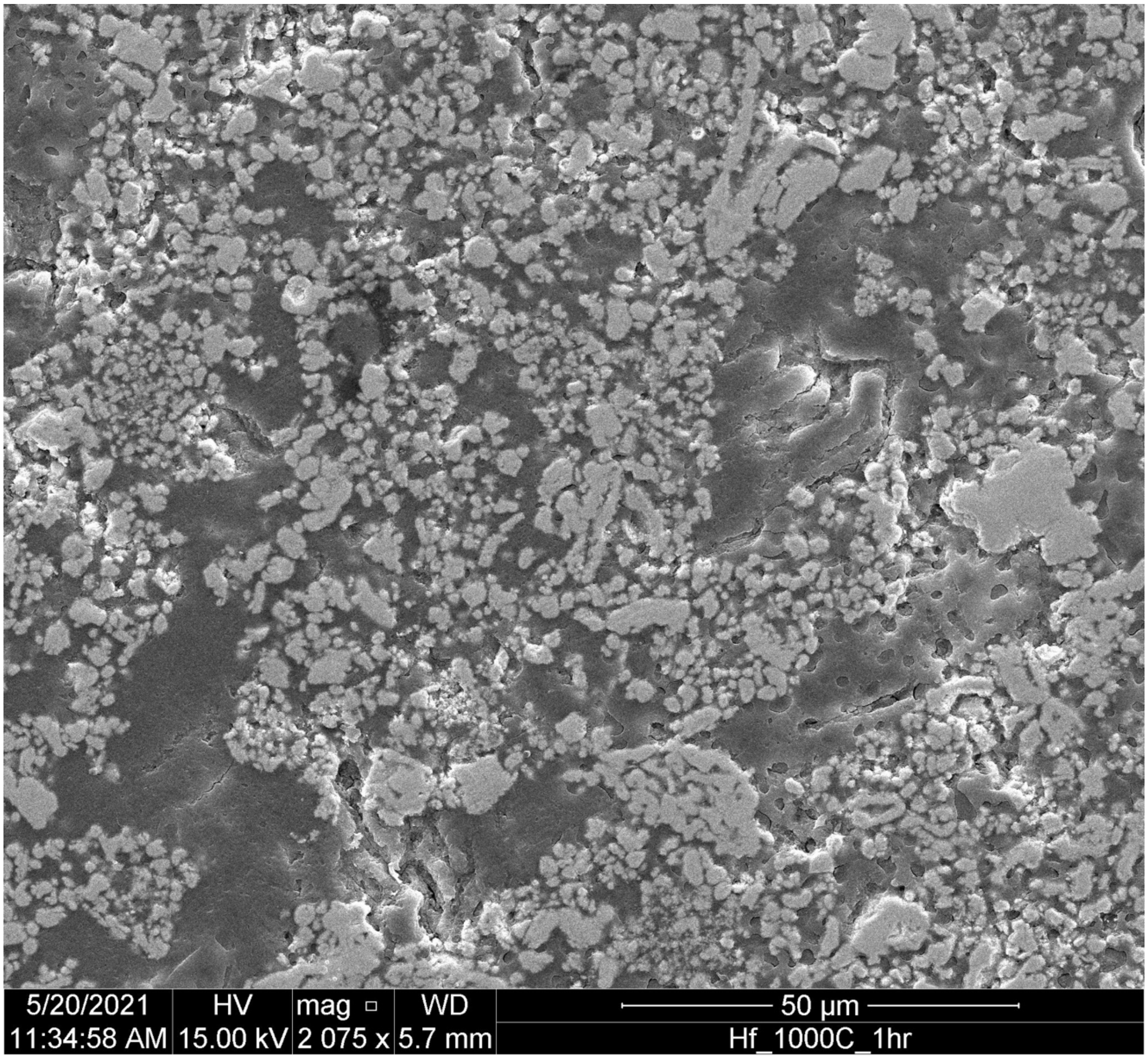

Figure 27. HfB_2 particles are oxidizing into HfO_2.

Using the same ramp up rate, the sample was held isothermally at 1000°C for 10 hours. Figure 29 shows the resulting powder after the run and shows almost no physical differences from Figure 26. However, an XRD analysis, shown in Figure 28, shows a tetragonal phase of $HfSiO_4$ indicating that CMAS constituents containing Si interacted with HfO_2. The plot also shows that not all HfB_2 has oxidized into HfO_2.

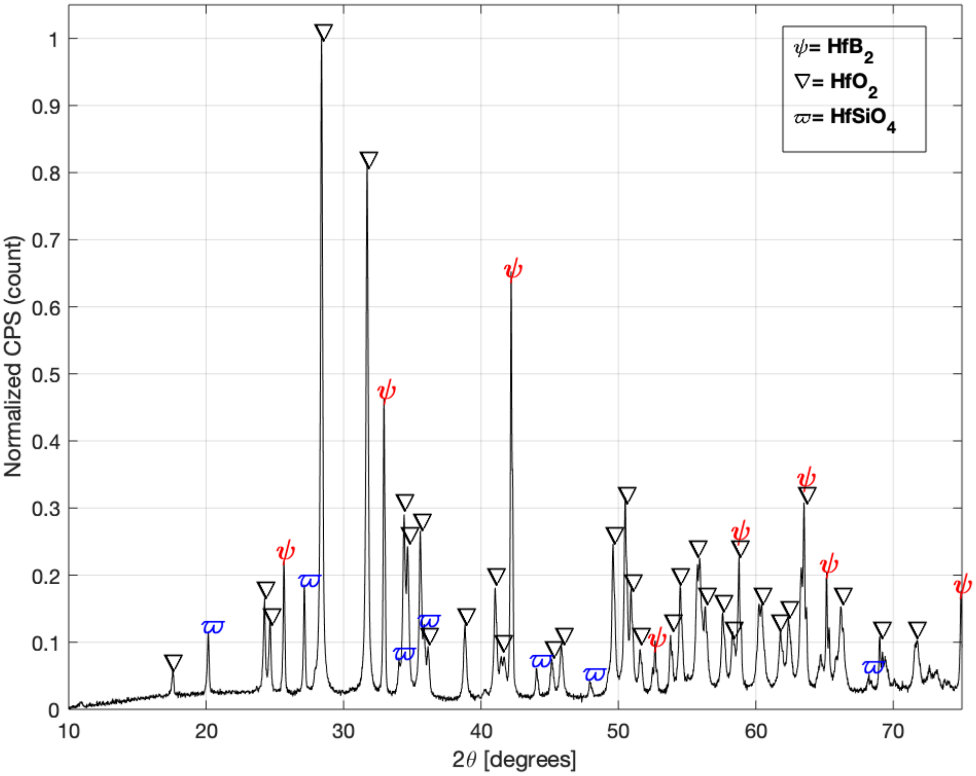

Figure 28. XRD spectra of HfB_2+CMAS at 1000°C 10-hour isothermal hold. The slight curvature over 15–30 degrees corelates to CMAS. Oxidation product from the heat yield monoclinic HfO_2. The new phase tetragonal $HfSiO_4$ suggest a reaction between HfO_2 and CMAS.

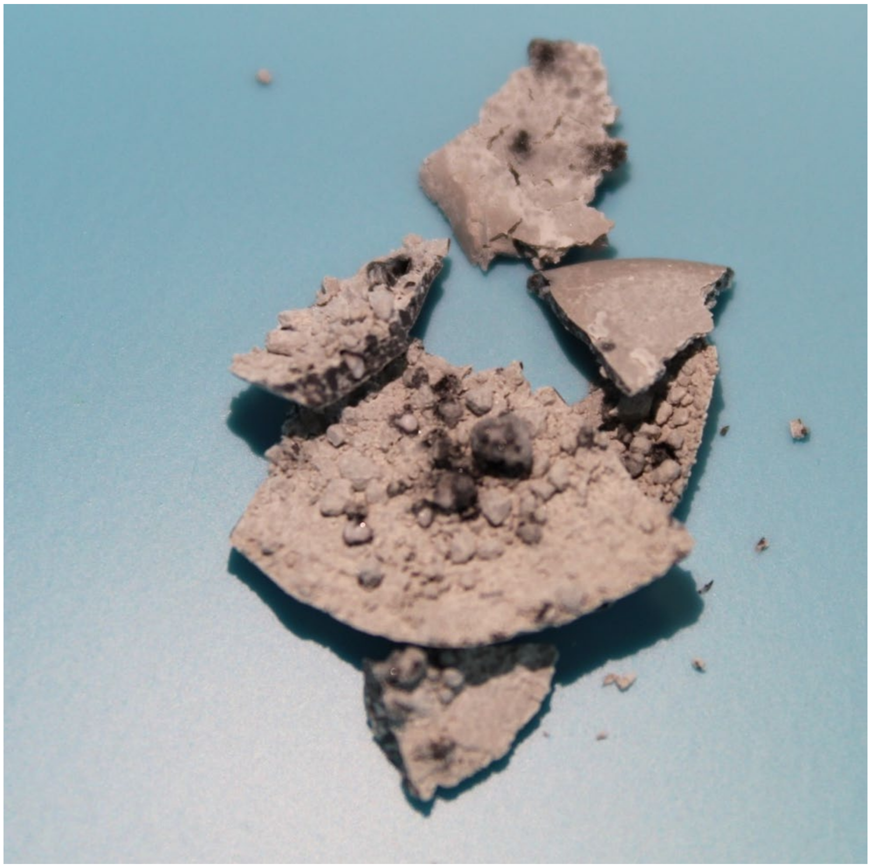

Figure 29. HfB_2 held at 1000 °C for 10 hours. There is no physical difference compared to Figure 25.

For the final run at 1000°C, the sample, shown in Figure 31, was held for 100 hours. Like with the 10-hour run, the same products resulted from the 100 hours isothermal run with different intensities as shown in Figure 30. The strongest intensities correlating to HfO_2 and $HfSiO_4$ with weak peaks correlating to HfB_2 implying almost all of HfB_2 oxidized into HfO_2.

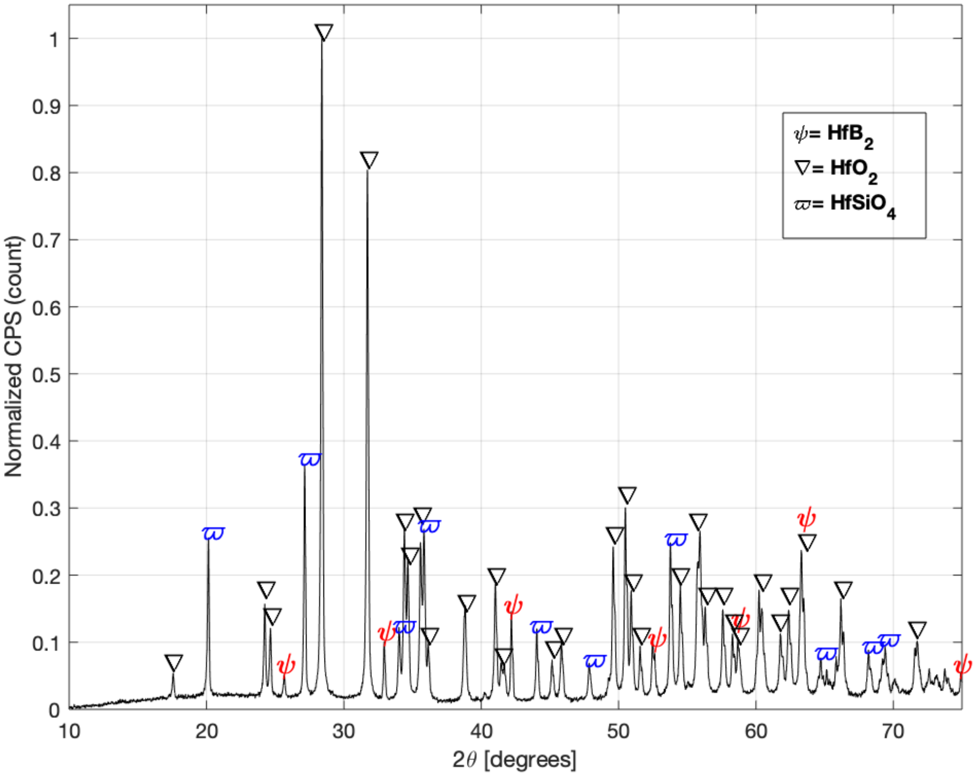

Figure 30. XRD spectra of HfB_2+CMAS at 1000°C 100-hour isothermal hold. CMAS continues to interact with HfO_2 and produced stronger tetragonal $HfSiO_4$ peaks.

Figure 31. HfB_2 held at 1000°C for 100 hours. No major physical changes to the sample.

2. 1300°C Isothermal Hold

The sample, like previous runs, did not show any significant physical changes as shown in Figure 33. Using XRD, the sample yielded the same products with no reaction with between HfO_2 and CMAS from 1000°C one hour run despite increasing the temperature to 1300°C as shown in Figure 32.

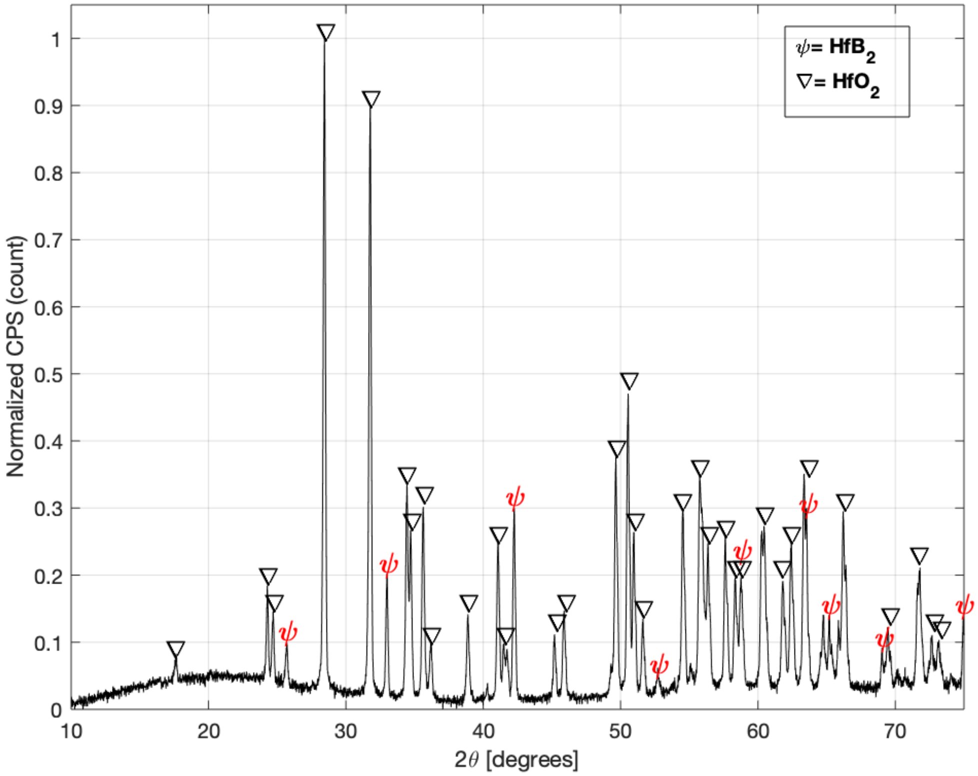

Figure 32. XRD spectra of HfB_2+CMAS at 1300°C 1 hour isothermal hold. Oxidation product from the heat yield monoclinic HfO_2. No reaction between CMAS and HfB_2.

Figure 33. HfB$_2$ held at 1300 °C for 1 hour. There are no noticeable physical changes compare from the 1000°C heated samples.

The ten-hour isothermal hold also matched the results from the 1000°C ten-hour isothermal hold with HfO$_2$ reacting with the CMAS to yield tetragonal phase HfSiO$_4$ shown in Figure 34. Figure 35 also shows almost no physical changes in the sample. SEM analysis shows the articles increasing in size with is HfO$_2$ reacting with CMAS to form HfSiO$_4$ are seen in Figure 36.

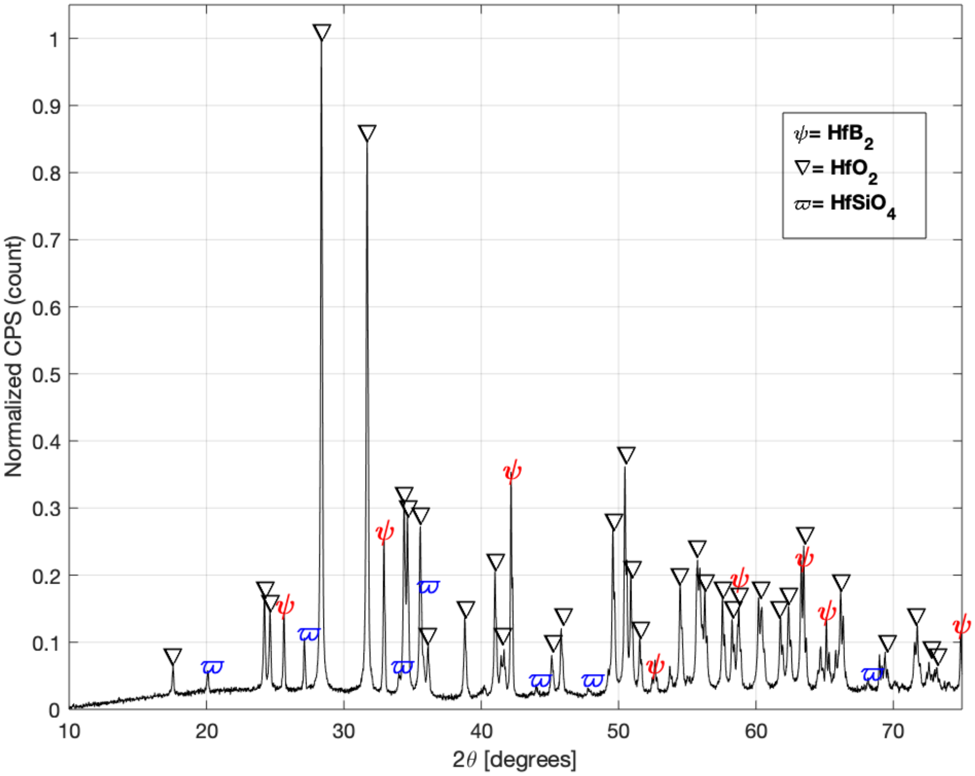

Figure 34. XRD spectra of HfB_2+CMAS at 1300°C 10 hour isothermal hold. CMAS did interact with HfO_2 and produced tetragonal $HfSiO_4$.

Figure 35. HfB_2 held at 1300 °C for ten hours.

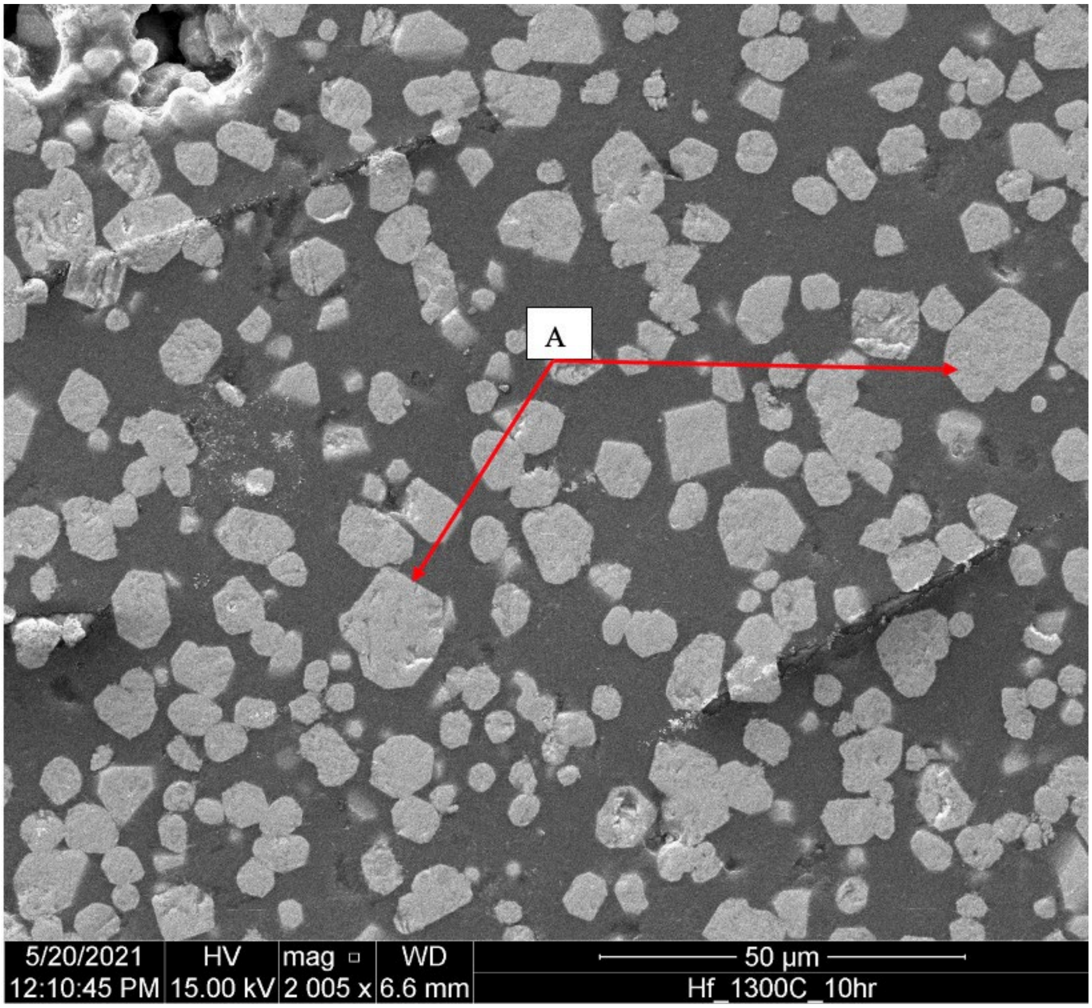

Figure 36. (A) HfO_2 observed.

Like with the previous runs, the 100-hour isothermal hold also matched the results from the 1000°C 100-hour isothermal hold with HfO_2 reacting with the CMAS to yield tetragonal phase of $HfSiO_4$ shown in Figure 37. Strongest peaks correlate to $HfSiO_4$ instead of HfO_2 indicating the duration allowed for more interaction between HfO_2 and CMAS. The sample also appears to have a glassy film, a possible mixture of CMAS glass and B_2O_3, on the surface of the sample with porous holes indicating B_2O_3 transitioning into a gas and escaping from the sample shown in Figure 38. Additional SEM images were taken, Figure 39, and $HfSiO_4$ was observed with HfO_2.

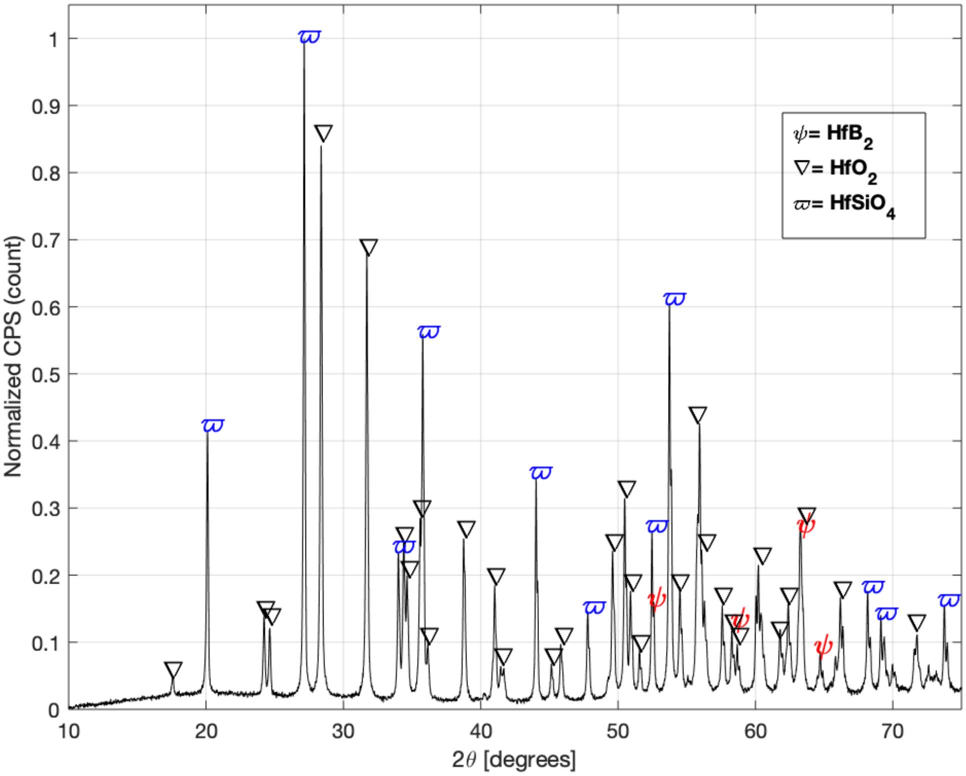

Figure 37. XRD spectra of HfB_2+CMAS at 1300°C one-hundred-hour isothermal hold. CMAS did interact with HfO_2 and produced tetragonal $HfSiO_4$. Stronger intensity for $HfSiO_4$ shows a greater amount of CMAS is reacting with HfO_2

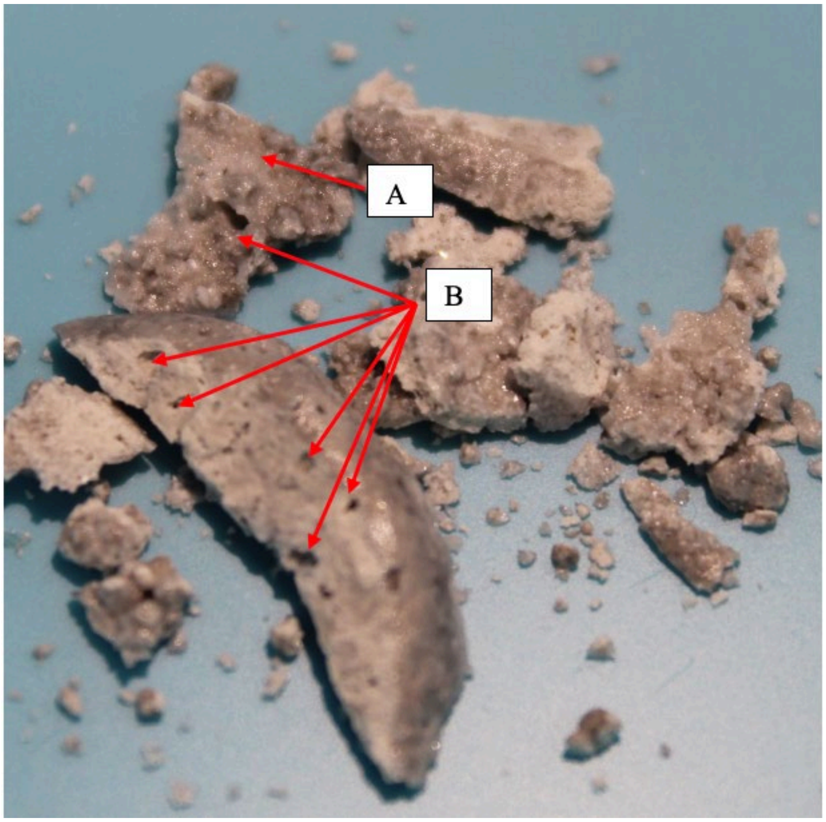

Figure 38. HfB_2 held at 1300 °C for 100 hours. (A) Milky glassy film on the surface on the surface of the sample. (B) Porous holes seen on the sample likely a result of gaseous B_2O_3.

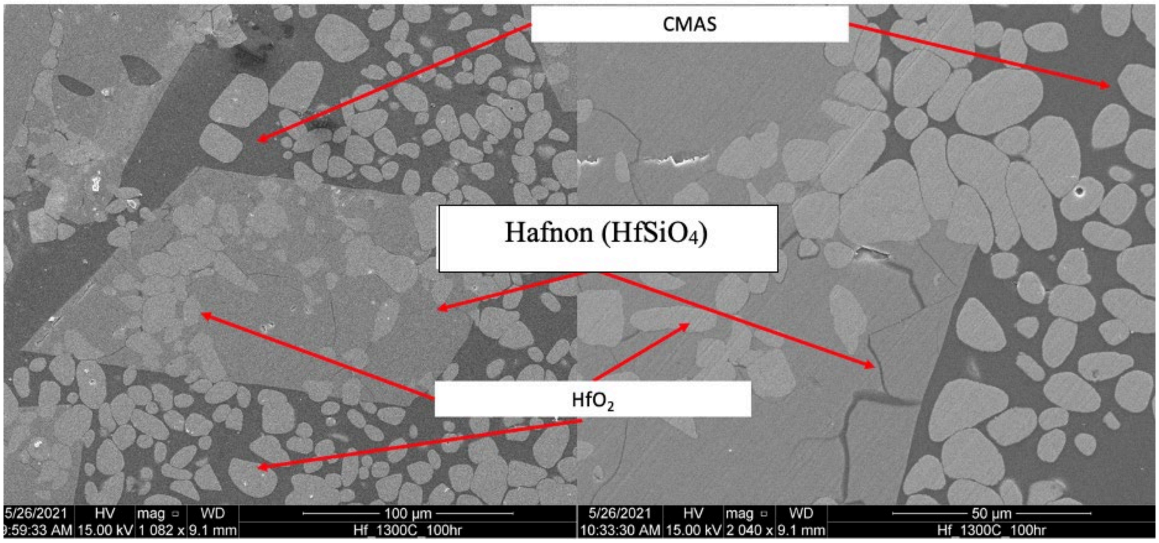

Figure 39. $HfSiO_4$ is shown. HfO_2 is shown inside $HfSiO_4$.

3. 1600°C Isothermal Hold

The experiment, shown in Figure 41, yielded the same results from the 1000°C and 1300°C one hour runs. HfB_2 oxidized with the ambient air and produced HfO_2 but did not react with the CMAS. Figure 40 shows the identified phases from the run with all major peaks correlating to both HfB_2 and HfO_2.

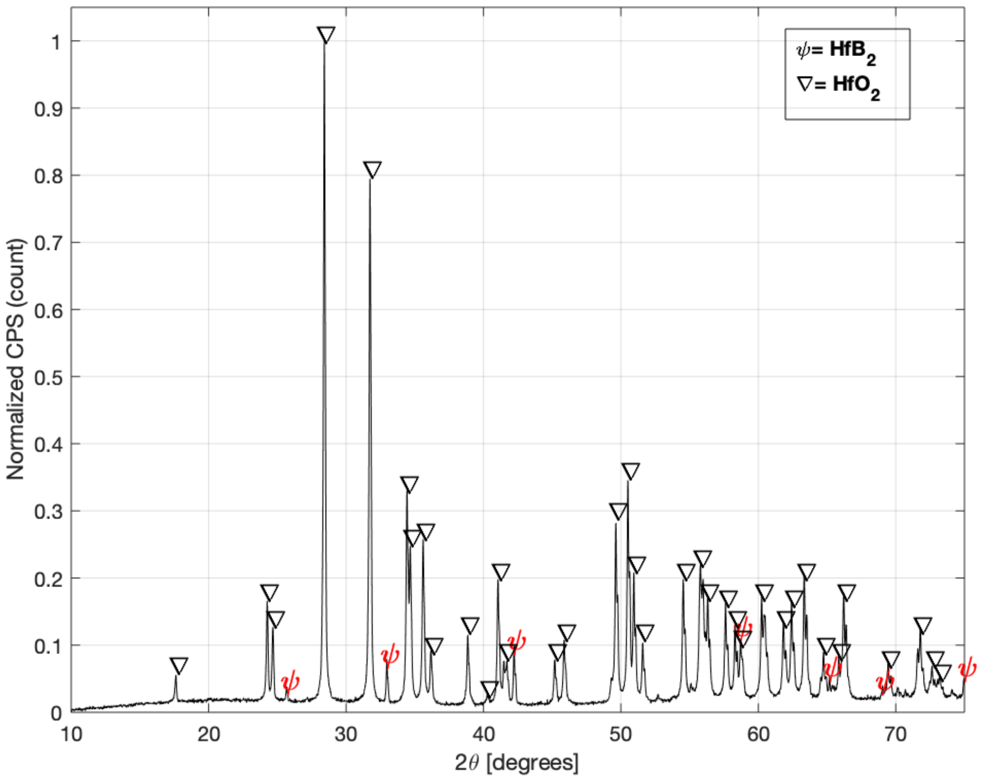

Figure 40. XRD spectra of HfB_2+CMAS at 1600°C 1 hour isothermal hold. Oxidation product from the heat yield monoclinic HfO_2. Like with previous one hour runs, CMAS did not interact with HfO_2 to produce $HfSiO_4$.

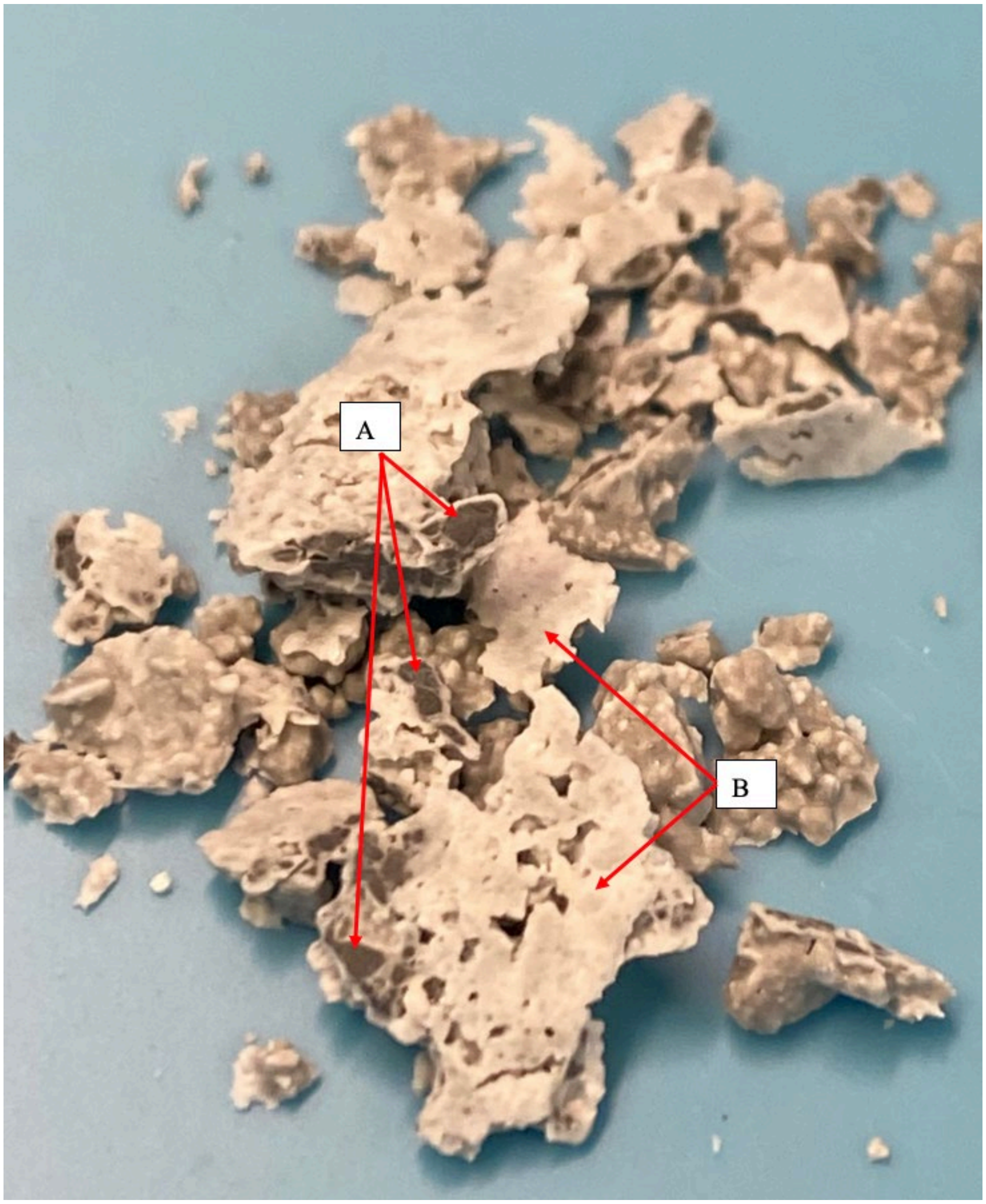

Figure 41. HfB_2 held at 1600 °C for 1 hour. (A) Darker sample shows HfB_2 that has not oxidized. (B) Lighter sample correlates to HfO_2.

For the ten-hour run, HfB_2 , shown in Figure 43, continued to be oxidized. With a longer time duration and more oxidation, the product began to react with CMAS to yield $HfSiO_4$ as seen with the previous ten hour runs at 1000°C and 1300°C. Figure 42 shows the major peaks from XRD correlating to both HfO_2 and $HfSiO_4$.

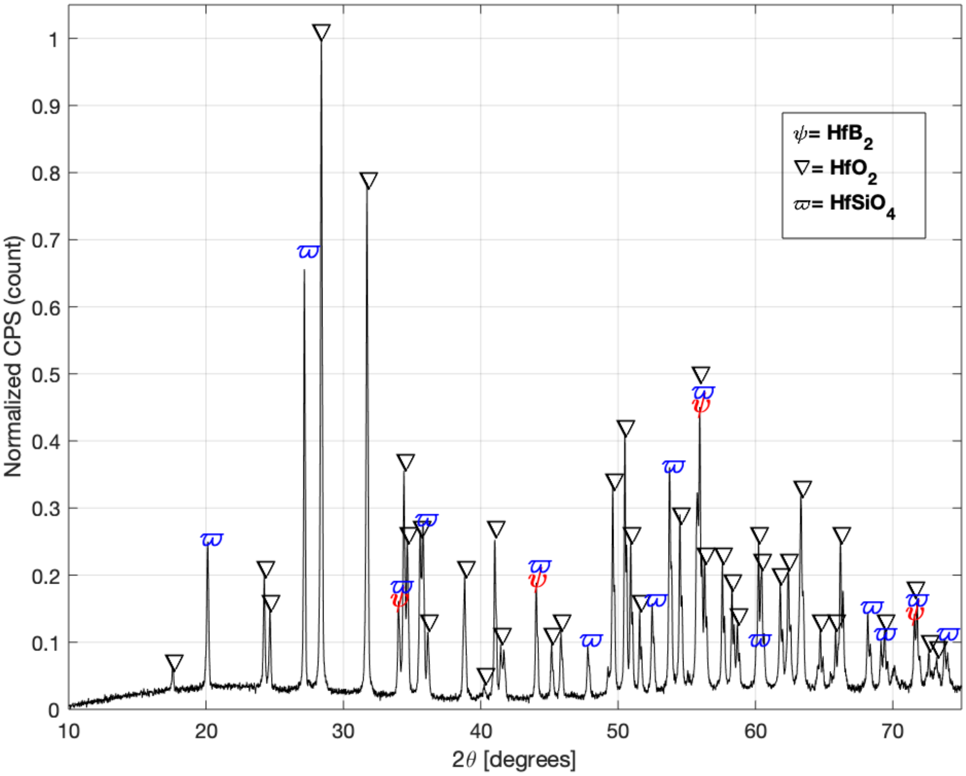

Figure 42. XRD spectra of HfB_2+CMAS at 1600°C 10-hour isothermal hold. Oxidation product from the heat yield monoclinic HfO2. CMAS interacted with HfO_2 to produce tetragonal $HfSiO_4$.

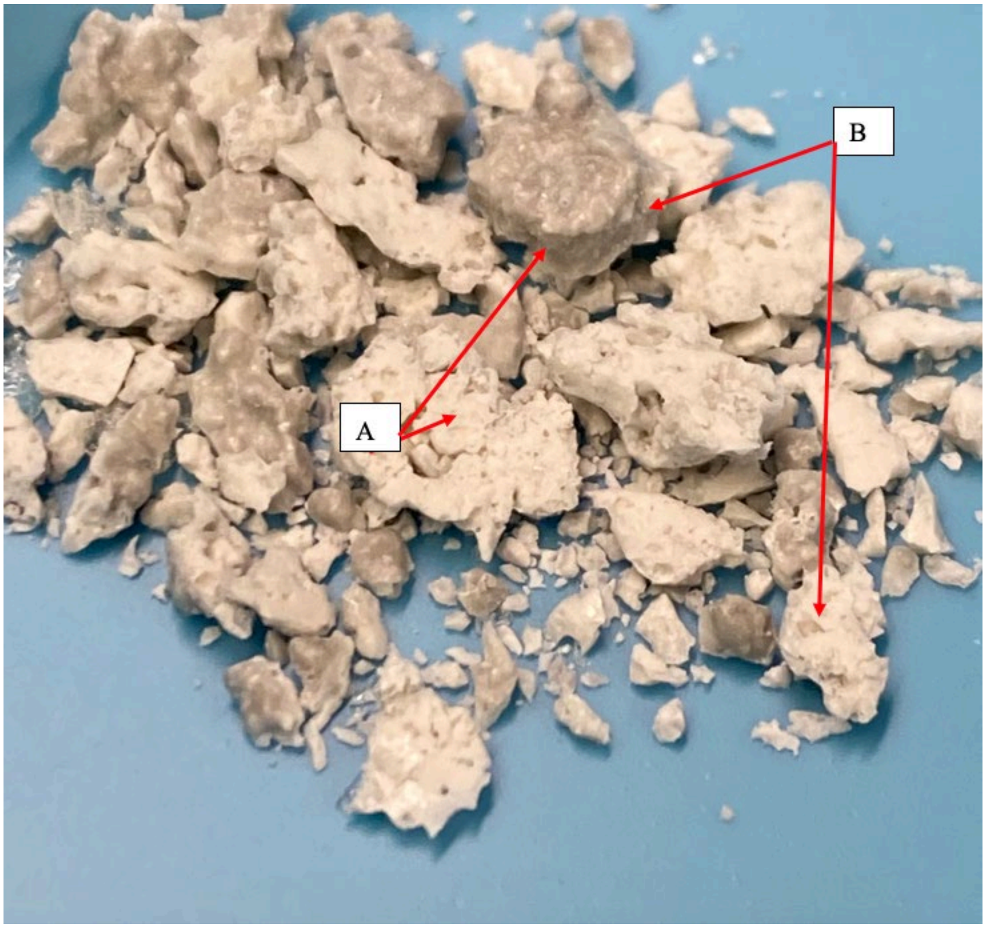

Figure 43. HfB_2 held at 1600 °C for 10 hours. (A) Porous holes seen inside the sample. (B) Darker material seen on the surface of the sample.

The 100 hours isothermal hold yielded different results from the previous 100 hours runs. The intensity peaks from Figure 44 shows heavy oxidation but weaker peaks correlating to $HfSiO_4$ suggesting HfO_2 did not interact with CMAS as heavily with previous runs. The sample, shown in Figure 45, displayed more porous holes indicating B_2O_3 formed and escaped as gas. SEM analysis, shown in Figure 46, shows very little HfB_2 and mostly HfO_2.

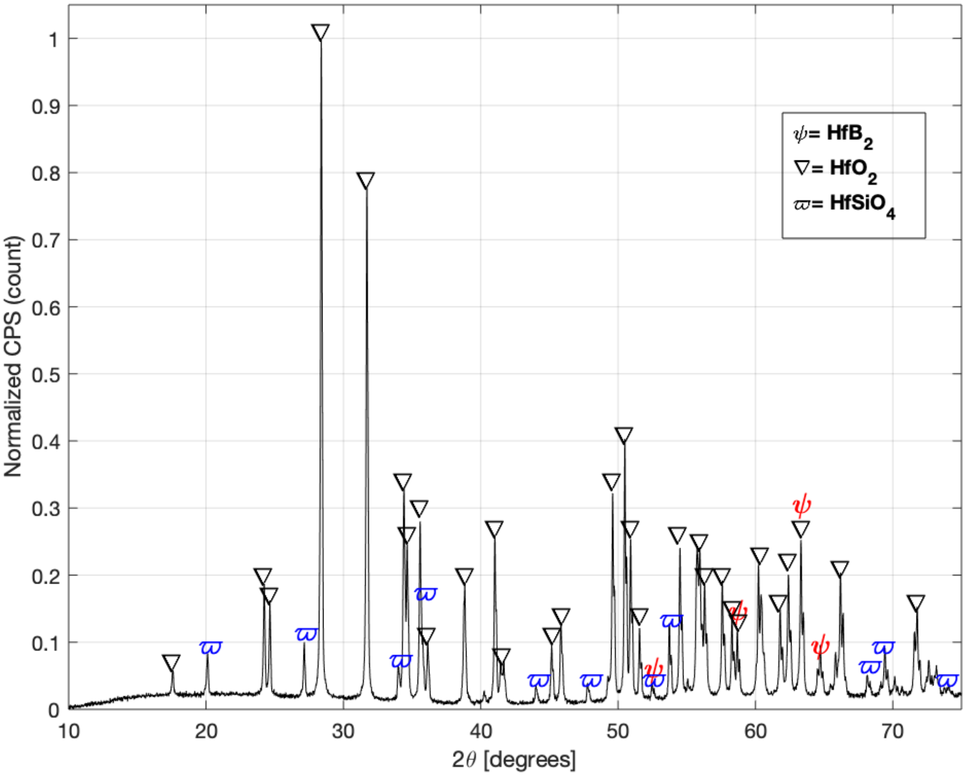

Figure 44. XRD spectra of HfB_2+CMAS at 1600°C 100 hour isothermal hold. Oxidation product from the heat yield monoclinic HfO2. CMAS interacted with HfO_2 to produce tetragonal $HfSiO_4$.

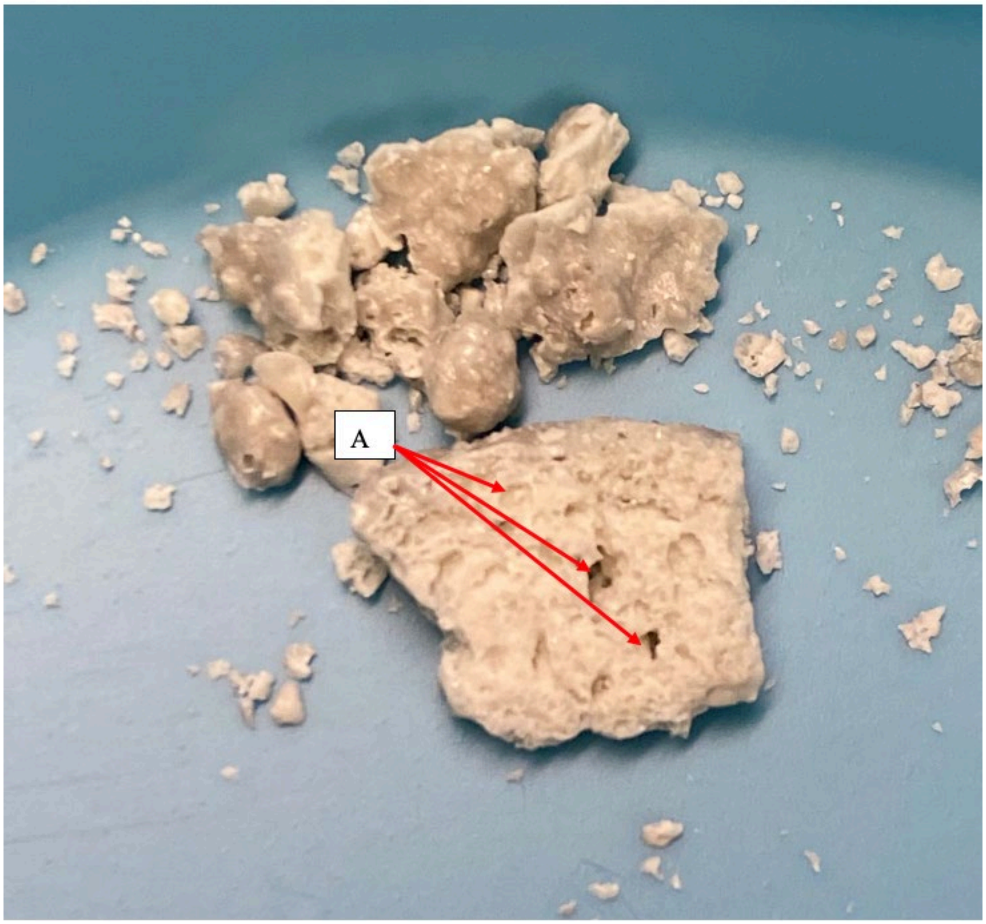

Figure 45. HfB_2 held at 1600°C for 100 hours. (A) Larger porous holes observed.

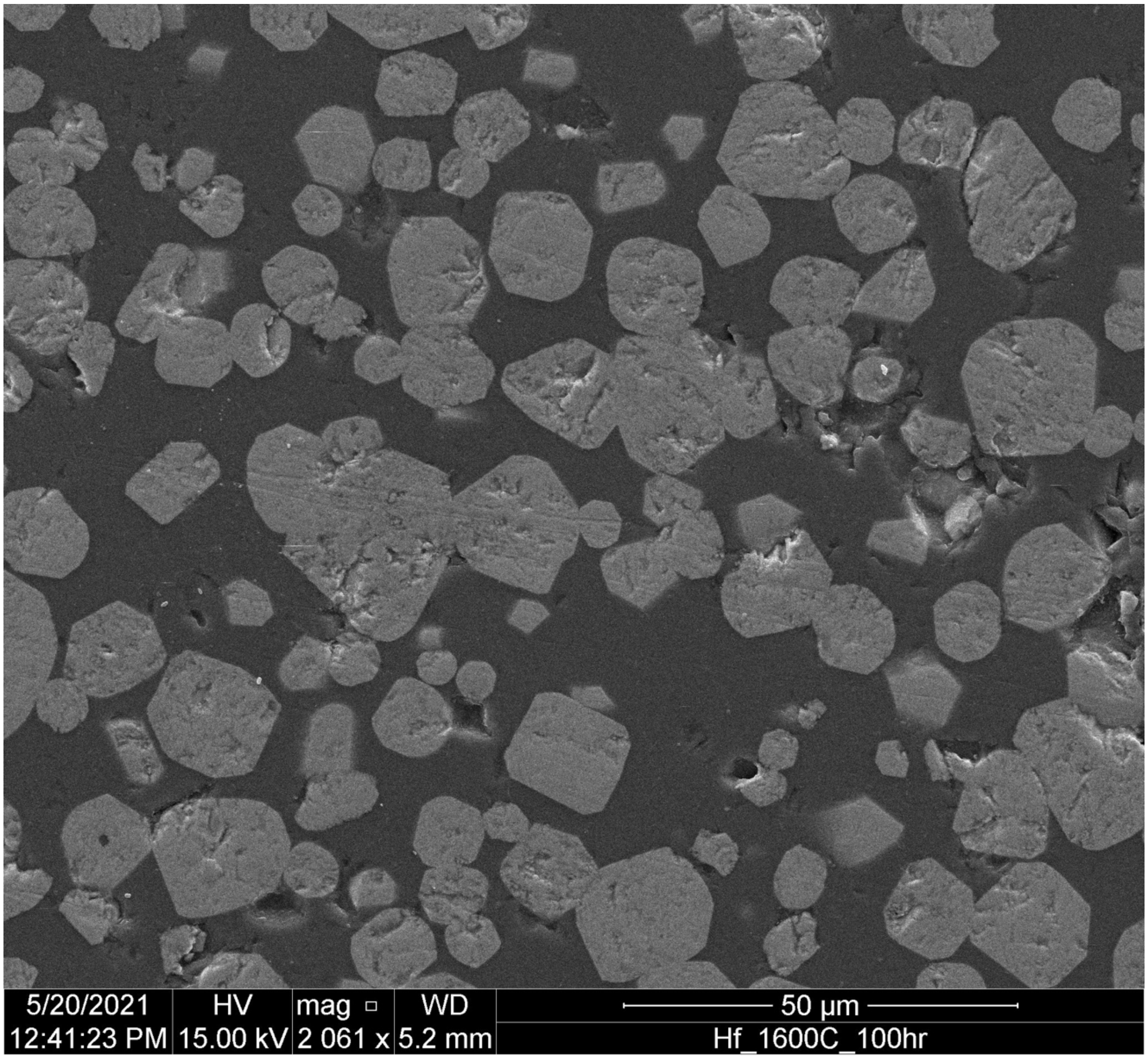

Figure 46. Polished cross section of HfB_2+CMAS 1600°C at 100 hours hold. Varying sizes and sharpness of particles indicate HfO_2 and $HfSiO_4$ are present.

Figure 46 matches with Ahlborg and Zhu [33] results, shown in Figure 47, where HfO_2 are round in shape and varying in size.

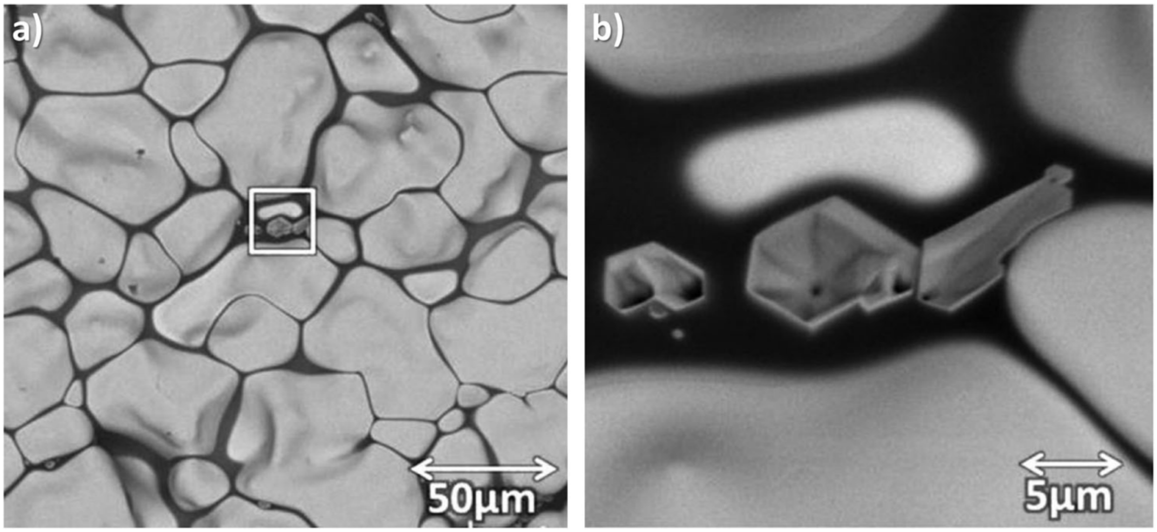

Figure 47. (A) RE doped HfO_2 with (B) CMAS infiltration. Note the similarities in shape and size of HfO_2 with Figure 46. Source: [33]

The sample was prepped and placed under TEM for to perform EDX. The image of the sample is shown in Figure 48 and Figure 49. The sample appeared to be crystalline in nature and surrounded by an amorphous phase. The d-spacing of the crystal, shown in Figure 50 and Figure 51, was measured to be 2.69 angstrom correlating to (211) plane of $HfSiO_4$ conveying the silicon rich CMAS is the direct cause for the formation of $HfSiO_4$.

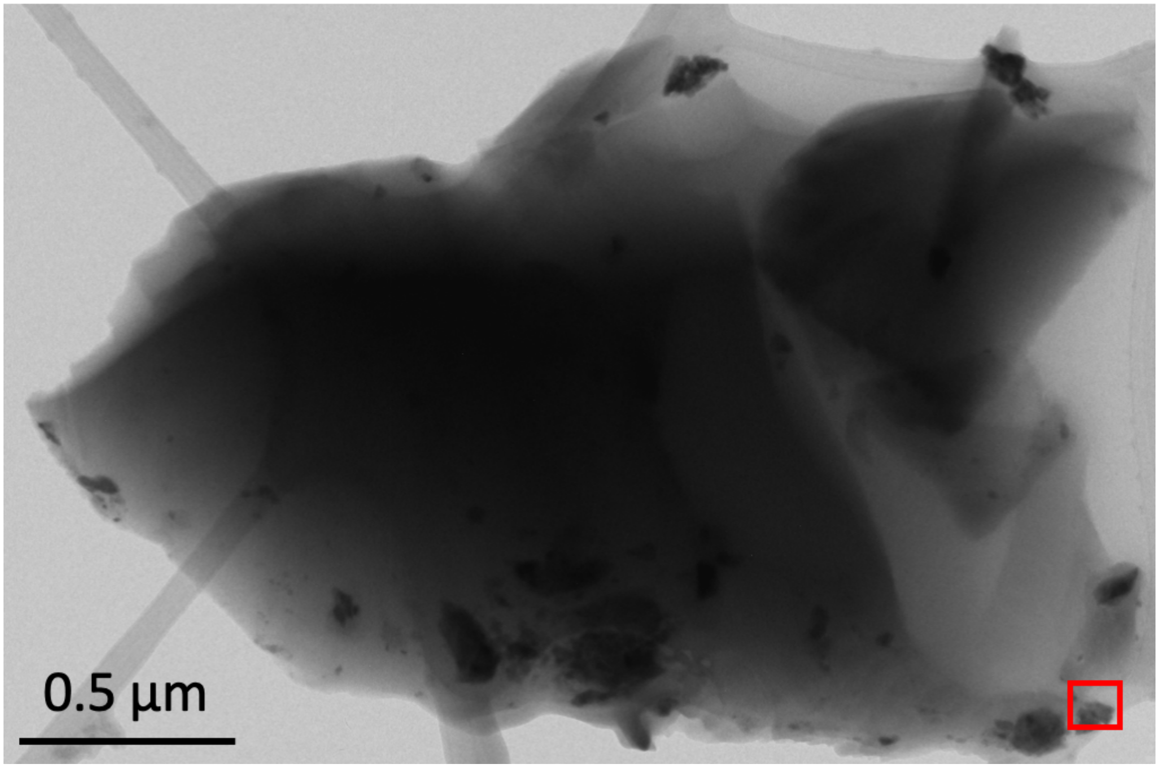

Figure 48. TEM image of HfB_2+CMAS exposed at 1600°C for 100 hours. The red box is shown in Figure 49.

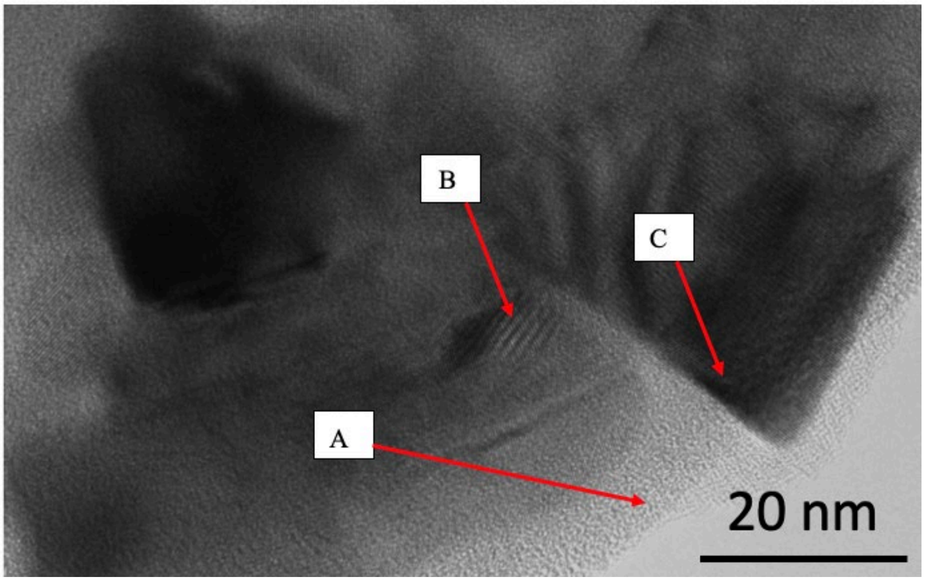

Figure 49. TEM image of HfB2+CMAS exposed at 1600°C for 100 hours at 20 nm. (A) Amorphous phase species. (B) Crystalline phase. (C) Area where measurement of d-spacing shown in Figure 50 was taken from.

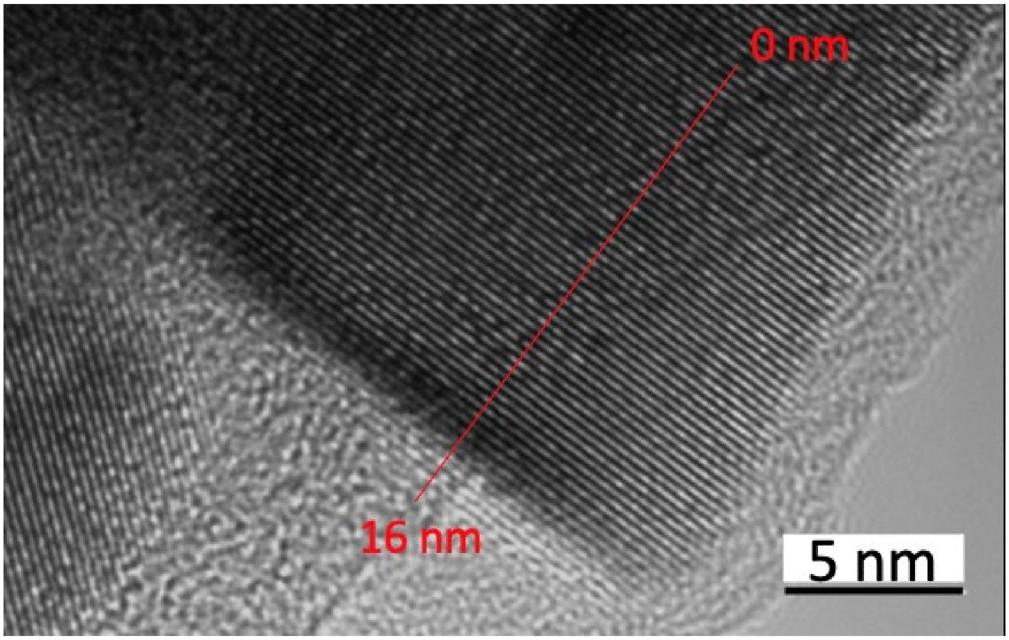

Figure 50. The spacing between the plane, shown in Figure 51(B), measured 2.69 angstroms.

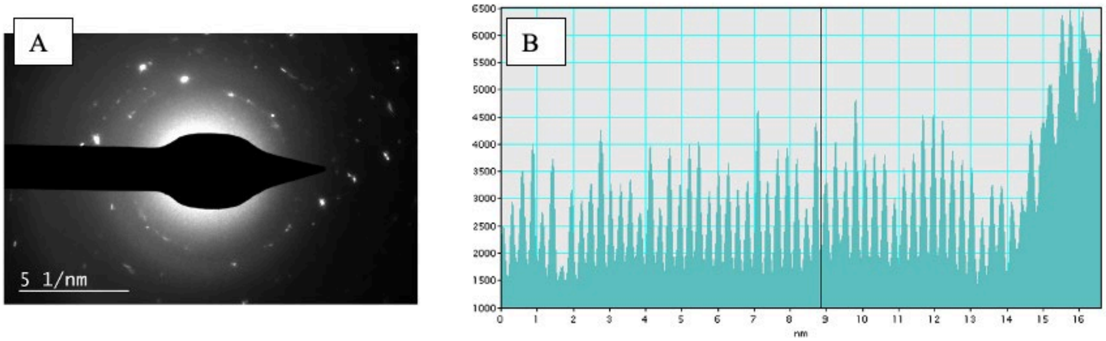

Figure 51. (A)Electron diffraction pattern of the sample. The strong halo presence suggest the species is surrounded by an amorphous phase. (B) The line profile of the sample from 0–16 nm.

An EDX was conducted in a small area shown in Figure 52. The results, shown in Figure 53, reveal the sample is made up Hf, Si, and O indicating the sample is $HfSiO_4$. The presence of boron is unlikely due to low energy of boron and limitations of the TEM accurately detecting boron. The presence of silicon along with other CMAS constituents indicate the crystal is surrounded by CMAS glass with potentially boron diffuse in the glass indicating B_2O_3(high unlikely at this temperature range) in still present in the sample at 1600°C.

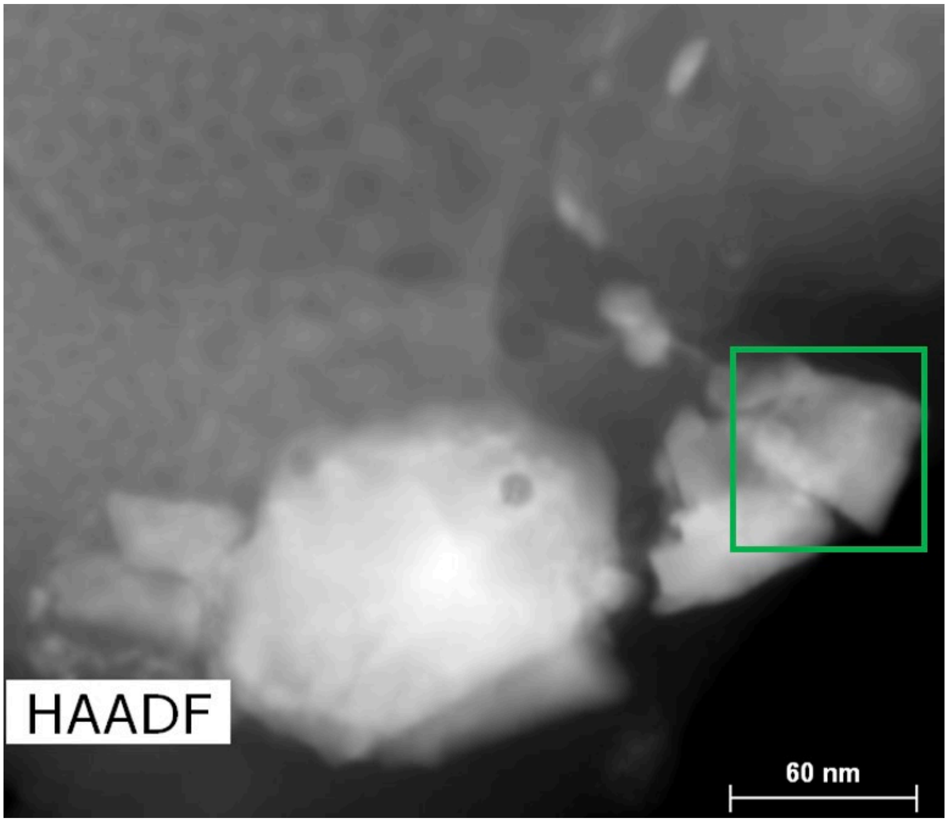

Figure 52. The green box is the area where Figure 50 and Figure 51 was conducted and the EDX mapping entire image shown in Figure 53.

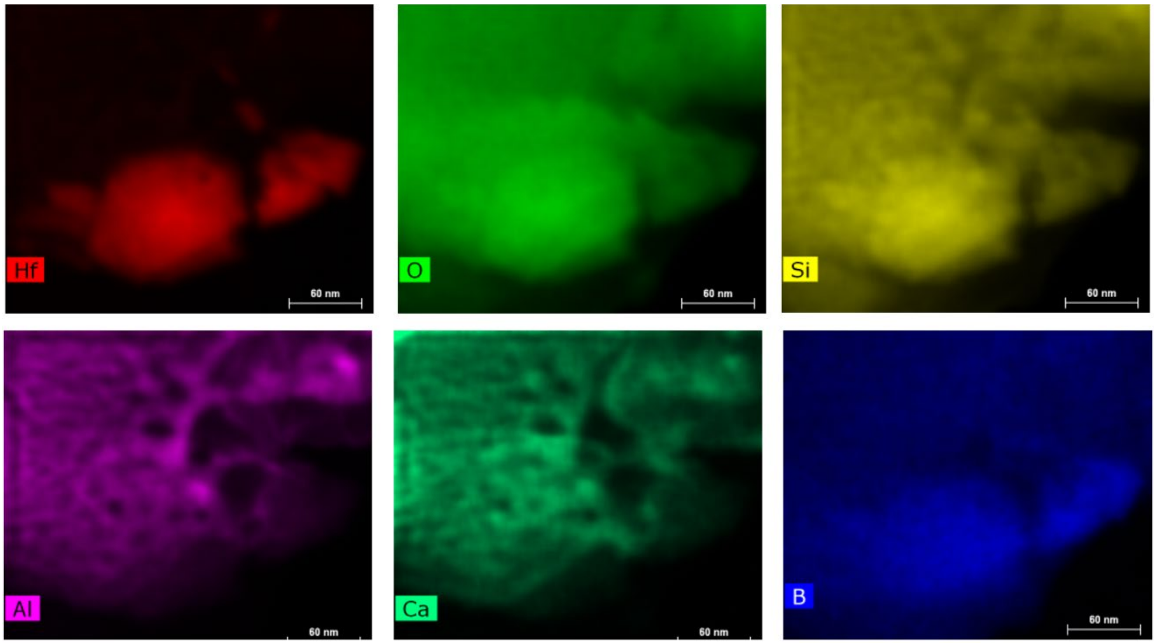

Figure 53. EDX mapping of the sample. $HfSiO_4$ is surround by CMAS and potentially B_2O_3 glass(low confidence).

4. Comparison Across Temperature and Time

In all three runs, HfB_2 reacted with the oxygen in the air to produce monoclinic phase of HfO_2. As temperature and duration increase, the oxidation also increases yielding stronger peaks of HfO_2 with nearly all of HfB_2 gone and this trend can be clearly seen in Figure 54, Figure 55, and Figure 56. For all temperatures with 10/100 hours durations, the CMAS reacted with HfO_2 and produced tetragonal phase of $HfSiO_4$. The strongest intensity of $HfSiO_4$ came from the 1300°C 100 hour run and is seen in Figure 56. The 1600°C 100 hours sample did not yield strongest peaks for $HfSiO_4$ but did for the 10-hour run. The trend can be seen in Figure 57.

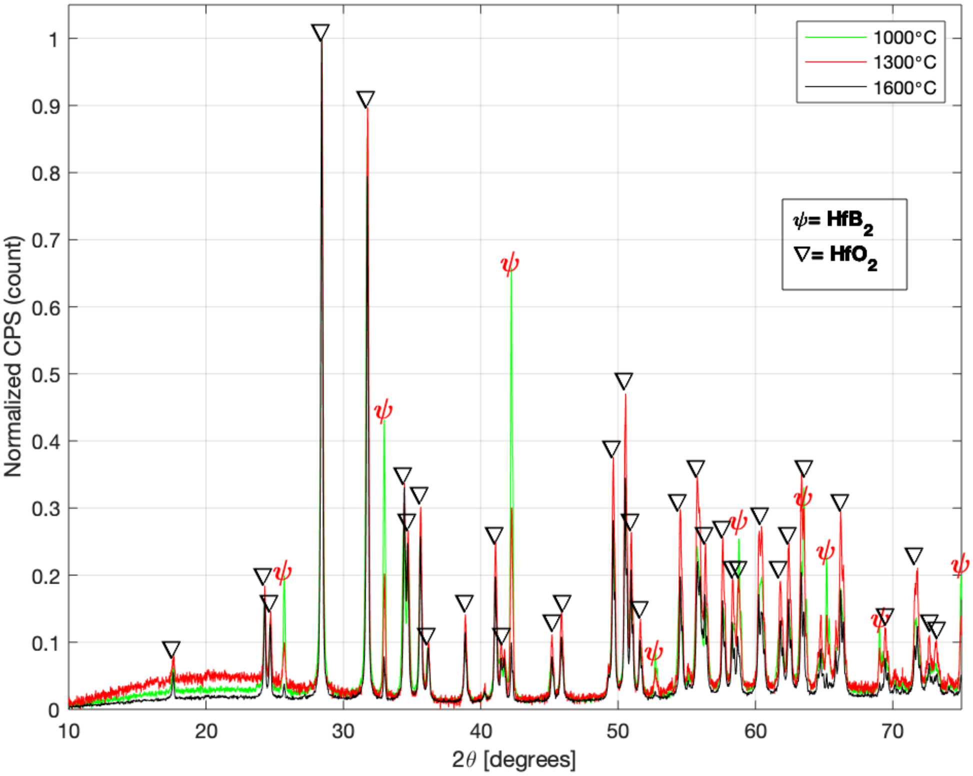

Figure 54. One hour isothermal hold at 1000°C, 1300°C, and 1600°C for HfB_2. The plots show despite temperature increase, HfO_2 does not interact with CMAS. Additionally, HfB_2 oxidized at a faster rate as temperature increases.

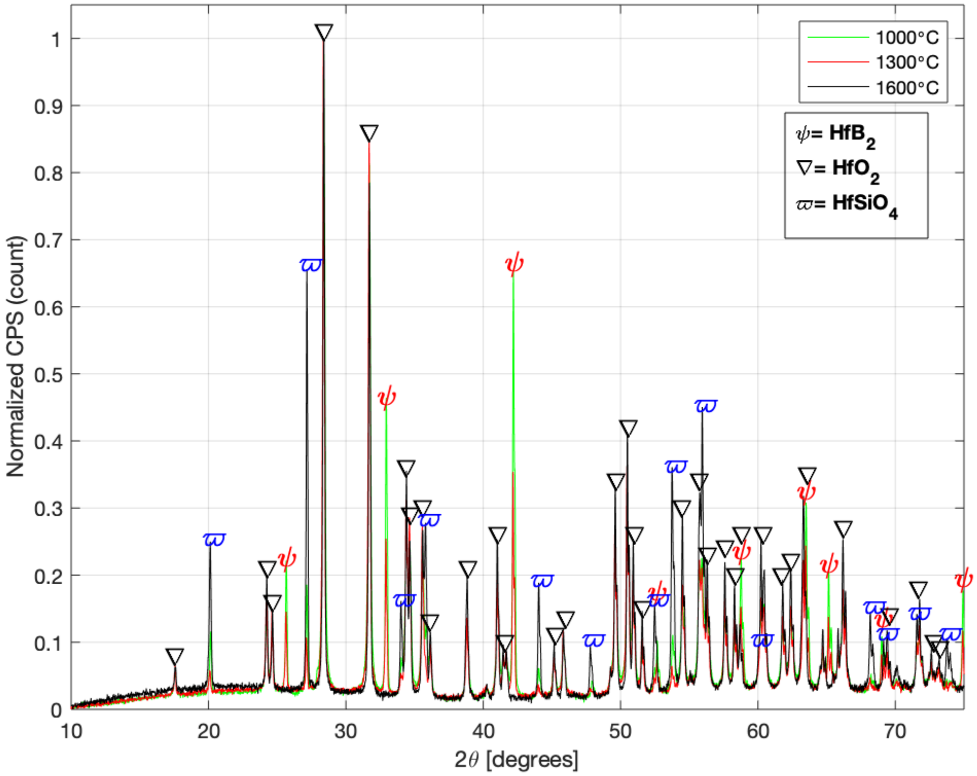

Figure 55. Ten-hour isothermal hold at 1000°C, 1300°C, and 1600°C for HfB_2. At 1600°C, both HfO_2 and $HfSiO_4$ produce the strongest intensities with nearly all of HfB_2 gone.

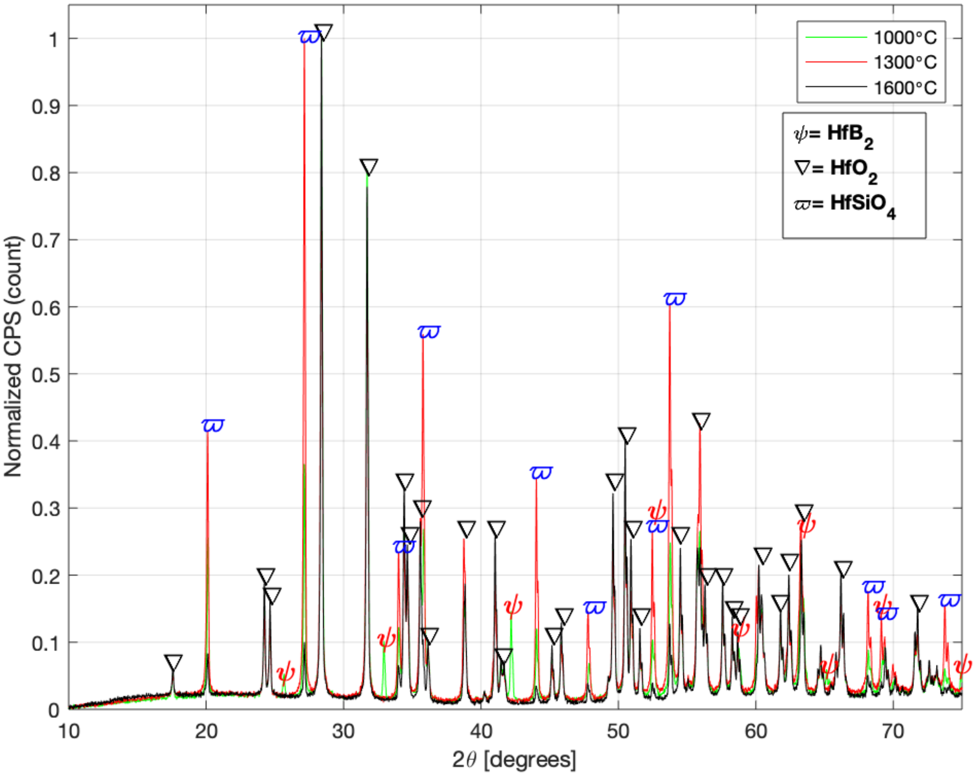

Figure 56. 100 hours isothermal hold at 1000°C, 1300°C, and 1600°C for HfB_2. At 1300°C, $HfSiO_4$ produces the strongest intensity indicating the reaction with CMAS is the strongest.

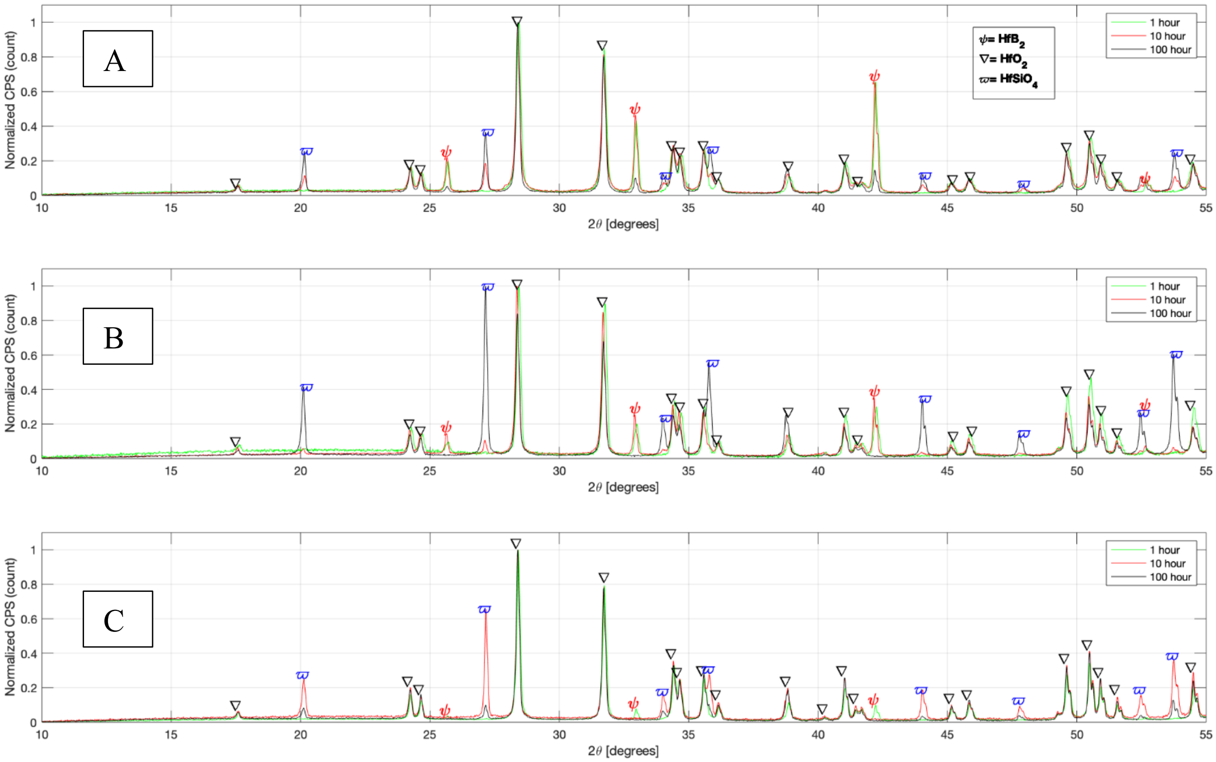

Figure 57. With the exception of all one hour runs and 1600°C 100 hours hold, all plots show HfB_2 oxidizes into HfO_2, and HfO_2 reacts with CMAS to yield $HfSiO_4$(A) 1000°C isothermal at 1,10,100 hours. (B) 1300°C isothermal at 1,10,100 hours. (C) 1600°C isothermal at 1,10,100 hours.

A study conducted by Salt et al. [31] suggested at the higher temperatures of hafnon ($HfSiO_4$) may have dissociated and reverted to HfO_2 and siliceous glass based of study conducted by Curtis et al.[32] where zircon ($ZrSiO_4$) dissociated into ZrO_2 and glass. This would account for the lower XRD intensity peaks for $HfSiO_4$ seen in 1600°C 100 hours run seen in Figure 44 and Figure 57(C).

E. ZRB2 CMAS INTERACTION

1. 1000°C Isothermal Hold

Figure 58 shows the sample after removed from the furnace. The powder appears to sinter with white crystalline particles and glassy surface visible on the porous puck not observed on any HfB_2 run. XRD analysis of the sample, shown in Figure 57, shows a monoclinic phase of ZrO_2, a result of oxidation. All major peaks correlates to ZrB_2 with a weaker peak correlating to ZrO_2 suggest ZrB_2 did not oxidized as quickly as HfB_2.

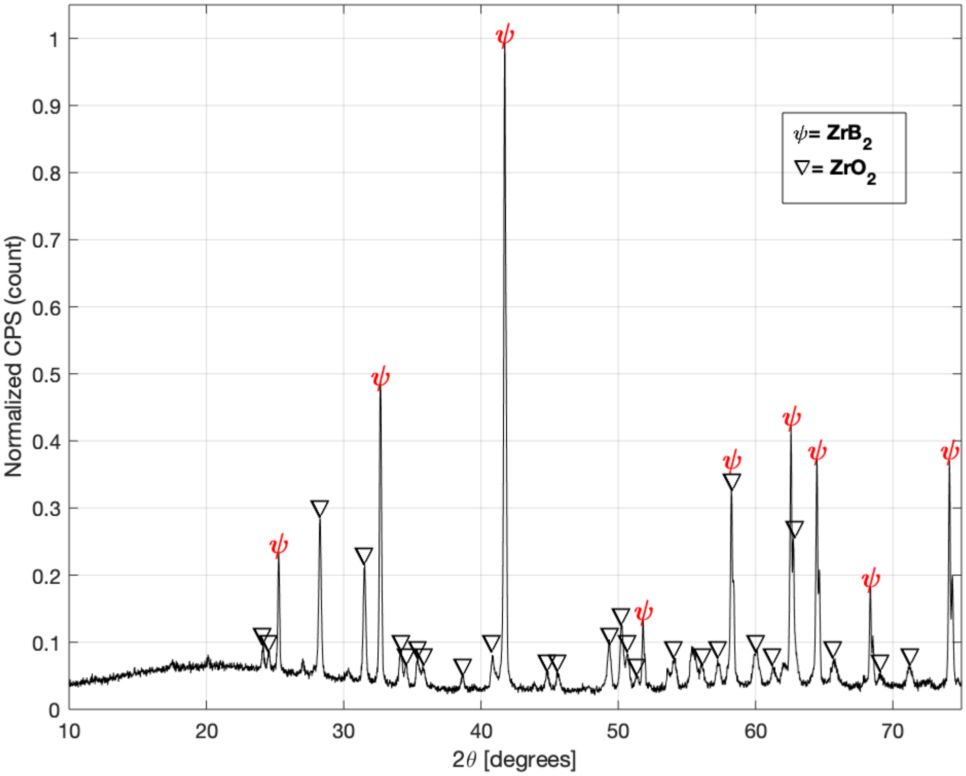

Figure 58. XRD spectra of ZrB_2 +CMAS held at 1000°C for one hour. Like with HfB_2, there is no interaction with CMAS, and the only product is monoclinic phase of ZrO_2 with ZrB_2 still present in the sample and seen in Figure 49.

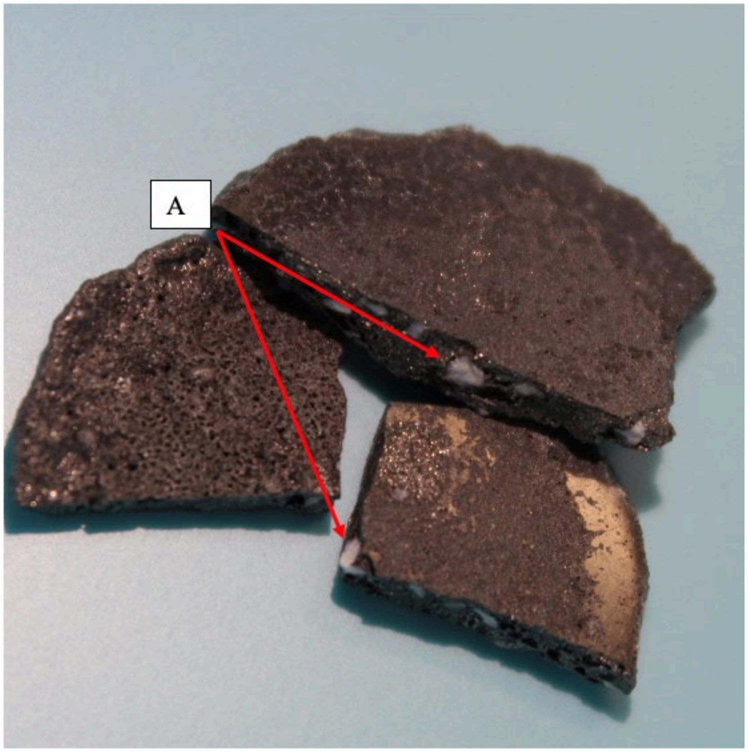

Figure 59. ZrB_2 held at 1000 °C for 1 hour. (A) White crystals appeared in the sample. EDS, shown in Figure 49 and 50, confirms it is CMAS.

The sample, Figure 59, was mounted in resin, polished, and then sputtered for EDS. The results show an even distribution of CMAS, seen in Figure 60 and Figure 61, throughout the material and confirms the white crystal seen in Figure 58 to be CMAS with boron present in the crystal. Figure 60 and Figure 62 shows the composition breakdown of the sample. The analysis did find any ZrO_2 in the sampled area.

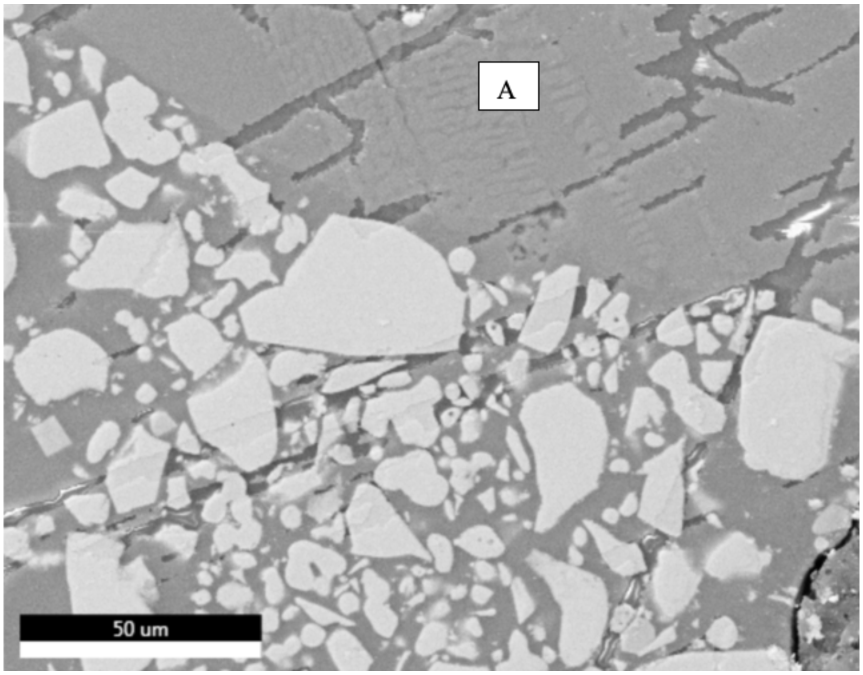

Figure 60. EDS image of ZrB_2 exposed to CMAS at 1000°C for an hour. (A) The gray region correlates to the white crystal seen in Figure 48. Figure 50 shows the crystal is compose of CMAS constituents.

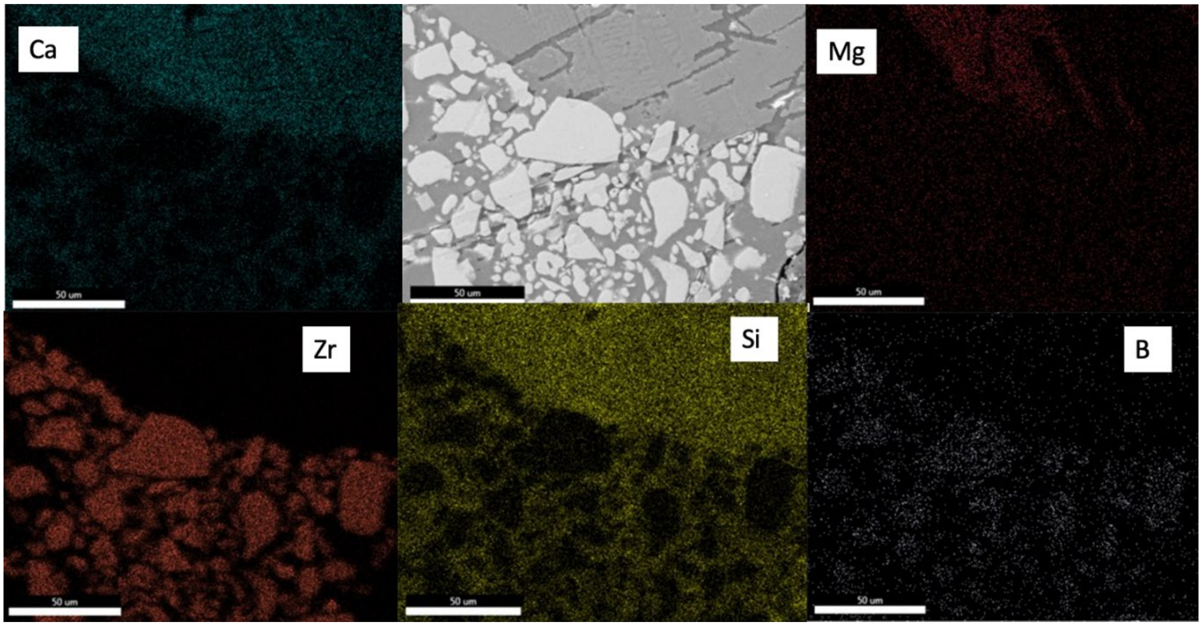

Figure 61. EDS image of ZrB_2 exposed to CMAS at 1000°C for an hour. The sample, taken from inside the puck, did not oxidize and as a result did not react which CMAS. The particles are ZrB_2 surrounded by CMAS and potentilly B_2O_3.

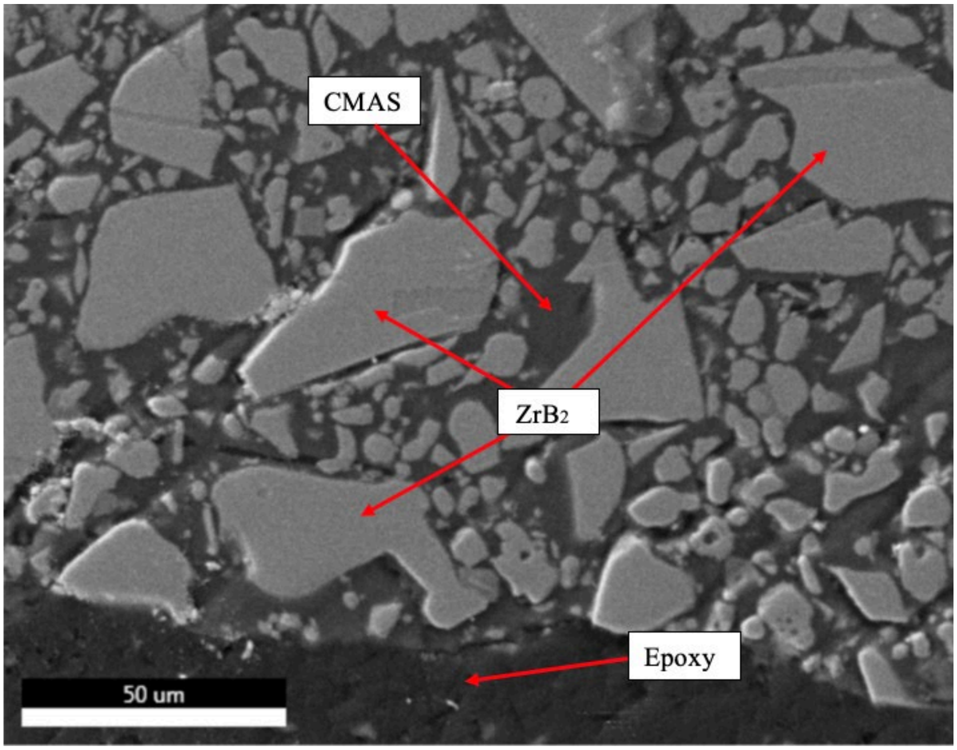

Figure 62. SEM image of ZrB_2 +CMAS taken from the surface of the sample. Figure 62 shows the composition of the sample.

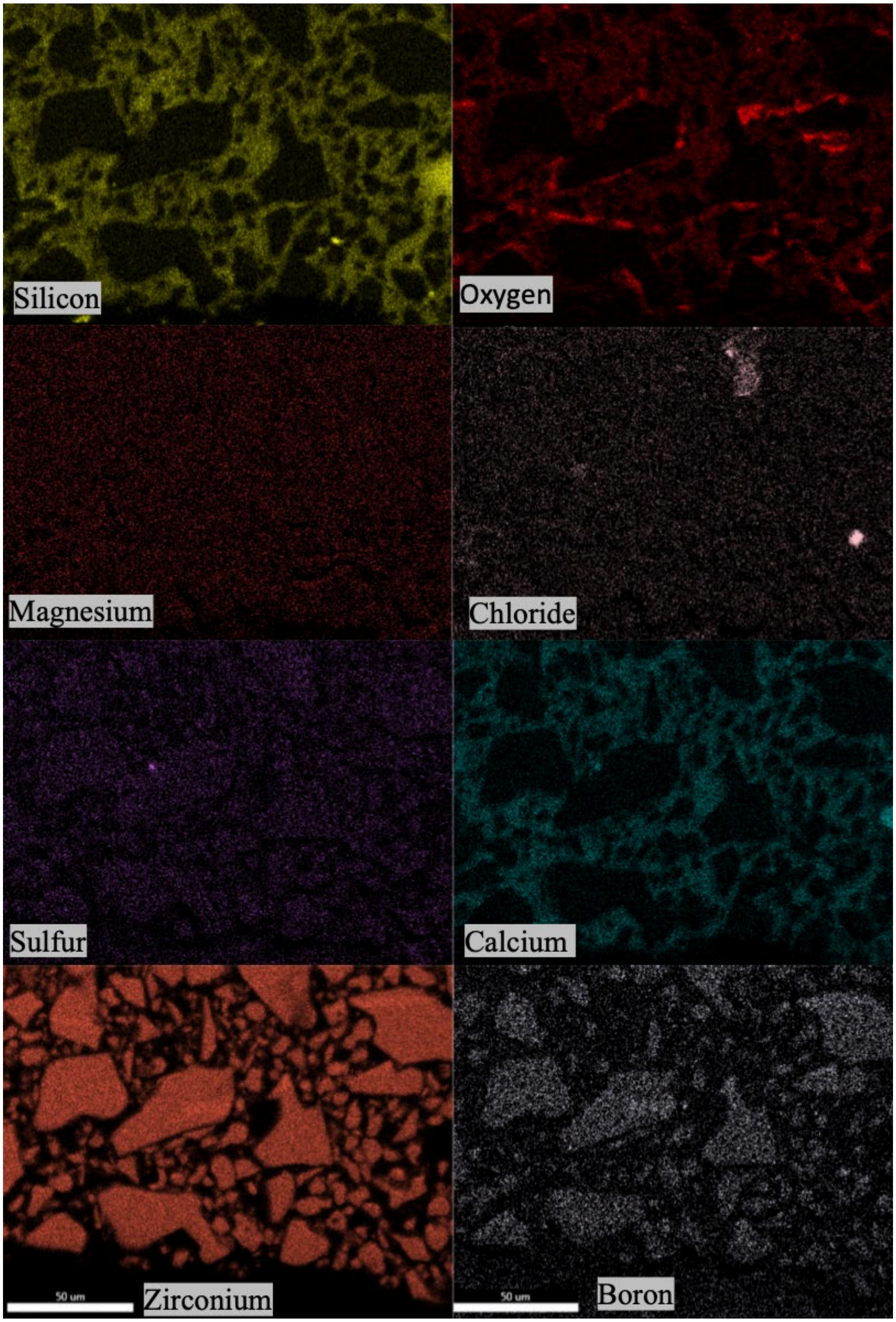

Figure 63. EDS composition of the ZrB_2 +CMAS sample held at 1000°C for an hour. The increased intensities for oxygen correlates to gaps on the surface of the sample.

After the ten-hour run, the sample displayed increased oxidation. Figure 64 shows the resulting powder after the run and shows a difference in color on the surface and inside the puck. A glassy presence was observed at the bottom of the puck as well. XRD analysis, Figure 63, shows a tetragonal phase of $ZrSiO_4$ indicating CMAS reacted with ZrO_2. Majority of the sample is still composed of ZrB_2 based of the strength of intensity peaks shown in Figure 63. During the 100 hours run, the increased oxidation product reacted with CMAS resulting in stronger peaks, shown Figure 65, of $ZrSiO_4$ and weaker peaks for ZrB_2. The sample, Figure 66 , continues to follow the trend observed in previous run where oxidation is observed on the surface and grows inward.

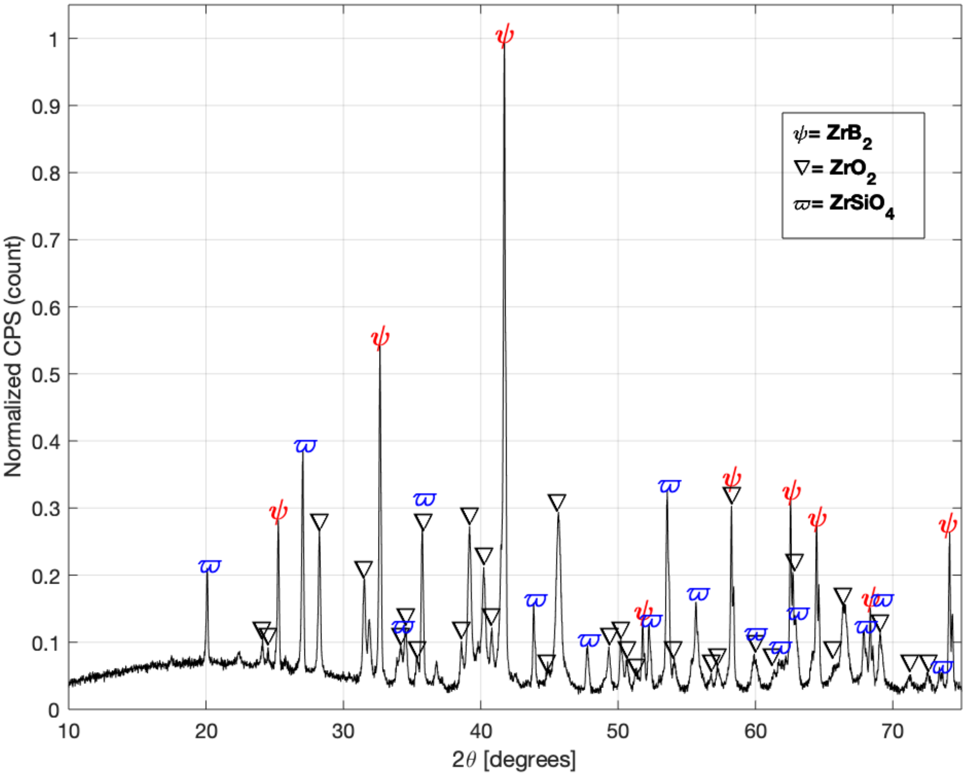

Figure 64. XRD spectra of ZrB_2 +CMAS held at 1000°C for ten hours. Like with HfB_2, the monoclinic phase of ZrO_2 reacted with CMAS to create tetragonal phase of $ZrSiO_4$.

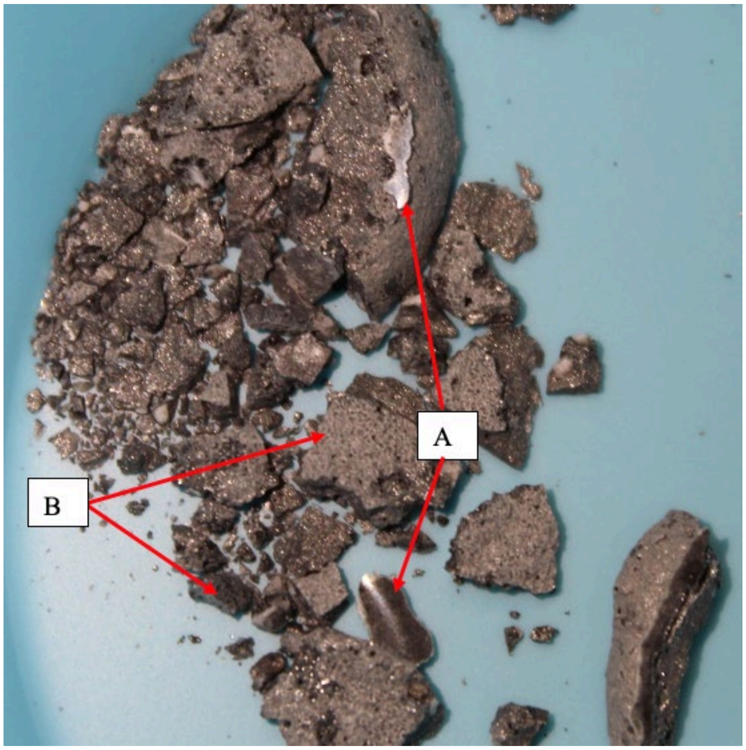

Figure 65. ZrB_2 +CMAS held at 1000 °C for 10 hours. (A) Glassy film observed at the bottom of the sample and is likely silicious glass. (B) Differences in shade indicates oxidation reaction is most prominent at the surface.

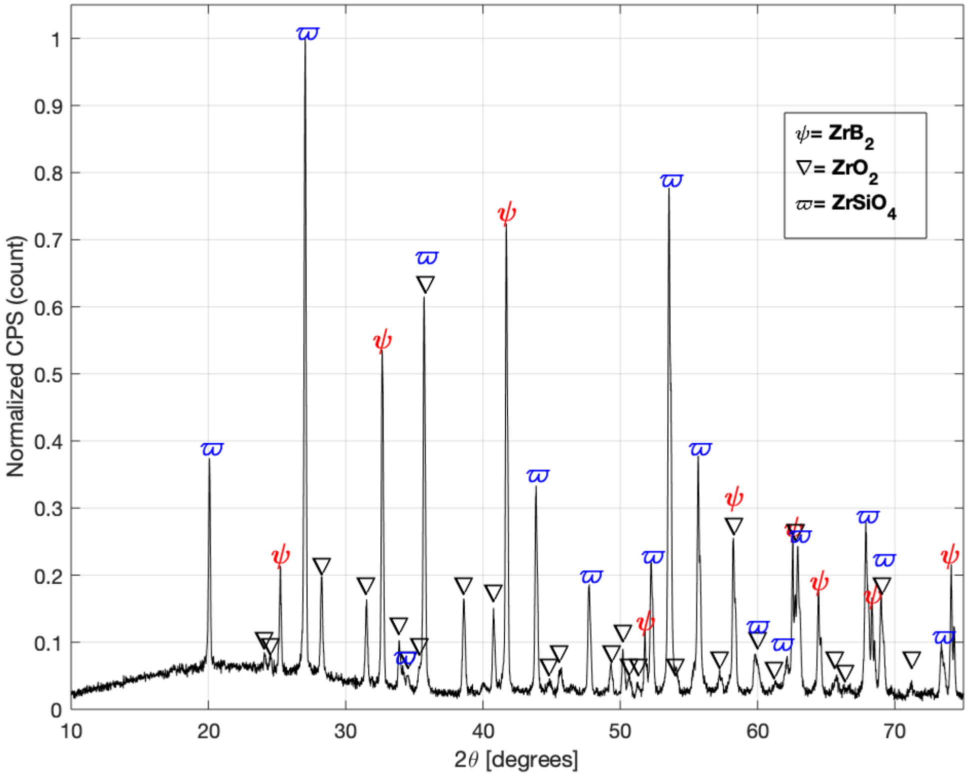

Figure 66. XRD spectra of ZrB_2 +CMAS held at 1000°C for 100 hours. Like with HfB_2, the monoclinic phase of ZrO_2 reacted with CMAS to create strong peaks of tetragonal phase $ZrSiO_4$.

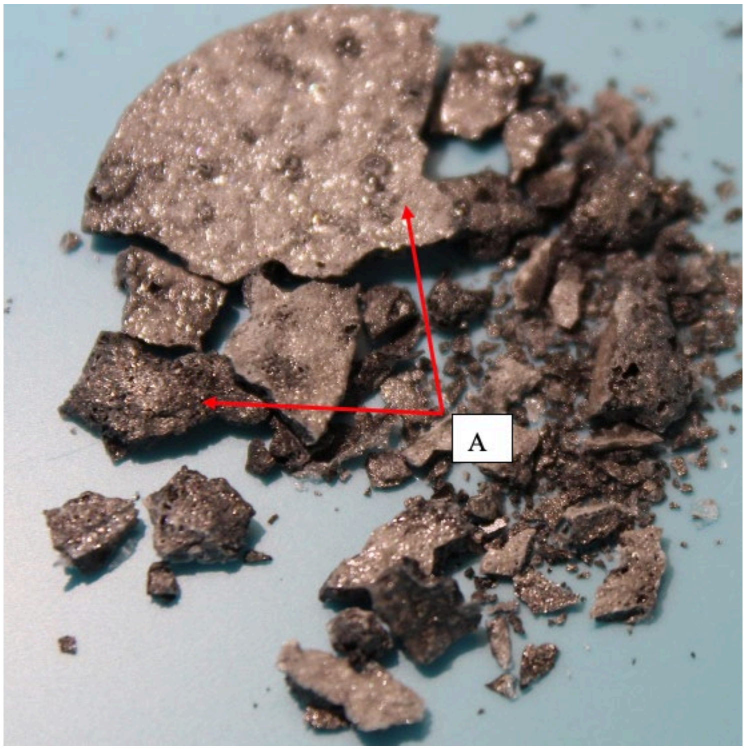

Figure 67. ZrB_2 held at 1000°C for 100 hours (A) Difference in shade shows oxidation is prominent on the surface of the sample.

2. 1300°C Isothermal Hold

ZrB_2 followed the same trend observed in HfB_2 when heated to 1300°C. Oxidation continues to increase with time and is seen physically in Figure 68, Figure 70, and Figure 74. At 100 hours, the reaction become more volatile as porous holes are observed in Figure 74 in the sample as B_2O_3 transitions into a gas.

Unlike in the 1000°C one-hour XRD spectra of ZrB_2 and all HfB_2 one hour runs, the 1300°C one-hour XRD spectra of ZrB_2, Figure 67, displayed small peaks correlating to traces of $ZrSiO_4$, a sign of reaction between zirconia and the CMAS glass.

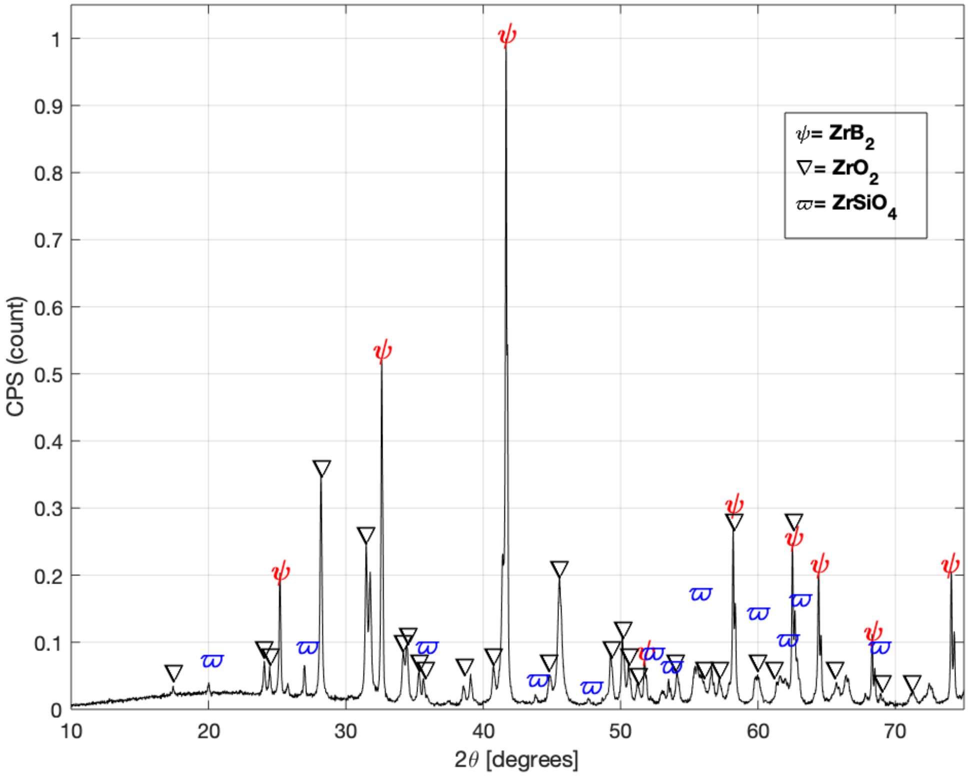

Figure 68. XRD spectra of ZrB_2 +CMAS held at 1300°C for one hour. Unlike with previous one hour runs, the monoclinic phase of ZrO_2 reacted with CMAS to form $ZrSiO_4$.

Figure 69. ZrB_2 held at 1300 °C for 1 hour. A Glassy film and an oxidation layer are observed on the sample.

For the 10-hour run, increased oxidation resulted in an increased reaction with CMAS yielding more $ZrSiO_4$, shown in the XRD spectra in Figure 69, but did not result in ZrB_2 completely reacting as physically seen in Figure 70. A sample between both surface and inside boundary was cut off, mounted in resin, and then polished to observe under SEM shown in Figure 71. The particles inside the boundary are sharper and more faceted in shape (correlating to unreacted ZrB_2 and CMAS) compared to the surface where the particles are round in shape (correlating to ZrO_2) and matches with Ahlborg and Zhu [33], shown in Figure 72.

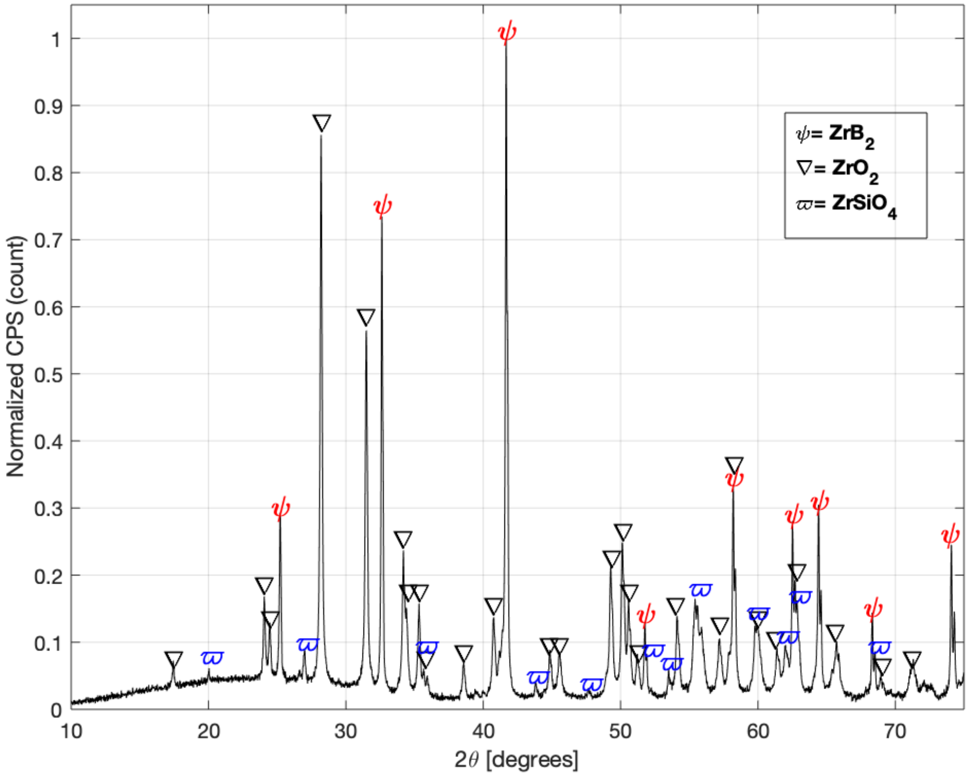

Figure 70. XRD spectra of ZrB_2 +CMAS held at 1300°C for ten hours. Like with HfB_2, the monoclinic phase of ZrO_2 reacted with CMAS to create $ZrSiO_4$.

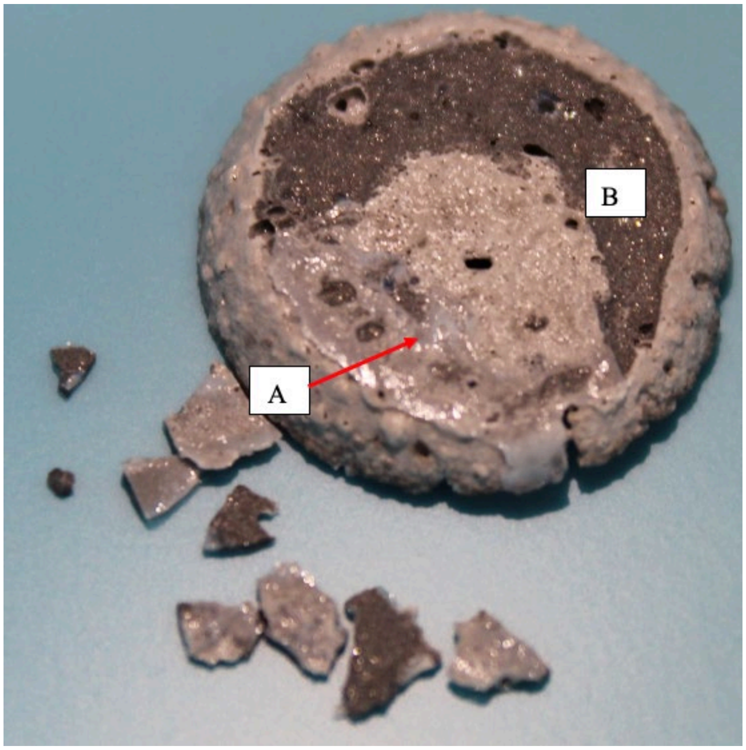

Figure 71. ZrB_2 held at 1300 °C for 10 hours. (A)Glassy film is observed. (B) The difference in color shows the oxidation on the surface and the unreacted ZrB_2 inside the puck.

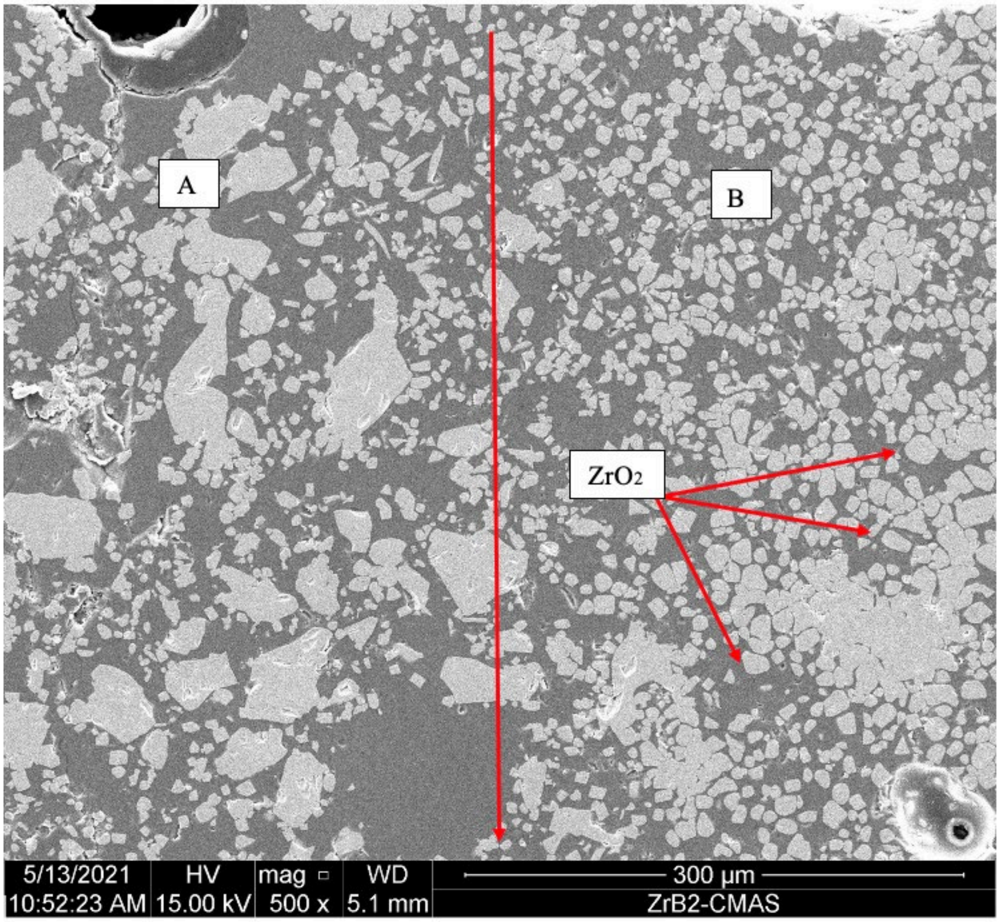

Figure 72. Distinct difference in sizes can be seen in ZrB_2 held at 1300 °C for 10 hours in region (A) and (B). The red arrow roughly divides the boundary. Region A shows unreacted ZrB_2 and CMAS given by the faceted hexagonal shape and Region B shows reacted ZrB_2 with O resulting in ZrO_2which are larger in diameter and circular in nature as seen in Ahlborg and Zhu [33] experiment shown in Figure 72.

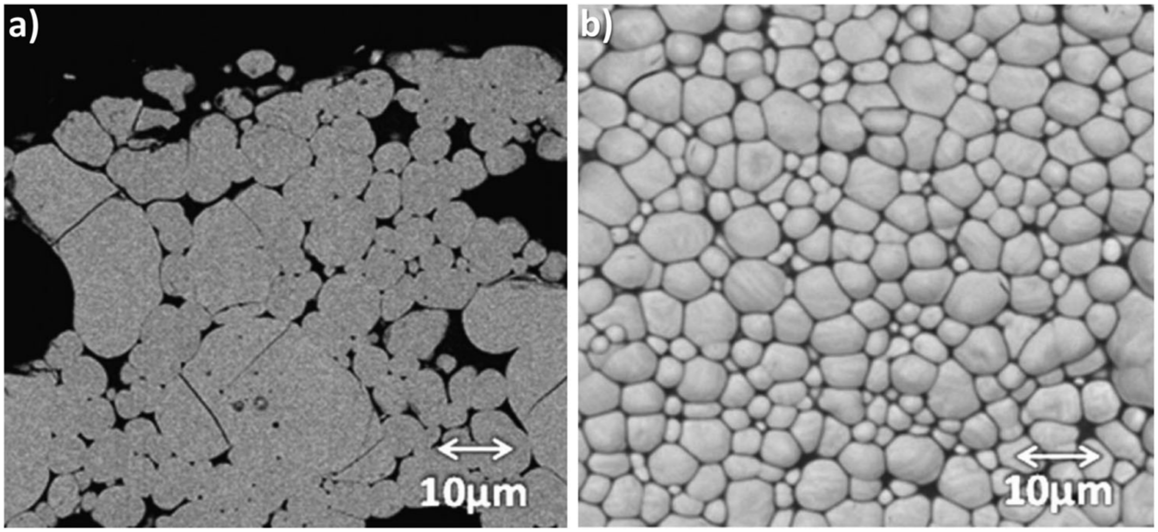

Figure 73. Re doped ZrO_2 exposed to CMAS. Note the similarity in size and shape of ZrO_2 as seen in Figure 71. Source: [33]

The 100 hours run sample experienced a more volatile reaction with oxygen and CMAS. Porous holes were observed, seen in Figure 75, indicating B_2O_3 formed into a gas and escape from the sample. XRD spectra, shown in Figure 74, reveal the strongest peaks of that of $ZrSiO_4$ all out of the trials conducted during the experiments with nearly all of ZrB_2 completely gone. SEM images, shown in Figure 76, shows tetragonal $ZrSiO_4$ with ZrO_2 inside the crystal from the 1300 °C 100 hour sample.

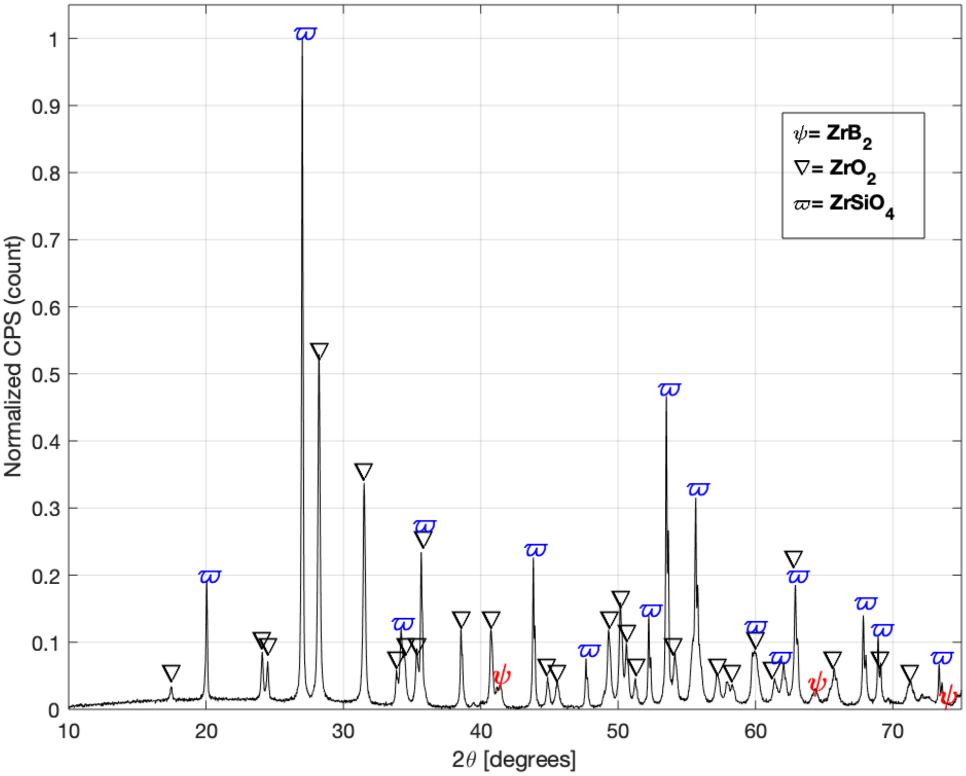

Figure 74. XRD spectra of ZrB_2 +CMAS held at 1300°C for hundred hours. ZrB_2 is almost gone oxidating into ZrO_2 and then into $ZrSiO_4$.

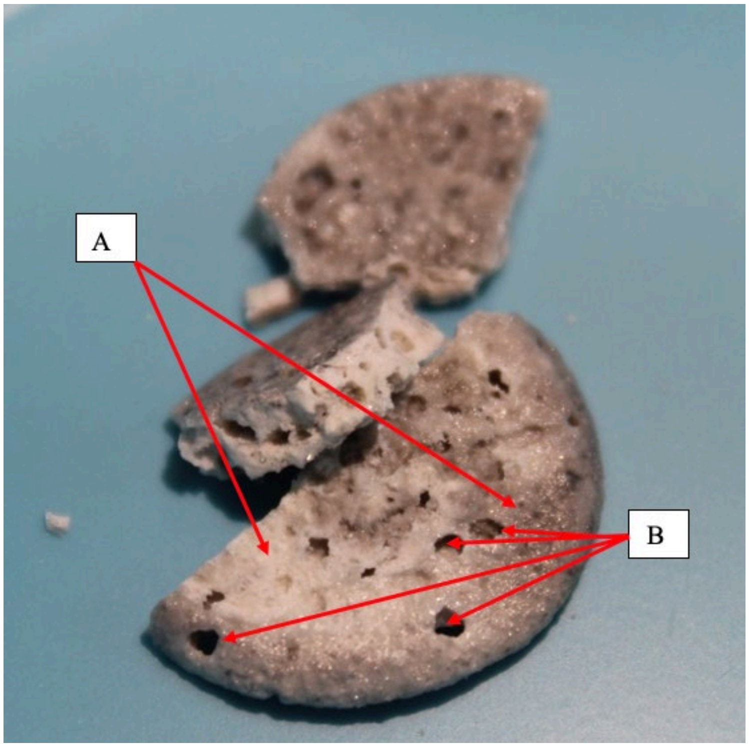

Figure 75. ZrB_2 held at 1300°C for 100 hours. (A) The sample shows nearly all of ZrB_2 reacted to form ZrO_2. (B) The porous holes correlate to the B_2O_3 escaping from the sample as it evaporates.

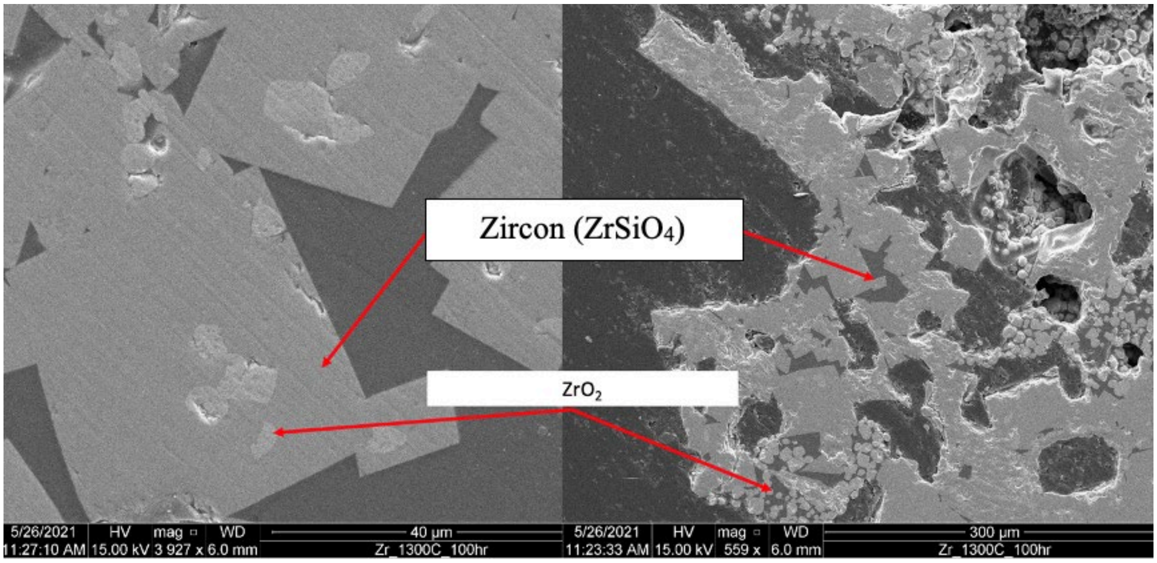

Figure 76. Like with $HfSiO_4$, $ZrSiO_4$ displayed the same shape with ZrO_2 observed inside the crystal.

3. 1600°C Isothermal Hold

For the final three runs, the temperature was increased to 1600°C using the same ramp up and cool down process from the previous runs. The increase of temperature increased oxidation volatility and led to partial reactivity of all three platinum crucibles. The one hour run sample was almost completely oxidized. Slight shades of grays were observed, shown in Figure 78, indicating small amounts of ZrB_2 was still present in the sample. No glassy film was observed as observed in previous runs. XRD analysis, Figure 77, shows that there was no $ZrSiO_4$ and only small traces of ZrB_2 remained where the majority of the sample had completely oxidized into ZrO_2.

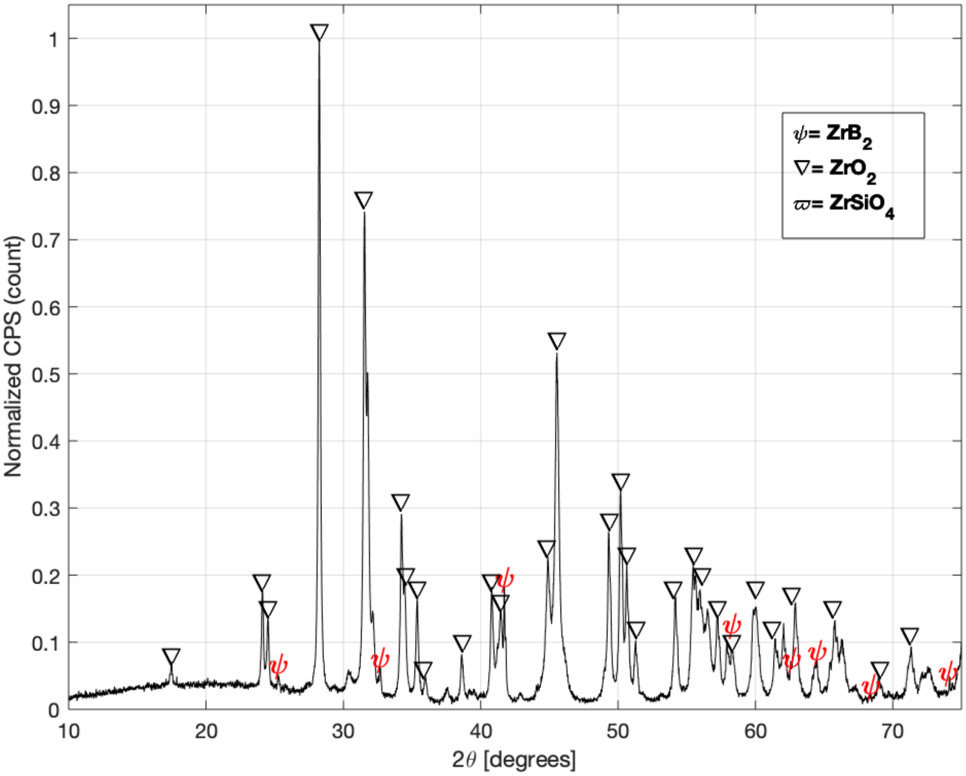

Figure 77. XRD spectra of ZrB_2+CMAS held at 1600°C for one hour. The run shows nearly all of ZrB_2 has oxidized into ZrO_2.

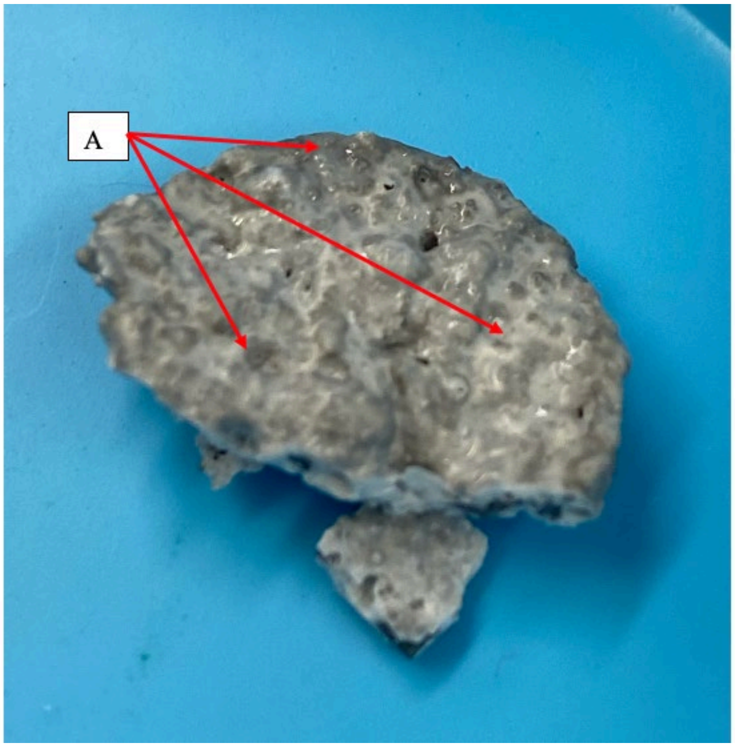

Figure 78. The sample after the one-hour exposure. Darker shades of gray likely indicates a ZrB_2 rich sample.

The remaining two runs followed the same trend as the one hour run. No trace of ZrB_2 or $ZrSiO_4$ was detected in the XRD analysis, shown in Figure 79 and Figure 81, and the oxidation was volatile as the sample became porous as the B_2O_3 evaporated (observed in Figure 80 and Figure 82). A small amount of platinum was observed in the samples, Figure 80, and no glassy films were observed. No new phases were created indicating ZrO_2 did not react with CMAS as with previous at 1000°C and 1300°C.

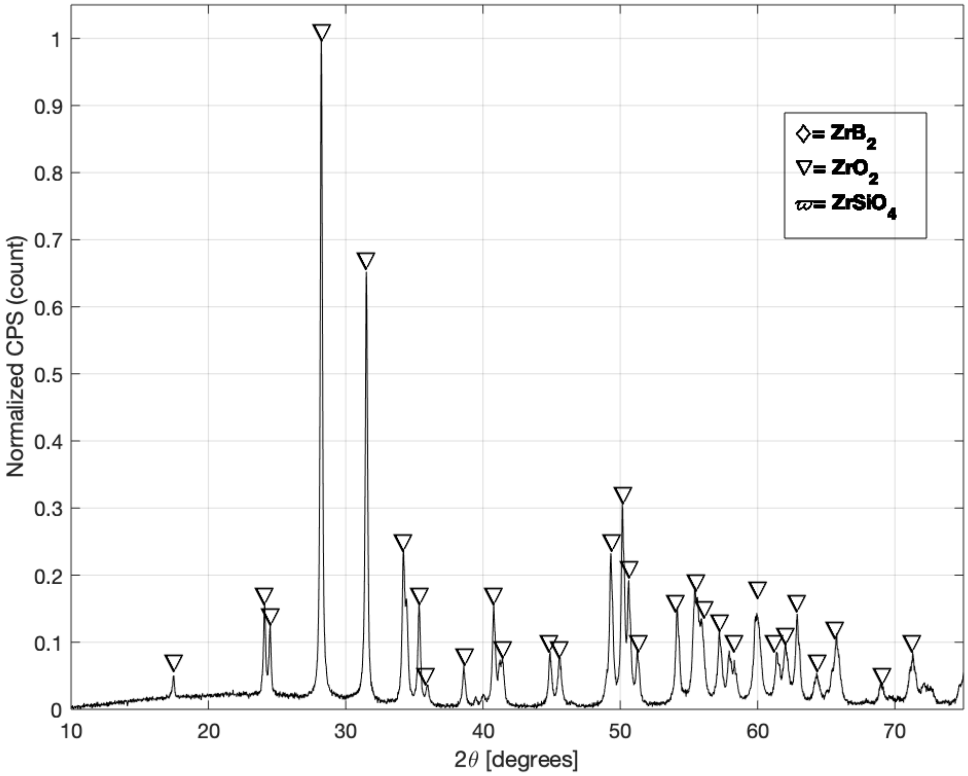

Figure 79. XRD spectra of ZrB_2+CMAS held at 1600°C for ten hours. No traces of ZrB_2 were detected and ZrO_2 did not react with CMAS to form $ZrSiO_4$.

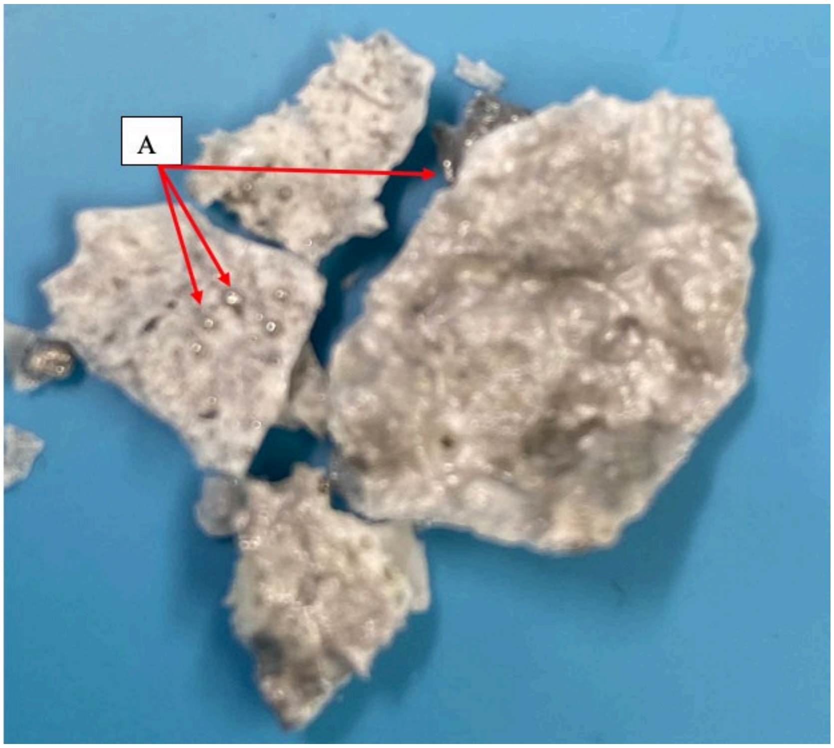

Figure 80. (A) Pieces of platinum from the crucible inside the ten-hour exposed sample.

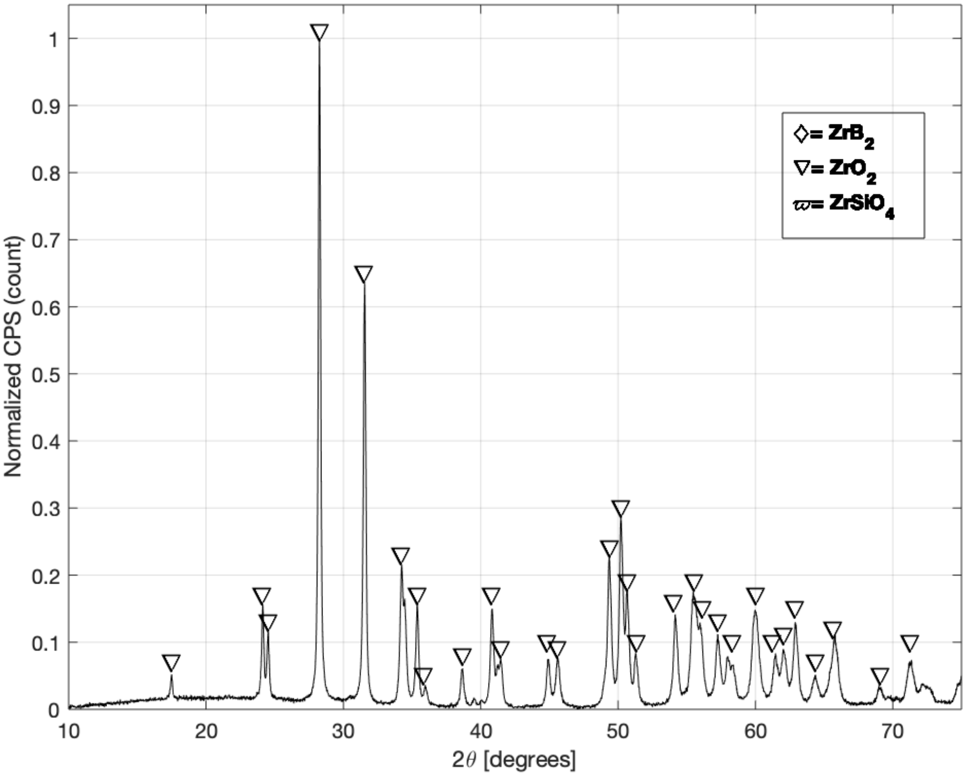

Figure 81. XRD spectra of ZrB2+CMAS held at 1600°C for hundred hours. Like with the ten-hour run, no traces of ZrB_2 and $ZrSiO_4$

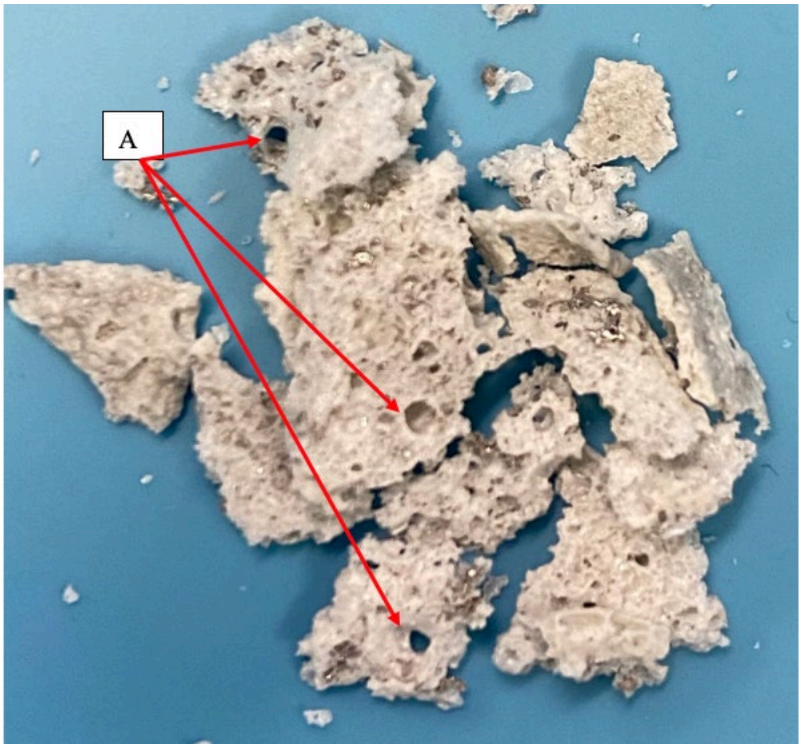

Figure 82. (A) The porous holes observed indicates B_2O_3 evaporated from the sample.

A small piece of the 100 hours sample was mounted in resin and polished to be observed in the SEM. Densely packed, small circular particles were observed through the sample, shown in Figure 83 and Figure 84, with no distinctly shaped particles indicating $ZrSiO_4$ were present.

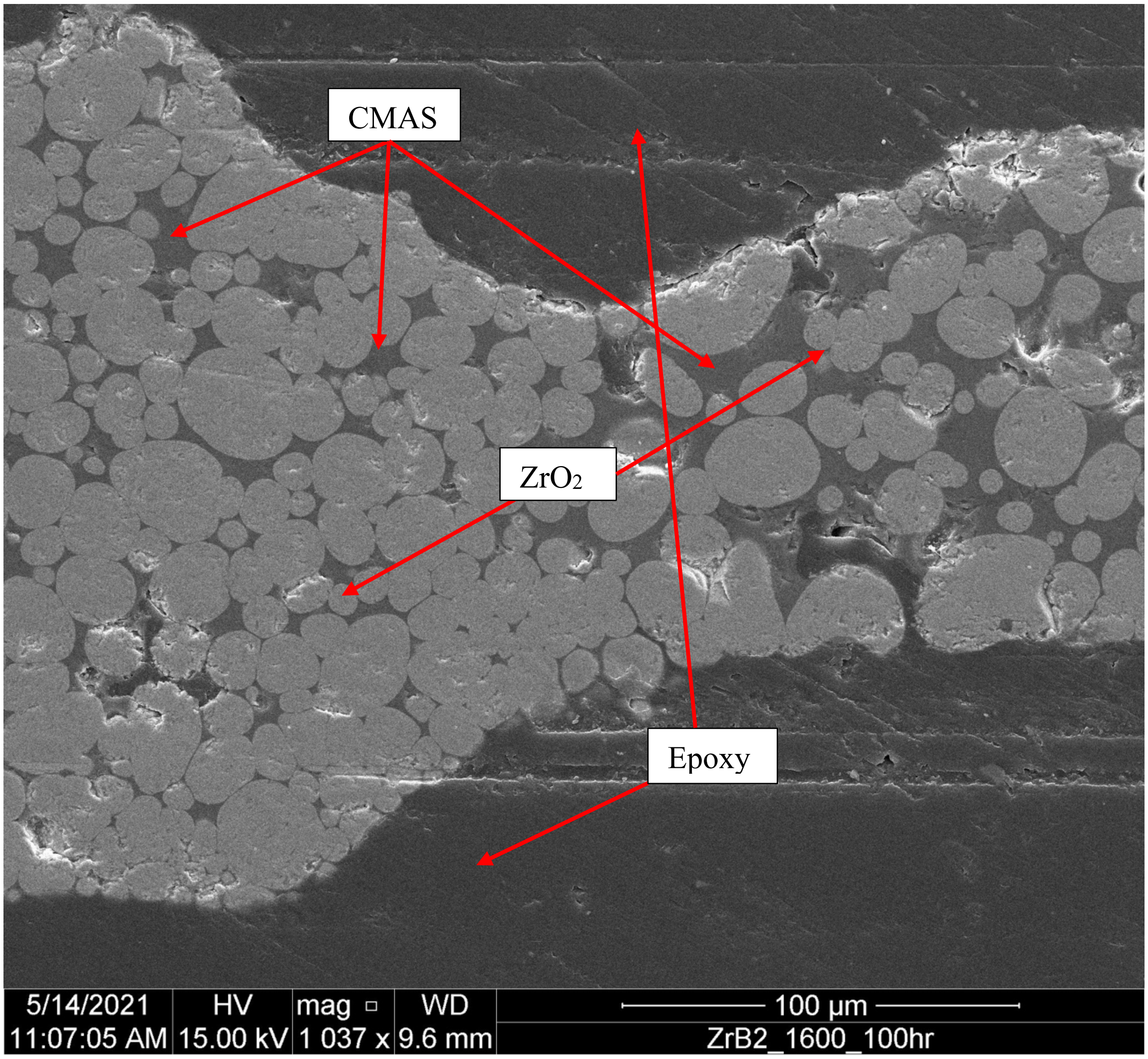

Figure 83. Cross section of densely packed ZrO_2. All of the ZrB_2 oxidized and no other CMAS constituents were observed in the sample.

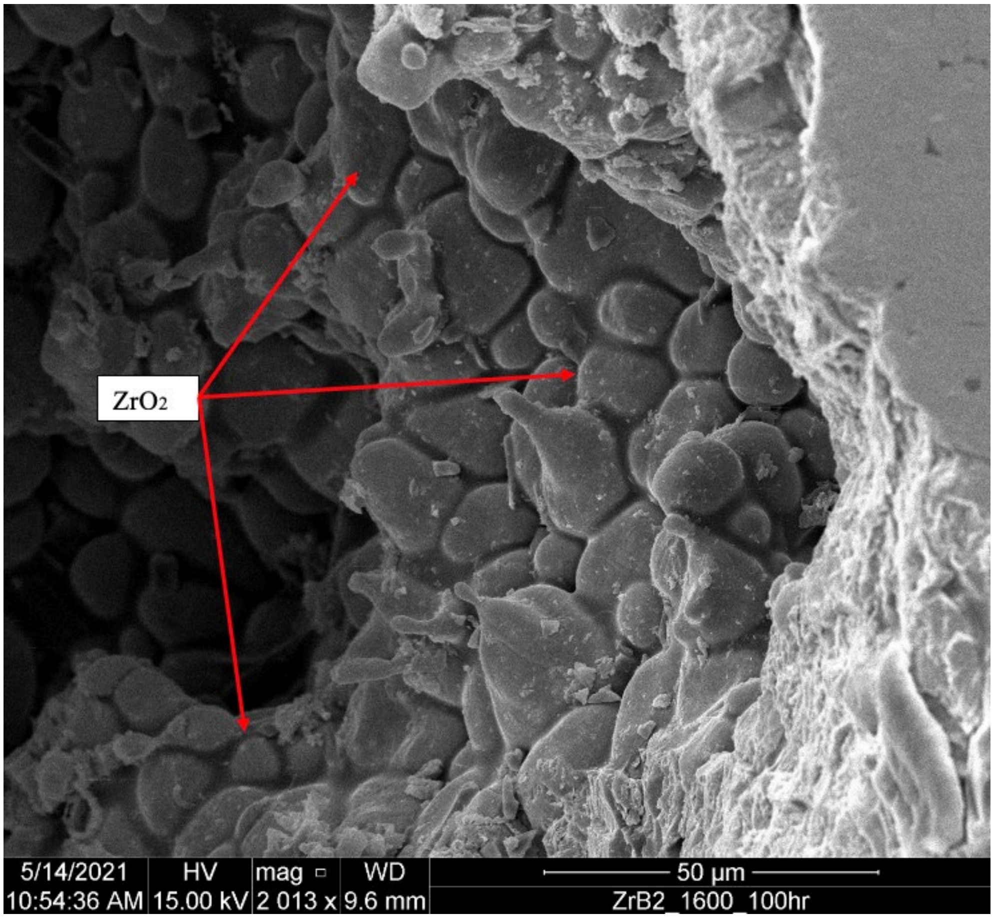

Figure 84. SEM image of ZrO_2 particles.

Next, another sample size was prepped and place under TEM to conduct EDX. The analysis of the sample, shown in Figure 85, revealed that crystalline particles with CMAS constituents, shown in Figure 86, were present in the sample. Similar to the Hf sample, the presence of silicon and boron in throughout of the sample indicate some form B_2O_3 is present in the sample. The traces of aluminum indicate crystal phase of CMAS former are still found in the glassy mixture of CMAS and boron. Electron diffraction of the crystalline surrounded by an amorphous phase, shown in Figure 87, was taken and the d-spacing of two planes, shown in Figure 88, were calculated and found to be 3.16 and 1.30 angstroms correlating to (-111) and (040) planes of ZrO_2.

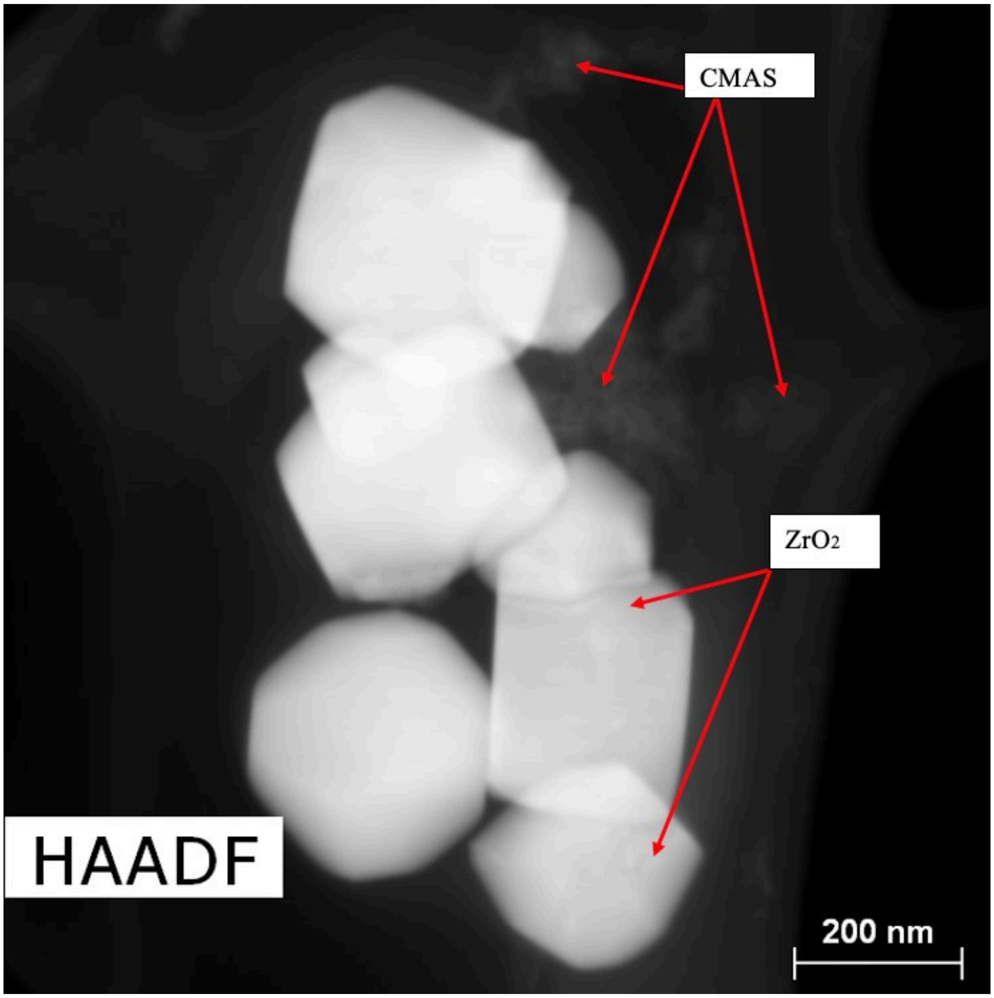

Figure 85. TEM image of ZrB_2+CMAS after 1600°C 100 hours exposure.

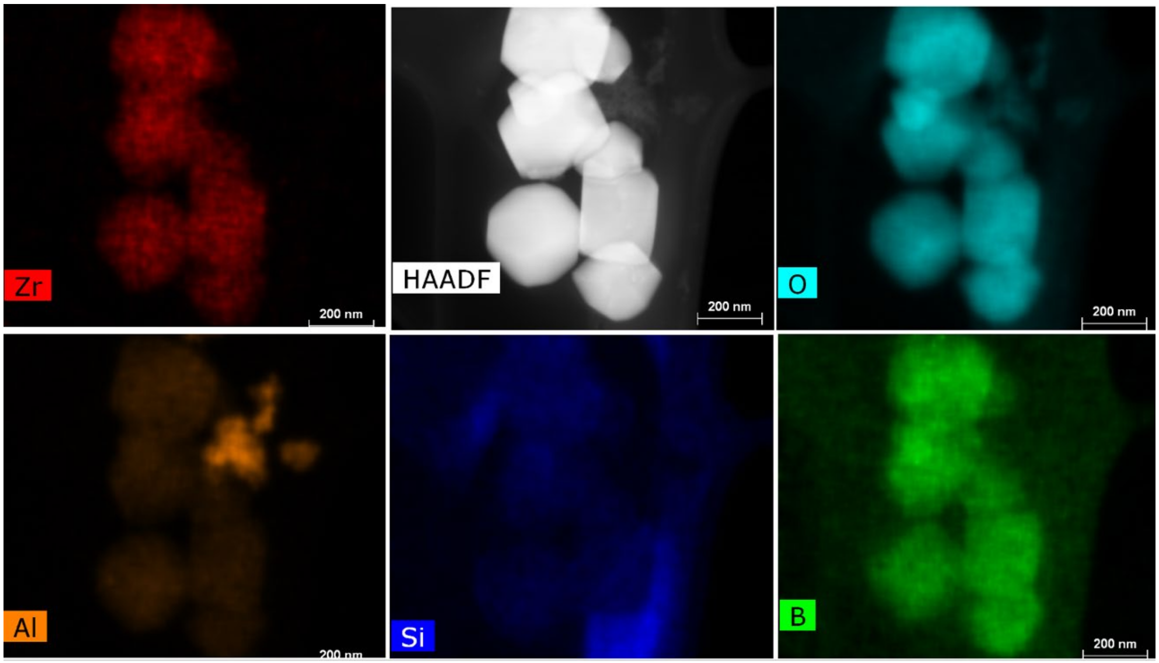

Figure 86. EDS mapping of ZrO_2 surrounded by a glassy and crystalline mixture of CMAS and boron(low confidence).

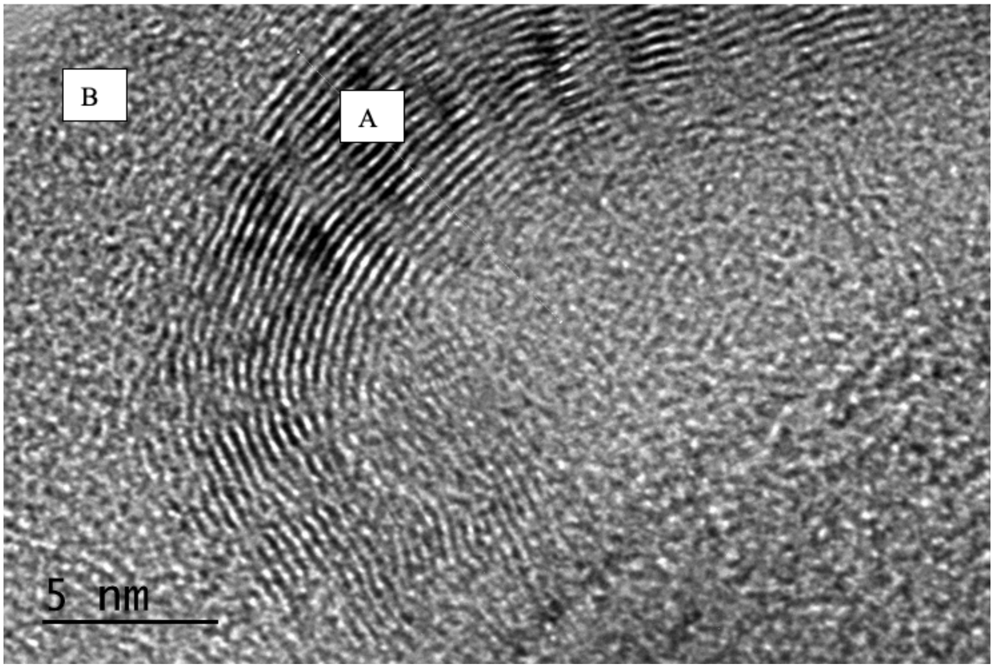

Figure 87. (A)Crystalline phase, ZrO_2, surround by (B)amorphous material (glassy CMAS).

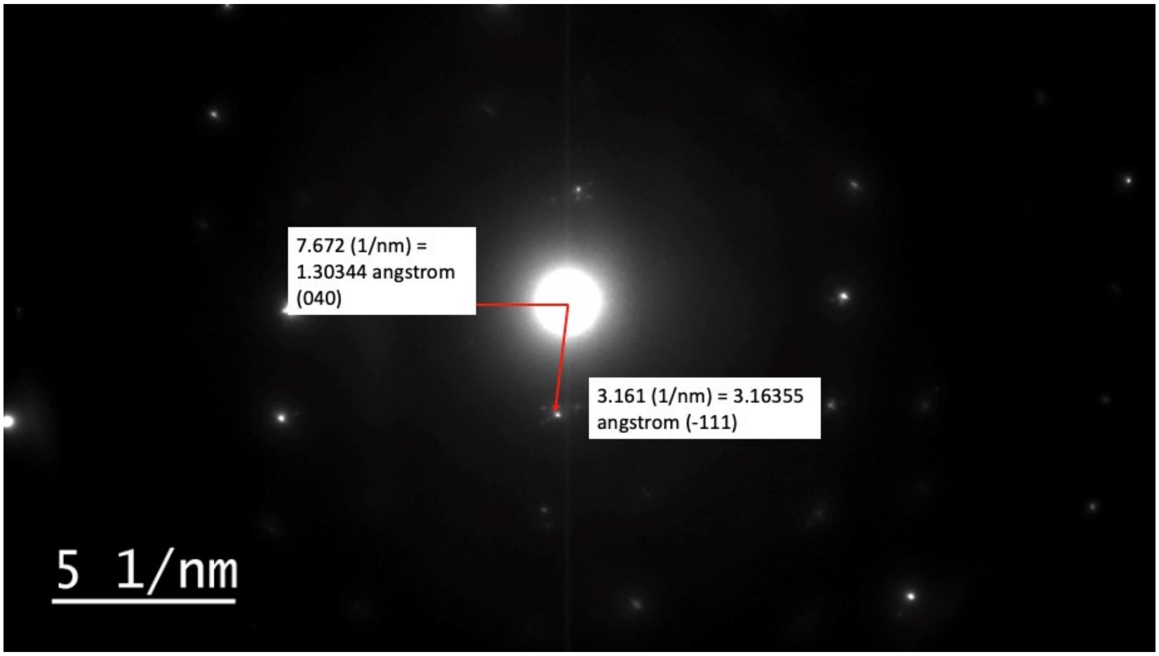

Figure 88. Electron diffraction of ZrO_2.

4. Comparison Across Temperature

All three runs, ZrB_2 reacted with the oxygen in the air to produce monoclinic phase of ZrO_2. As temperature and duration increase, the oxidation also increases yielding stronger peaks of ZrO_2 and essentially no ZrB_2 remaining after 100 hours at all temperatures as shows in XRD analysis in Figure 89, Figure 90, Figure 91, and Figure 92. Like with Hf runs, CMAS reacted with ZrO_2 and produced tetragonal phase of $ZrSiO_4$. The strongest intensity of $ZrSiO_4$ came from both 1000°C and1300°C exposed for 100 hours and is seen in Figure 92(B). Two deviations were observed when compared to HfB_2:

1. During one hour 1300°C trial, traces of $ZrSiO_4$ were observed via XRD, shown in Figure 89, where in all hafnium one hours runs, No $HfSiO_4$ were observed.
2. In all 1600°C runs, $ZrSiO_4$ did not form and confirmed findings by Curtis when $ZrSiO_4$ started to disassociate back to ZrO_2 and SiO_2 at around

1530°C[33]. For Hafnium, $HfSiO_4$ was observed at 1600°C with decreasing intensity as duration increase.

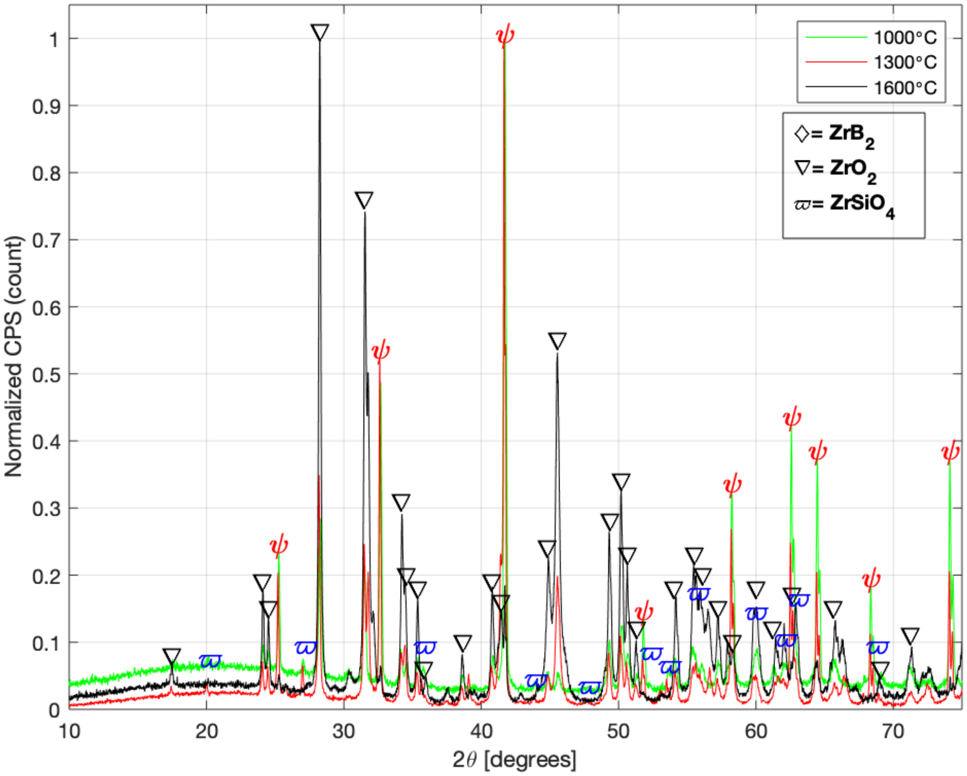

Figure 89. XRD spectra of ZrB_2+ CMAS at one hour exposure at 1000°C, 1300°C , and 1600°C. At one hour, no $ZrSiO_4$ developed with the exception at 1300°C. ZrB_2 nearly oxidized into ZrO_2 at 1600°C.

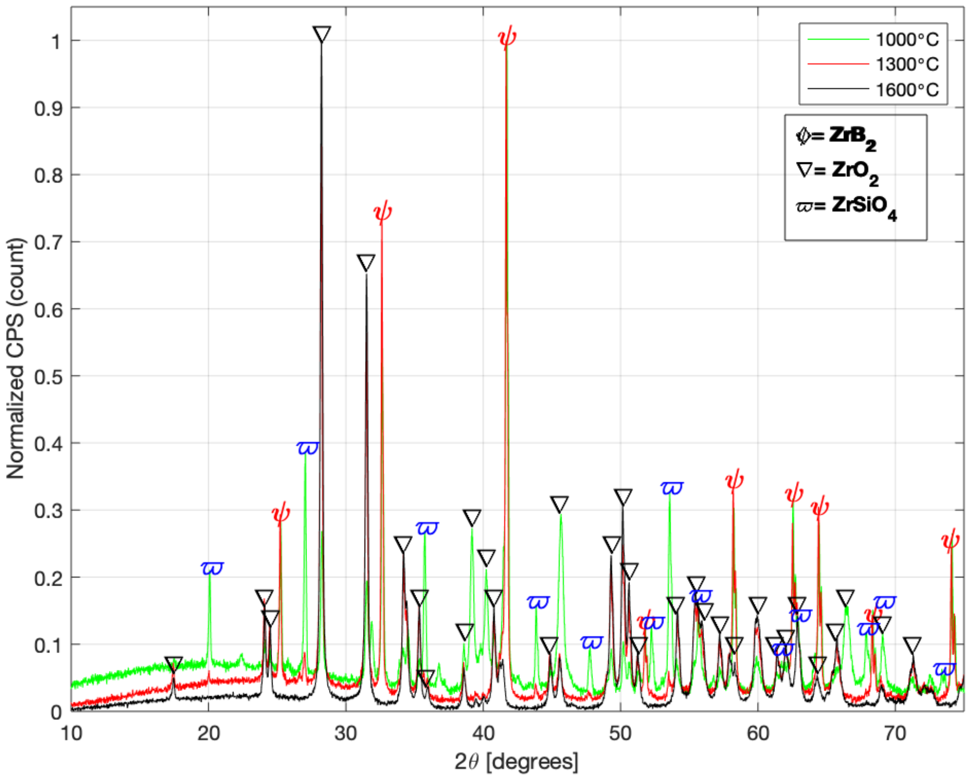

Figure 90. XRD spectra of ZrB_2+ CMAS at ten-hour exposure at 1000°C, 1300°C , and 1600°C. CMAS started to rapidly react with ZrO_2 and formed $ZrSiO_4$ as duration increased. ZrB_2 continues to oxidize into ZrO_2 as temperature increase with no detectable amount at 1600°C.

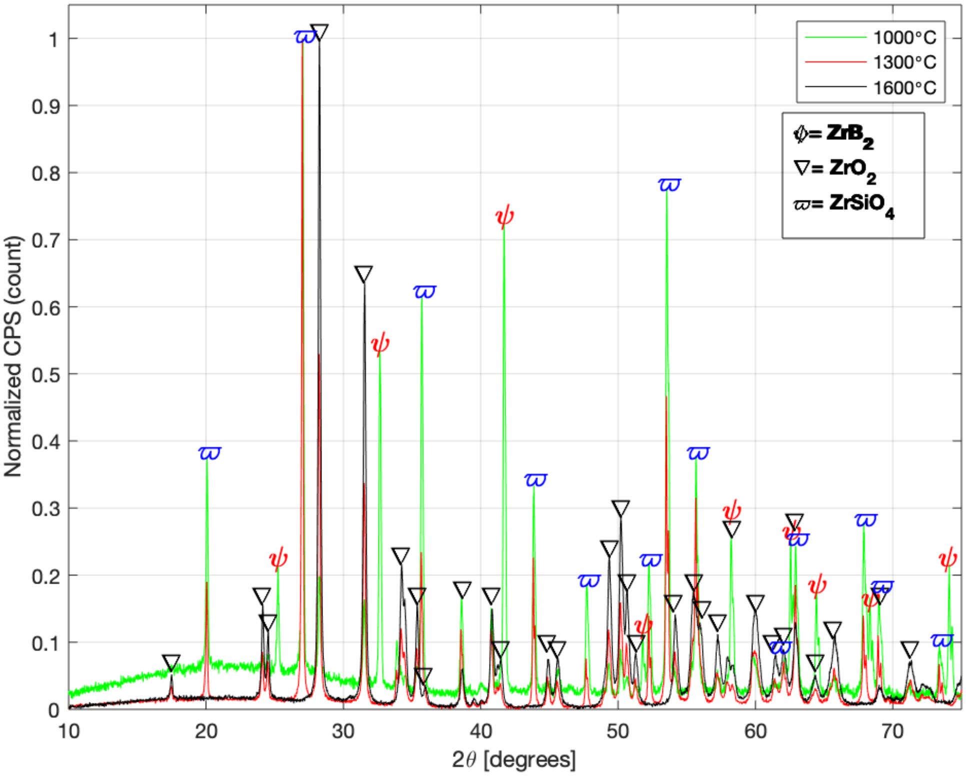

Figure 91. XRD spectra of ZrB_2+ CMAS at 100 hour exposure at 1000°C, 1300°C , and 1600°C. $ZrSiO_4$ yielded 1000°C and 1300°C. ZrB_2 completely oxidized into ZrO_2 at 1300°C and 1600°C.

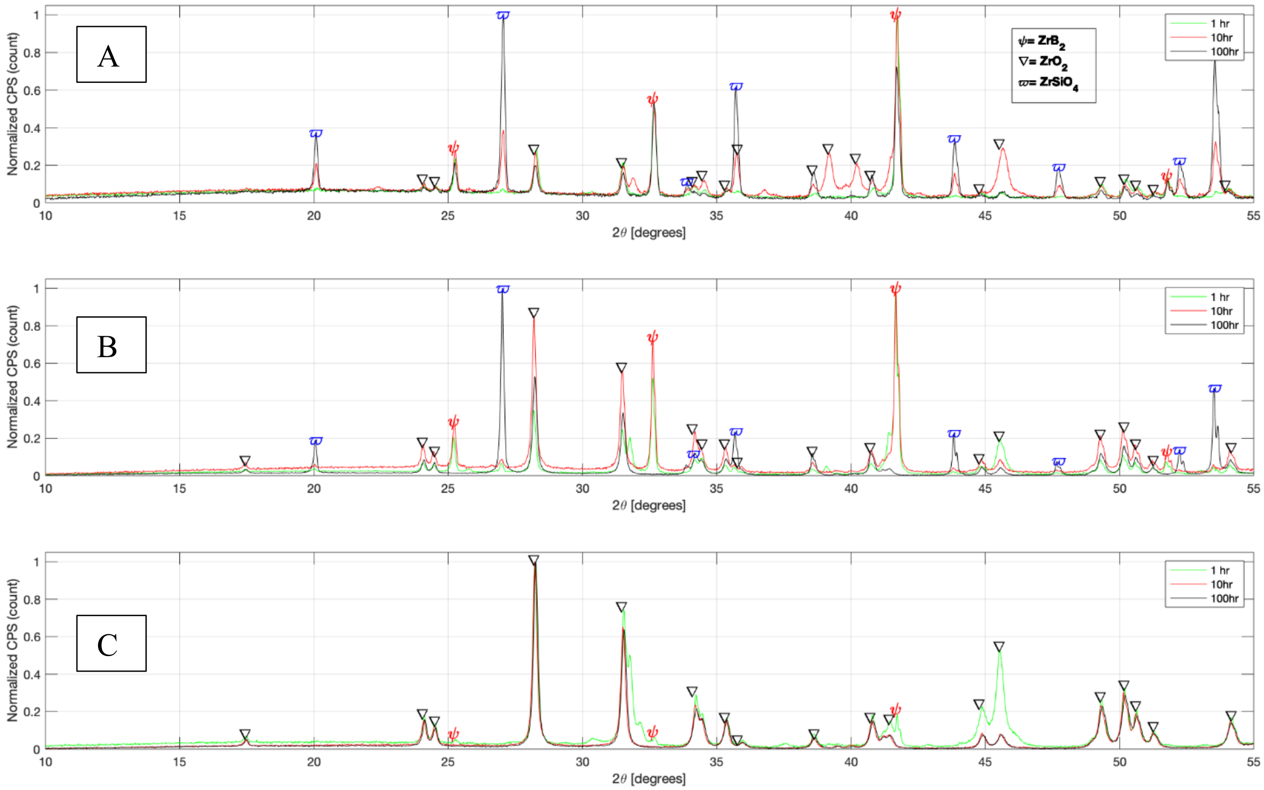

Figure 92. All plots show ZrB_2 oxidizes into ZrO_2, and ZrO_2 reacts with CMAS to yield $ZrSiO_4$. (A) 1000°C isothermal at 1,10,100 hours. (B) 1300°C isothermal at 1,10,100 hours. (C) 1600°C isothermal at 1,10, 100 hours.

F. REACTIVITY TRENDS AND COMPARISON WITH PREVIOUS STUDIES

The experiments conveyed both ZrB_2/HfB_2+CMAS interaction is dependent on the oxidation product and time exposure.

For hafnium, in all the one hour runs, regardless of temperature, HfO_2 did not react with CMAS. In all runs, HfB_2 oxidizes into monoclinic phase HfO_2 and, at longer and higher temperatures, produced gaseous B_2O_3 are evident by the porous material left over. As exposure time increases, HfO_2 begins to interact SiO_2 [31]found within CMAS yielding tetragonal $HfSiO_4$ with reaction strongest at 1300°C exposed for 100 hours. $HfSiO_4$ likely disassociated back into HfO_2 as evident in the XRD plots and as suggested by Salt et al.[31].Table 13 summarizes the reaction products from the experiment runs.

Table 13. HfB_2+CMAS products from the trials.

	1 hour	10 hours	100 hours
1000°C	**HfB_2**, HfO_2	**HfB_2**, HfO_2, *$HfSiO_4$*	**HfB_2**, HfO_2, *$HfSiO_4$*
1300°C	**HfB_2**, HfO_2 B_2O_3	**HfB_2**, HfO_2, *$HfSiO_4$*, B_2O_3	**HfB_2**, HfO_2, *$HfSiO_4$*, B_2O_3
1600°C	**HfB_2**, HfO_2,	**HfB_2**, HfO_2, *$HfSiO_4$*,	**HfB_2**, HfO_2, *$HfSiO_4$*,

For zirconium, the runs closely followed the same trends exhibited by hafnium, but the reactions were more volatile. ZrB_2 also oxidized much faster than HfB_2, reaffirming Gasch et al.[1] findings. With increasing ZrO_2, CMAS react with it to form $ZrSiO_4$, to include at 1300°C one hour exposure run but did not formed at 1600°C. At 1600°C, very little ZrB_2 was observed at one hour and at longer exposures, it is completely gone leaving just ZrO_2. Summary of products are shown in Table 14.

Both ZrB_2 and HfB_2 runs, no B_2O_3 were detected via XRD but observed in EDX. The glassy reside observed on the surface the materials and in the crucible were analyzed and were silicious in nature with traces of Hf/ZrO_2 detected. $HfSIO_4$ relative XRD intensities were significantly weaker at 1600°C and nonexistent in for ZrB_2. To ensure CMAS did not volatized at higher temperatures and longer exposures. Opie showed CMAS experienced significant mass loss with increasing temperature [7]. Ahlborg and Zhu also experienced CMAS volatility for exposures over 50 hours and added more CMAS to their samples to better stimulate environmental conditions[33]. 5 grams of CMAS was heated at 1600°C for ten hours inside a platinum crucible and measured again at 4.90 grams (2%

decrease). Another trial used 5 grams of AFRL-02 CMAS former using same temperature ramp up and hold and yielded 3.28 grams, a 34% loss. The result shows CMAS did not volatized during the higher temperature runs.

Table 14. ZrB_2+CMAS products from the trials.

	1 hour	10 hours	100 hours
1000°C	**ZrB_2**, ZrO_2	**ZrB_2**, ZrO_2, $ZrSiO_4$	**ZrB_2**, ZrO_2, $ZrSiO_4$
1300°C	**ZrB_2**, ZrO_2, *$ZrSiO_4$*, B_2O_3	**ZrB_2**, ZrO_2, *$ZrSiO_4$*, B_2O_3	**ZrB_2**, ZrO_2, *$ZrSiO_4$*, B_2O_3
1600°C	**ZrB_2**, ZrO_2,	ZrO_2	ZrO_2

Studies were conducted on 20% SiC doped Zr/HfB_2 [34,35] similar conditions and yield the same results seen in CMAS exposed attack. The silicon in SiC reacted with both Hf/ZrO_2 to produced Hf/$ZrSiO_4$. For the hafnium study, Parthasarathy et al. noted in higher temperatures(1900 to 2000°C under 8 minutes) $HfSiO_4$ formed on the leading edge of a hypersonic body and attributed to high fluid flow conditions from the scramjet used [34]. The experiment consisted using a SiC-HfB_2 leading edge connected to a scramjet rig used to simulate supersonic flight (and hypersonic) and tested under different Mach numbers ranging from 4–23 minutes of exposure [34]. The results from the experiments shared many similarities seen in this thesis and are shown in Figure 93.

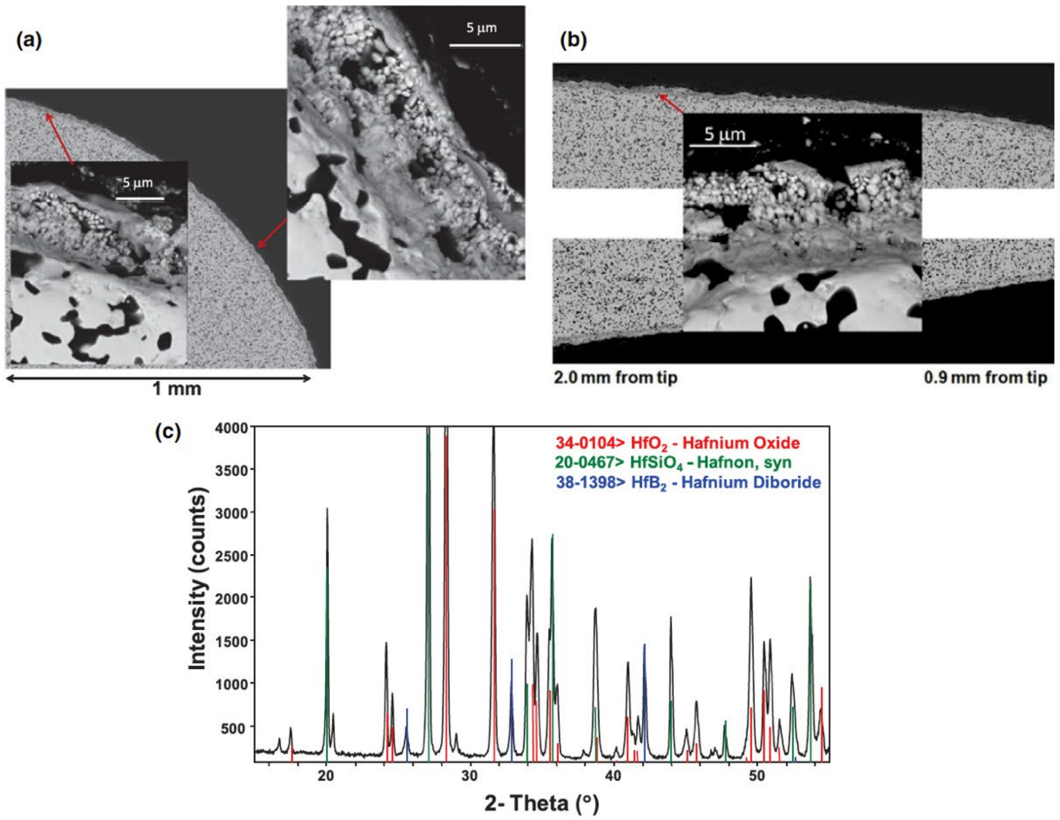

Figure 93. (A) The oxidations at the tip of the leading edge is shown. HfO_2 share the same shape as seen in Figure 36 and Figure 46. (B) Another view of the leading edge containing HfO_2. (C) XRD spectra of the sample showing peaks correlating to all three Hf samples. The formation of $HfSiO_4$ in the SiC doped HfB_2 proves that the silicon in the CMAS reacted with HfO2 to formed to hafnon. The XRD plot also shares the same peaks found in Figure 57. Source: [34].

Gao et al.[35] also conducted high temperature testing of 20% SiC doped ZrB_2 at 1000°C, 1200°C, 1400°C, and 1600°C each at 30 minutes using a tube furnace with a nitrogen rich atmosphere. When the target temperature was reached, oxygen was introduced with a partial pressure of 200 Pa [35]. Gao et al. found $ZrSiO_4$ to form between 1200–1400°C with relative intensity strongest at 1400°C and attributed $ZrSiO_4$ formation rate to both oxidation temperature and oxygen partial pressure [35]. Gao et al. also noted no $ZrSiO_4$ formed at 1600°C with densely packed ZrO_2 particles and attributed the missing $ZrSiO_4$ to its chemical instability [35]. The XRD spectra from the experiment are shown in Figure 94 and match the XRD spectra seen in Figure 92. The particles, Figure 95, match the shape and size seen in Figure 83 and Figure 84.

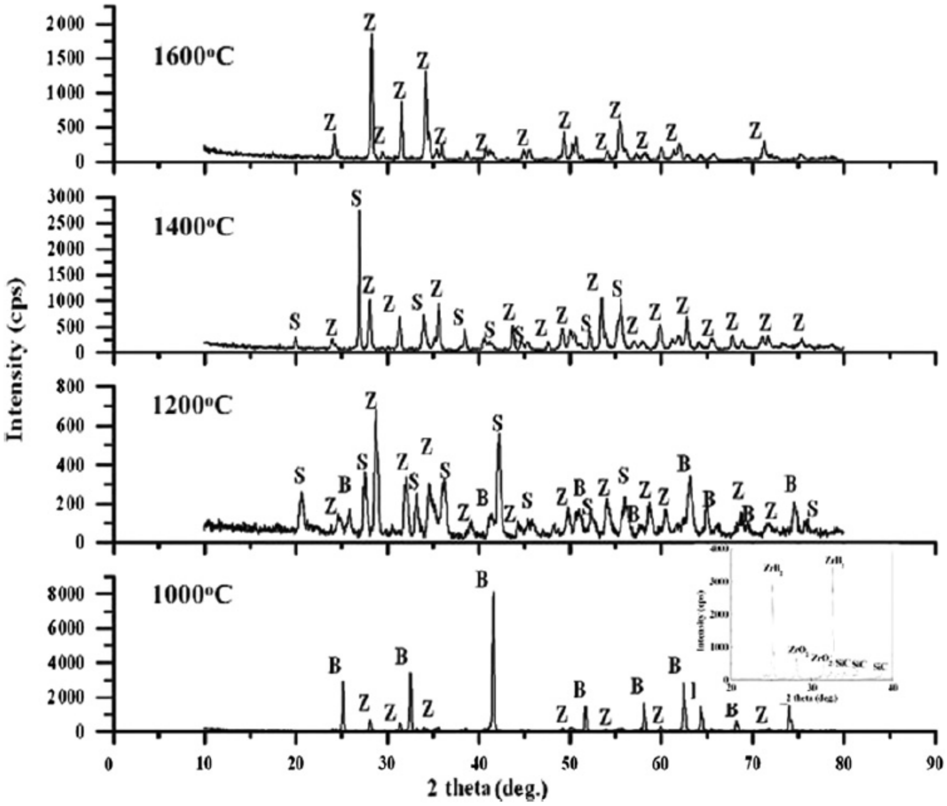

Figure 94. XRD spectra from SiC doped ZrB_2 after heating at various temperatures. B, Z, S correlate to ZrB_2, ZrO_2, and $ZrSiO_4$ respectively. The plots are match the results seen in Figure 92 and support that silicon found in CMAS reacts with ZrO_2 to form $ZrSiO_4$ but reverts back to its original products once increasing to 1600°C. Source: [35].

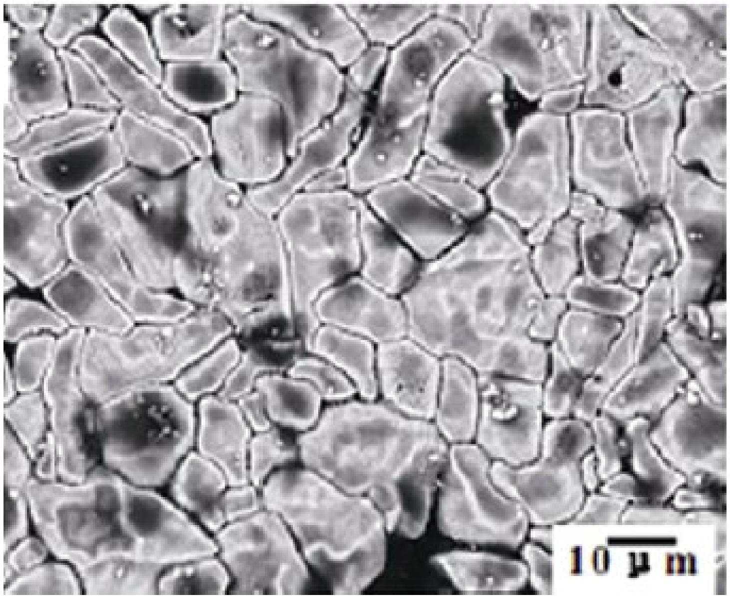

Figure 95. ZrO_2 after heated to 1600°C. Gao found no $ZrSiO_4$ in the sample as well. Source: [35].

THIS PAGE INTENTIONALLY LEFT BLANK

V. CONCLUSION

A. SUMMARY

Overall, the runs show ZrB_2 and HfB_2 does not explicitly reacted with CMAS. Their respective oxidation products ZrO_2 and HfO_2 do react with CMAS.

- Both oxidation products react with the silicon found in CMAS to yield Zr/ $HfSiO_4$.
- Both dissolute back into SiO_2 and Zr/HfO_2 at higher temperatures and exposure rates due to its chemical instability [33–35].
- HfB_2 displayed increased volatility to CMAS at increased temperatures compared to ZrB_2 as $HfSiO_4$ was detected at 1600°C.
- CMAS has the greatest effects on the UHTCs at 1300°C where the relative XRD peaks of Zr/$HfSiO_4$ were the strongest.

B. IMPLICATIONS FOR HYPERSONIC AND OTHER HIGH TEMPERATURE APPLICATIONS

Formations of both Hf/$ZrSiO_4$ is the strongest at 1300°C before breaking back down to its respective oxide and a glassy silica equilibrium mix. The data suggest that at higher temperatures, CMAS attack will not have a great effect on these ceramics as they transit at lower altitudes in a sand-dense atmosphere such as those found in the Middle East.

Both ceramics have promising properties that are favorable for the next generation of advanced E/TBC for gas turbine engines as higher temperatures are achieved. The limited reaction with CMAS at higher temperatures suggest an increase in the engine life and reducing maintenance cost of engines as they operate in sandy environments throughout the world.

C. DIRECTION FOR FUTURE WORK

Controlling oxidations rates will be key to preventing CMAS attack on the ceramics. Further studies are needed to better characterization of these reactions such as using bulk pucks of ZrB_2 and HfB_2. Using both ceramics with other E/TBC substrates to explore and characterize CMAS attack. Lastly using more realistic conditions such as a wind tunnel/rig burner to stimulate high velocity flow can provide further insight to CMAS attack.

LIST OF REFERENCES

[1] Gasch, M. J., Ellerby, D. T., and Johnson, S. M., 2005, “Ultra High Temperature Ceramic Composites,” Handbook of Ceramic Composites. N.P. Bansal, ed., Springer U.S., Boston, MA, pp. 197–224.

[2] Eakins, E., Jayaseelan, D. D., and Lee, W. E., 2011, “Toward Oxidation-Resistant ZrB2-SiC Ultra High Temperature Ceramics,” Metallurgical and Materials Transactions A, 42(4), pp. 878–887.

[3] Parthasarathy, T. A., Rapp, R. A., Opeka, M., and Kerans, R. J., 2007, “A Model for the Oxidation of ZrB2, HfB2 and TiB2,” Acta Materialia, 55(17), pp. 5999–6010.

[4] Berkowitz-Mattuck, J. B., 1966, “High-Temperature Oxidation: III . Zirconium and Hafnium Diborides,” Journal of the Electrochemical Society, 113(9), p. 908.

[5] Guo, W.M., Zhang, G.J., Kan, Y.M., and Wang, P.L., 2009, “Oxidation of ZrB2 Powder in the Temperature Range of 650–800°C,” Journal of Alloys and Compounds, 471(1), pp. 502–506.

[6] Nieto, A., Agrawal, R., Bravo, L., Hofmeister-Mock, C., Pepi, M., and Ghoshal, A., 2020, “Calcia–Magnesia–Alumina–Silicate (CMAS) Attack Mechanisms and Roadmap Towards Sandphobic Thermal and Environmental Barrier Coatings,” International Materials Reviews, pp. 1–42.

[7] Opie, N., 2014, “A Comparison of Afghanistan, Yuma, AZ, and Manufactured Sands Melted on EB-PVD Thermal Barrier Coatings,” Thesis, Air Force Institute of Technology.

[8] Kelley, J. R., Wakeley, L. D., McKenna, J. R., and Jackson, S. S., 2010, “Physical Characteristics of Soil Collected in Iraq and Afghanistan Related to Remote Sensing,” Engineer Research And Development Center Vicksburg Ms Geotechnical And Structures Lab.

[9] Ditzler, C., Scheffe, K., and Monger, H. C., 2017, “Soil Survey Manual,” Government Printing Office, Washington, D.C.

[10] Engelbrecht, J., McDonald, E., Gillies, J., and Gertler, A., 2008, “Department of Defense Enhanced Particulate Matter Surveillance Program (EPMSP),” Desert Research Institute, Reno, NV.

[11] Smialek, J. L., Archer, F. A., and Garlick, R. G., 1994, “Turbine Airfoil Degradation in the Persian Gulf War,” JOM, 46(12), pp. 39–41.

[12] de Wet, D. J., Taylor, R., and Stott, F. H., 1993, “Corrosion Mechanisms Of ZrO2-Y2O3 Thermal Barrier Coatings In The Presence Of Molten Middle-East Sand Le Journal de Physique IV, 03(C9), pp. C9-655-C9-663.

[13] Bose, S., 2018, High Temperature Coatings, Butterworth-Heinemann, Cambridge, MA.

[14] Smialek, J. L., and Miller, R. A., 2018, “Revisiting the Birth of 7YSZ Thermal Barrier Coatings,” Coatings, 8(7), p. 255.

[15] Padture, N. P., 2002, “Thermal Barrier Coatings for Gas-Turbine Engine Applications,” Science, 296(5566), pp. 280–284.

[16] Ghoshal, A., Murugan, M., Walock, M. J., Nieto, A., Barnett, B. D., Pepi, M. S., Swab, J. J., Zhu, D., Kerner, K. A., Rowe, C. R., Shiao, C.Y., Hopkins, D. A., and Gazonas, G. A., 2017, “Molten Particulate Impact on Tailored Thermal Barrier Coatings for Gas Turbine Engine,” Journal of Engineering for Gas Turbines and Power, 140(022601).

[17] Krämer, S., Yang, J., Levi, C. G., and Johnson, C. A., 2006, “Thermochemical Interaction of Thermal Barrier Coatings with Molten CaO–MgO–Al2O3–SiO2 (CMAS) Deposits,” Journal of the American Ceramic Society, 89(10), pp. 3167–3175.

[18] Wu, J., Guo, H., Gao, Y., and Gong, S., 2011, “Microstructure and Thermo-Physical Properties of Yttria Stabilized Zirconia Coatings with CMAS Deposits,” Journal of the European Ceramic Society, 31(10), pp. 1881–1888.

[19] Wellman, R., Whitman, G., and Nicholls, J. R., 2010, “CMAS Corrosion of EB PVD TBCs: Identifying the Minimum Level to Initiate Damage,” International Journal of Refractory Metals and Hard Materials, 28(1), pp. 124–132.

[20] Shifler, D. A., and Choi, S. R., 2018, “CMAS Effects on Ship Gas-Turbine Components/Materials,” American Society of Mechanical Engineers Digital Collection.

[21] Wiesner, V. L., and Bansal, N. P., 2015, “Mechanical and Thermal Properties of Calcium–Magnesium Aluminosilicate (CMAS) Glass,” Journal of the European Ceramic Society, 35(10), pp. 2907–2914.

[22] “AFRL 02 Test Dust,” Powder Technology Inc. [Online]. Available: https://www.powdertechnologyinc.com/product/afrl-02-test-dust/. [Accessed: 23-Mar-2021].

[23] Wuchina, E., Opila, E., Opeka, M., Fahrenholtz, B., and Talmy, I., 2007, “UHTCs: Ultra-High Temperature Ceramic Materials for Extreme Environment Applications,” The Electrochemical Society Interface, 16(4), p. 30-36.

[24] Upadhya, K., Yang, J. M., and Hoffman, W., 1997, “Advanced Materials for Ultrahigh Temperature Structural Applications Above 2000 Deg C,” Air Force Research Lab Edwards AFB CA Propulsion Directorate West.

[25] Ma, H.B., Zou, J., Zhu, J.T., Lu, P., Xu, F.F., and Zhang, G.J., 2017, “Thermal and Electrical Transport in ZrB2 -SiC-WC Ceramics Up to 1800°C,” Acta Materialia, 129, pp. 159–169.

[26] Mallik, M., Kailath, Ansu. J., Ray, K. K., and Mitra, R., 2017, “Effect of SiC Content on Electrical, Thermal and Ablative Properties of Pressureless Sintered ZrB2-Based Ultrahigh Temperature Ceramic Composites,” Journal of the European Ceramic Society, 37(2), pp. 559–572.

[27] Zou, J., Sun, S.-K., Zhang, G.-J., Kan, Y.-M., Wang, P.-L., and Ohji, T., 2011, “Chemical Reactions, Anisotropic Grain Growth and Sintering Mechanisms of Self-Reinforced ZrB2-SiC Doped with WC: Mechanisms of Self-Reinforced ZrB2-SiC Doped with WC,” Journal of the American Ceramic Society, 94(5), pp. 1575–1583.

[28] Tandon, R., Dumm, H. P., Corral, E., Loehman, R., and Kotula, P., 2006, Ultra High Temperature Ceramics for Hypersonic Vehicle Applications, SAND Report No. SAND 2006–2925.

[29] Bargeron, B., Benson, R., Newman, R., Jette, A. N., and Phillips, T. E., 1993, “Oxidation Mechanisms Of Hafnium Carbide And Hafnium Diboride In The Temperature Range 1400 To 2100°C,” Materials Research And Applications—II, 14(1), pp. 29–36.

[30] Wiesner, V. L., Scales, D., Johnson, N. S., Harder, B. J., Garg, A., and Bansal, N. P., 2020, “Calcium–Magnesium Aluminosilicate (CMAS) Interactions with Ytterbium Silicate Environmental Barrier Coating Material at Elevated Temperatures,” Ceramics International, 46(10), pp. 16733–16742.

[31] Salt, D. J., and Hornung, G., 1967, “Synthesis and X-Ray Study of Hafnium Silicate,” Journal of the American Ceramic Society, 50(10), pp. 549–550.

[32] Curtis, C. E., and Sowman, H. G., 1953, “Investigation of the Thermal Dissociation, Reassociation, and Synthesis of Zircon,” Journal of the American Ceramic Society, 36(6), pp. 190–198.

[33] Ahlborg, N. L., and Zhu, D., 2013, “Calcium–Magnesium Aluminosilicate (CMAS) Reactions and Degradation Mechanisms of Advanced Environmental Barrier Coatings,” Surface and Coatings Technology, 237, pp. 79–87.

[34] Parthasarathy, T., Petry, M., Cinibulk, M., Mathur, T., and Gruber, M., 2013, "Thermal and Oxidation Response of UHTC Leading Edge Samples Exposed to Simulated Hypersonic Flight Conditions," Journal of the American Ceramic Society, pp. 907–915.

[35] Gao, D., Zhang, Y., Fu, J., Xu, C., Song, Y., and Shi, X., 2010, "Oxidation of Zirconium Diboride–Silicon Carbide Ceramics Under An Oxygen Partial Pressure of 200 Pa: Formation of Zircon," Corrosion Science, 52(10), pp. 3297–3303.

INITIAL DISTRIBUTION LIST

1. Defense Technical Information Center
   Ft. Belvoir, Virginia

2. Dudley Knox Library
   Naval Postgraduate School
   Monterey, California